Geo-information Science and Remote Sensing

Thesis Report GIRS-2024-28

Impact of Structure from Motion processing parameters on thermal orthomosaic temperatures

Jesper Linderhof

09-04-2024

Impact of Structure from Motion processing parameters on thermal orthomosaic temperatures

Jesper Linderhof

Registration number 1304925

Supervisors:

Magdalena Smigaj

A thesis submitted in partial fulfilment of the degree of Master of Science
at Wageningen University and Research,
The Netherlands.

09-04-2024
Wageningen, The Netherlands

Thesis code number: GRS-80436
Thesis Report: GIRS-2024-28
Wageningen University and Research
Laboratory of Geo-Information Science and Remote Sensing

Acknowledgements

I would like to thank everyone that was directly or indirectly involved in or contributed to this thesis. First of all, I would like to thank Magdalena Smigaj for supervising this thesis and providing me with feedback on my progress throughout this project. At times when I was struggling, her support helped me to further the research into the right direction.

Furthermore, I would like to thank Sytze de Bruin and George van Voorn for their insights on how to assess the influence of the SfM parameters on orthomosaic temperatures. I would also like to thank Quanxing Wan for his support during fieldwork.

Lastly, I would like to thank my fellow students for their feedback during thesis rings, and the general discussions we had in the thesis room.

Table of contents

Abstract

The miniaturization of thermal cameras made it possible to mount them to small-sized unmanned aerial vehicle (UAV) platforms, with benefits including high spatial and temporal resolution. UAV thermal images are typically processed with the structure from motion (SfM) workflow, to generate a thermal orthomosaic. However, little is known about the influence of SfM parameters on resultant orthomosaic temperatures. In this study, the influence of five SfM parameters on orthomosaic temperatures was explored in Agisoft Metashape. The tested parameters included the co-alignment (or the lack of) of thermal images with multispectral images, the dense point cloud (DPC) quality settings, the DPC depth filtering settings, the use of colour calibration, and the choice of a blending mode. The influence of the parameters was assessed through a one-at-a-time sensitivity analysis. Although the temperature influence of the co-alignment could not be assessed, as the thermal imagery failed to properly align without the aid of multispectral imagery, other parameters showed distinctive patterns. The parameter with the highest influence was colour calibration.

The extent of the influence of colour calibration on orthomosaic temperatures was determined by temperature differences in the data, and the used blending mode. The choice of blending mode had large influence on orthomosaic temperatures in areas with high temperature fluctuations between adjacent images. The DPC quality and depth filtering settings had the least influence on orthomosaic temperatures. However, substantial variability was observed if the DPC parameters were combined with the mosaic blending mode. In general, the selection of parameters should be made on a case-by-case basis. For applications where a high accuracy is required, it is advised not to use thermal orthomosaic without validation with ground reference measurements.

List of abbreviations

DEM - Digital elevation model
DPC - Dense point cloud
FOV - Field of view
GSA - Global sensitivity analysis
IQR - Interquartile range
MAE - Mean absolute error
NUC - Non-uniformity correction
RMSE - Root mean squared error
SfM - Structure from motion
UAV - Unmanned aerial vehicle
-

1 Introduction

1.1 Context

Rainfall patterns are becoming more variable due to climate change, increasing the frequency of droughts (Rama et al., 2022). This can result in water deficiencies in plants since they cannot gather enough water to meet their evaporation demands. In response to drought stress, plants close their stomates to prevent further water loss (Ludovisi et al., 2017; Ozturk et al., 2021). Prolonged drought will cause plants to reduce growth, start wilting and take on a yellow colour. Accordingly, the (ecosystem) services plants can provide diminish (Yang et al., 2021). Detecting drought early would allow nature conservationists, farmers, and urban green managers to mitigate aforementioned effects.

The early stages of drought stress often cannot be visually determined. However, thermal infrared cameras can detect changes in canopy temperatures caused by stress (Galieni et al., 2021; Virtue et al., 2021). The magnitude of these changes differs based on the type of stress and plant. In proximal studies, drought stress resulted in a temperature increase of 0.7 °C to 6 °C (Belfiore et al., 2019; García-Tejero et al., 2012; Mulero et al., 2023; Pineda et al., 2020; Sepulcre-Cantó et al., 2006) whereas viral infections resulted in temperature increases between 0.5 °C and 1.5 °C (Hasan et al., 2023; Pineda et al., 2020; L. Wang et al., 2019). Detecting these types of stress is especially valuable in agriculture as it allows farmers to act swiftly, resulting in sustained and efficient plant growth with reduced water, nutrient, and pesticide usage (Khanal et al., 2017; Maes & Steppe, 2019).

Field measurements of plant health status are time and labour intensive. In contrast, a large area can be measured within a smaller timeframe through remote sensing. In recent years, small sized unmanned aerial vehicle (UAV) platforms have been introduced, enabling the capture of imagery at a high spatial, spectral, and temporal resolution (Maes & Steppe, 2019; Malbéteau et al., 2021). Simultaneously, thermal cameras have evolved from large spaceborne or airborne cameras with low spatial and temporal resolution to small sized cameras with a high spatial resolution (Khanal et al., 2017). The size reduction allowed thermal cameras to be mounted to UAVs, effectively increasing the temporal resolution. Consequently, UAV-based thermal cameras have been widely used in research, for several purposes. Examples are determining differences in drought response between different plants (Ludovisi et al., 2017; Qin et al., 2022), detecting salinity stress (Stutsel et al., 2021), creating irrigation plans (Gutiérrez-Gordillo et al., 2020), and monitoring underground coal fire (G. Yuan et al., 2021).

Despite their versatile use, UAV-based thermal cameras have limitations. The high resolution and small field of view of UAV-mounted cameras result in a large quantity of images during an overflight. The structure from motion (SfM) workflow is often applied to align the images and to construct a single orthorectified image. The low level of detail in thermal images makes it difficult for SfM algorithms to accurately align thermal images, negatively affecting the accuracy of the final orthomosaic. This, in combination with camera-related error sources, can restrict the usefulness of thermal imagery for applications where small differences in temperature need to be measured accurately (Maes & Steppe, 2019; Malbéteau et al., 2021; Mesas-Carrascosa et al., 2018). Examples are detecting plant stress, disease detection, the estimation of the evapotranspiration rate, and plant phenotyping (Eide et al., 2021; Elfarkh et al., 2023)

1.2 Research need

UAV mounted thermal cameras are uncooled, due to size and weight constraints. Such uncooled cameras are sensitive to temperature fluctuations of the sensor, as microbolometers in the focal plane array (FPA) heat up differently based on several factors. The drone and camera themselves influence the camera temperature through internal camera electronics, heat from the gimbal motor and air dissipation by the propellors (W. Yuan & Hua, 2022). The thermal emission of objects that are being measured is partially dissipated by parts of the camera, which creates an uneven heat measurement across the FPA. This dissipation can result in the vignetting effect (Malbéteau et al., 2021). External factors, such as the ambient temperature, wind speed and direction, humidity, cloud cover, and shadows also influence the measurements. These factors affect measurements mid-flight and cause fluctuations in FPA temperature (Aragon et al., 2020; G. Yuan et al., 2021).

Thermal cameras perform non-uniformity corrections during the flight to adjust to fluctuations in the FPA temperature, yet measurement differences remain (Acorsi et al., 2020). The measured objects themselves influence thermal measurements as well. Object characteristics such as reflectivity, emissivity, and radiation background temperature need to be considered (G. Yuan et al., 2021). The caveat is that for measuring differences between stressed and non-stressed plants a sub-1 °C accuracy is normally required (Mesas-Carrascosa et al., 2018). Depending on the target, currently available thermal cameras have an accuracy of up to ± 5 °C (Virtue et al., 2021). Consequently, derivation of accurate temperatures from raw thermal imagery captured by an uncooled thermal camera requires calibration. The most prominently researched source of error in UAV-based thermal imagery is the sensitivity and instability of uncooled thermal cameras. In response, many authors have created methods and procedures to correct for these inaccuracies. To illustrate, Aragon et al. (2020) suggested a calibration procedure based on the ambient temperature, Virtue et al. (2021) equipped a thermal camera with a heated shutter as a more reliable source for in-flight non-uniformity correction, and Kelly et al. (2019) suggested a set of best practices to consider before, during, and after the flight.

Processing thermal imagery into orthomosaic introduces additional error. The structure from motion (SfM) workflow is generally applied to generate thermal orthomosaics. However, this workflow is geared towards RGB/multispectral imagery with high amounts of discernible details. The lack of detail in thermal imagery affects the capability of SfM algorithms to identify tie-points between images and to align images. Furthermore, the temperature value for one location can be dynamic across thermal images due to the aforementioned fluctuations in FPA temperature (Maes et al., 2017; Malbéteau et al., 2021). Apart from alignment issues, other parameters influence orthomosaic temperatures as well. One of the main identified parameters is the blending mode, used for orthomosaic generation. Both Malbéteau et al. (2021) and Acorsi et al. (2020) discuss that the blending modes each produce different result, as each mode blends overlapping pixel values in different ways. Still, the influence of SfM parameters on resultant orthomosaic temperatures is scarcely discussed, despite being a known source of potential error (Malbéteau et al., 2021). In fact, most authors do not discuss the SfM parameters used in projects, despite the unknown temperature influence the parameters could have (Acorsi et al., 2020; Kelly et al., 2019; Maes et al., 2017; McCarthy et al., 2021, 2022; Ribeiro-Gomes et al., 2017).

1.3 Aim and research questions

At the moment of writing this thesis, there was limited knowledge on the influence of structure from motion processing parameters on resultant temperatures in thermal orthomosaics. The aim of this thesis was to determine what SfM parameters are influential on orthomosaic temperatures, and to determine what influence the parameters have on the resultant temperatures. The following research questions were answered to satisfy this aim:

1) What are the key processing parameters that affect thermal orthomosaic generation?
2) How do key processing parameters influence the temperatures of thermal orthomosaics?
3) How do different combinations of key processing parameters influence thermal orthomosaic temperatures?

2 Data and methods

The methodology is split into two parts: data acquisition & processing and data analysis (Figure 1). The first part addresses the steps taken to prepare the data for the analysis. This includes the data collection method (2.1.1), selection of influential structure from motion (SfM) processing parameters and orthomosaic generation (2.1.3 & RQ1) with a vignetting mask (2.1.2), and the empirical line correction of the orthomosaics (2.1.4). After the data processing, the influence of the SfM processing parameters was assessed through multiple one-at-a-time sensitivity analyses (2.2.3). The influence of each separate parameter was assessed first (2.2.4 & RQ2). Afterwards, the influence of parameter pairs was assessed (2.2.5 & RQ3). The outcome of these analyses consists of violin plots which depict the distribution and impact of parameters on the orthomosaic temperatures and inter-parameter influences.

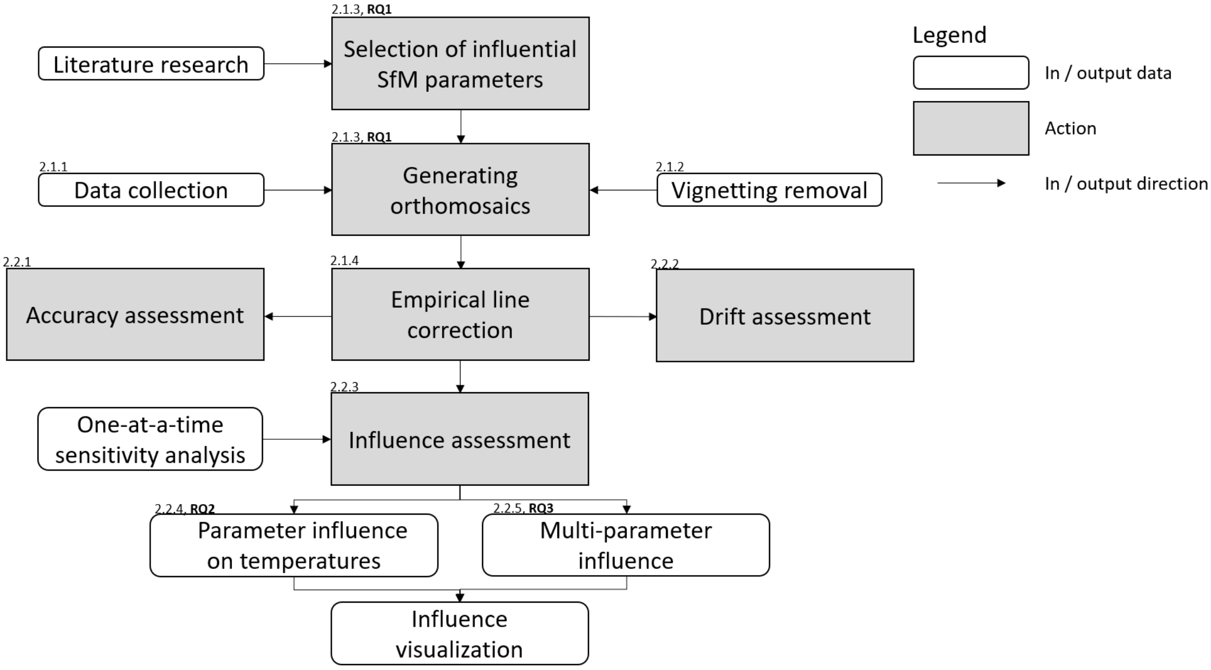

Figure 1 General methodological workflow, numbering in the boxes relates to headers in the methodology.

2.1 Data acquisition & processing

2.1.1 Data collection

The data for this project originates from the Nergena grass field in Bennekom, The Netherlands (Figure 2). It is in use for a drought resistance experiment among 20 grass species and mixtures, spread across 240 plots ranging in size from 1 x 1 m to 2 x 2 m (appendix B). Each plot is subject to one of four treatments. A plot is either irrigated or non-irrigated, with a grass height of 3 cm or 6 cm. The imagery of the grass field was acquired on the 7th of September 2023 at 1:00 pm in a 9 minute long flight, at a height of 30 meters. It was a sunny, cloudless day with an air temperature of 28 °C. The period before the data acquisition was one of frequent rainfall, with a total of 156 mm of rainfall in August 2023 measured by the Wageningen Pd weather station (KNMI, n.d.). Between 09:11 and 09:42 hours on the day of the data acquisition, the average measured volumetric water content was 12 % and 16 % for the non-irrigated and irrigated sides of the grass field, respectively.

For the analysis in this project, 36 of the 48 larger 2 x 2 meter plots were used (Figure 2). The larger plots were used as they provide a large sample size of pixels compared to the smaller 1 x 1 meter plots. If pixel values of adjacent plots are mistakenly included in a larger plot, their influence is smaller. 12

plots were omitted from the analysis due to temperature anomalies in the orthomosaics on the western side of the grass plot caused by the rapid change in FPA temperature.

The DJI M210 RTK UAV platform equipped with a Hiphen Airphen multispectral camera and a FLIR Tau 2 thermal camera was utilized to acquire the imagery. The Hiphen Airphen captures images at six wavelengths (450nm, 530nm, 570nm, 675nm, 730nm & 850nm), whereas the FLIR Tau 2 measures in the 7.5 nm to 13 nm range with an emissivity value of 0.98. The drone flew in a west-east direction (Figure 2). Five ground control points were placed around the grass field for post-alignment geometric correction in Metashape. The GPS location of these ground control points was measured with a Topcon RTK receiver.

Four reference panels and two water targets were placed to the south of the grass field, for post-flight temperature calibration. The reference panels' colour ranged from black to white, ensuring a range of temperature values. One of the water targets was kept cold by adding ice cubes, whilst the other was continuously warmed by the sun. The temperatures of these targets were measured with the Raytek Raynger ST handheld device (± 2 °C, emissivity value of 0.95), shortly after the drone passed. These measurements were converted to the target emissivity of 0.98, which corresponds to the emissivity of vegetation. After conversion, panel temperatures ranged from 26.6 °C to 40.6 °C, whereas the cold and warm water targets were 16.3 °C and 18.8 °C, respectively. After the drone passed, the ground reference temperatures of the 16 southmost 2 x 2 grass plots were measured (appendix C). The measured grass temperatures ranged from 20.7 °C to 24.3 °C.

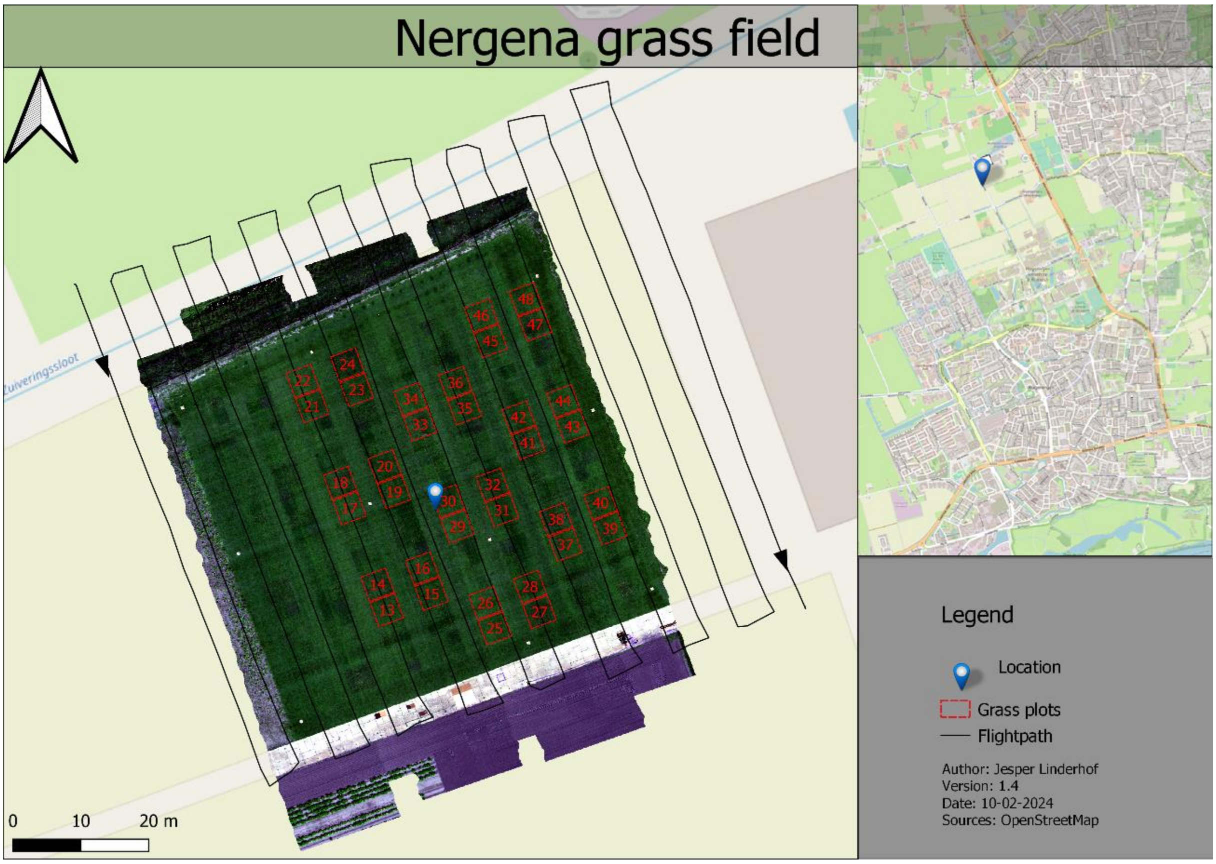

Figure 2 Nergena grass field, Bennekom, The Netherlands. Includes the 36 plots used in the assessment and the flight path of the drone that was used on the 7th of September.

2.1.2 Removing vignetting effect

Upon closer inspection of the captured thermal infrared imagery, vignetting was observed. Based on the recommendation by Kelly et al. (2019), only the central portion of the thermal imagery was used during the orthomosaicking process. The first 10 post-flight images of the uniform helipad surface were used to calculate residuals. It was assumed that post-flight images are most representative of in-flight images affected by flight conditions. The 10 residuals were averaged. Based on this average, different thresholds (of 1, 1.5 and 2 standard deviations) for outlier removal were trialled. The 1.5 standard deviation was seen as the most suitable as it retained most centre image values while removing most of the vignetting effect at the edges of the images (appendix D). A threshold of 1 or 2 standard deviations removed large portions of the central image values or nearly no values, respectively. Subsequently, a rectangular mask was made based on the 1.5 standard deviation threshold, which was applied to thermal images before the orthomosaic generation.

2.1.3 Generating orthomosaics

The thermal imagery was processed into orthomosaics with Agisoft Metashape 1.8.4. Five of the processing parameters in Metashape were identified as influential on thermal orthomosaic temperatures (Table 1). Two separate Metashape projects were created. In one project thermal imagery was aligned without aid by multispectral imagery, and one where thermal imagery was co-aligned with multispectral imagery. This ensured that the influence of the parameter's settings was kept separate. The workflow that was used consists of the alignment of imagery, geometric correction of the alignment based on ground control points, dense point cloud (DPC) generation, digital elevation model (DEM) generation, colour calibration and orthomosaicking.

Table 1 Tested parameters

Parameters	Setting or value(s) that have been tested
Co-alignment thermal imagery with multispectral imagery	Thermal imagery or thermal + Multispectral imagery
Dense point cloud quality setting	Ultra-high, high, medium, low, lowest
Dense point cloud depth filtering	Disabled, mild, moderate, aggressive
Colour calibration	No colour calibration, tie point-based colour calibration, DEM based colour calibration
Orthomosaicking blending mode	Mosaic, average, disabled

The parameter selection was based on the presumed influence of parameters on orthomosaic temperatures. The selected parameters are the co-alignment of thermal imagery with multispectral imagery, DPC quality, DPC depth filtering, colour calibration and the blending mode.

The co-alignment of thermal imagery is known to improve the geometric accuracy, gaps, and artefacts in thermal orthomosaics (Kapil et al., 2023; Maes et al., 2017). These inaccuracies may influence the allocation of temperatures in orthomosaics. The DPC quality and DPC depth filtering settings influence the heights in the DPC, and the DEM (Benjamin & Dennis O'brien, 2017; Conte et al., 2018; Ribeiro-Gomes et al., 2017; Tinkham & Swayze, 2021). Higher DPC quality settings lead to better dense point cloud geometry (Benjamin & Dennis O'brien, 2017; Conte et al., 2018; Ribeiro-Gomes et al., 2017). Each step down in quality reduces the resolution of the original imagery, whereas the ultra-high setting retains the original image resolution (Tinkham & Swayze, 2021). Depth filtering removes noise, thus influences the height differences in the DPCs (Conte et al., 2018; Ribeiro-Gomes et al., 2017). According to Tinkham & Swayze (2021), depth filtering removes outlier points from the DPC through a connected component filter with differing thresholds per depth filtering setting. The DEM is based on the DPC, thus the DPC quality and depth filtering settings could influence the orthomosaic temperatures.

Before orthomosaicking, colour calibration can be applied to the imagery. This calibration evens out the brightness across all images in the dataset, and thus directly affects temperature values (Agisoft, 2023). The blending mode determines how pixel values of overlapping images are mixed, and thus directly influences the orthomosaic temperatures. This influence was confirmed in prior research by Acorsi et al. (2020) and Malbéteau et al. (2021). The disabled blending mode does not mix pixel values, yet only retains the pixel values closest to nadir. The average blending mode performs a weighted average. In contrast, the mosaic blending mode divides the data into multiple domains and mixes pixel values most at the seamlines (Agisoft, 2023).

The parameters that were not selected are important in the orthomosaicking process. However, most of these settings do not influence the orthomosaic temperatures. For the alignment process, parameters such as the alignment quality, key point limit, and tie-point limit were set to fixed values (appendix E). The alignment quality was set to the highest quality to have the best chance of a proper alignment without co-aligning thermal imagery (Agisoft, 2023). The key-point limit and tie-point limit were set to the default values (Acorsi et al., 2020; Maes et al., 2017; Śledź & Ewertowski, 2022). The remaining parameters determine what data is used in processing steps, the projection, resolution, interpolation, and hole filling. All these settings were set to the default settings (appendix E).

2.1.4 Empirical line correction

The generated orthomosaics were radiometrically calibrated with the empirical line method. The ground reference measurements of the reference panels and water targets were used, as this shows great correlation (Graph 1). The R^2 across all orthomosaics ranged between 0.94 and 0.96. For each orthomosaic, the temperature at the centre portion of the panels with a diameter of 8 centimetres was extracted. This diameter was used to match the field of view (FOV) of the Raytek handheld device at a height of 1 meter above the ground. Given the emissivity value of 0.95 used by the handheld device, the handheld measurements were transformed to match the emissivity value of 0.98 used by the FLIR Tau 2. Based on these transformed values and the extracted temperatures, the orthomosaics were corrected.

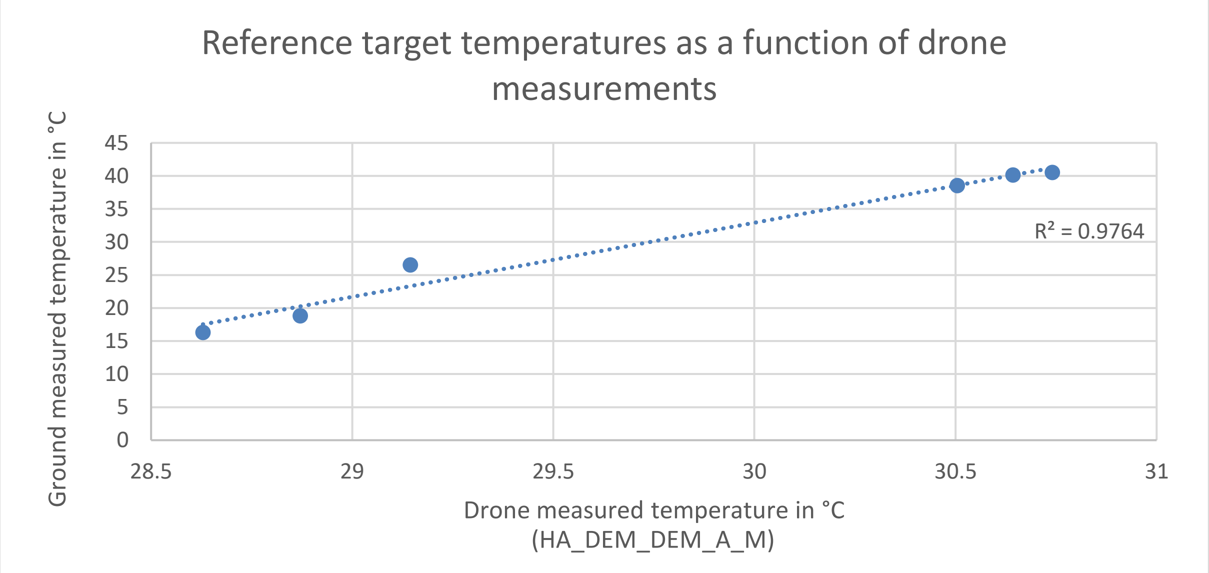

Graph 1 Example of ground reference measurements (y-axis) plotted against values extracted from an orthomosaic (x-axis). The orthomosaic used was generated using the high DPC quality setting, the aggressive DPC depth filtering setting, DEM based colour calibration and the average blending mode.

2.2 Data analysis

2.2.1 Accuracy assessment

After the empirical line correction was applied, the accuracy of the orthomosaic temperatures was assessed based on ground reference measurements of the 16 southmost grass plots. The ground reference measurements from the sixteen southmost 2 x 2 meter plots were first transformed to match a 0.98 emissivity value. In each orthomosaic, sixteen average temperature values were extracted from the middle of the sixteen grass plots (appendix C). The temperatures were extracted from a circular shape with a diameter of 8 centimetre, matching the FOV of the Raytek handheld device if used at a height of 1 meter. The values extracted from all orthomosaics were compared to the ground reference measurements to calculate the root mean squared error (RMSE), mean absolute error (MEA) and the R^2.

2.2.2 Drift assessment

Both before and after radiometric correction, an eastward temperature increase was observed in the orthomosaics. Given the west – east flight direction and a decrease in FPA temperature of 7 °C throughout the flight, it was suspected that the temperature increase was caused by thermal drift. For this reason, three drift correction methods were attempted. The first method by Mesas-Carrascosa et al. (2018) uses tie-points to extract temperature values of all images that overlap with each individual tie-point. The second method discussed by Wang et al. (2023) uses the overlap between sequential images to calculate the accumulative drift. The last method by Malbéteau et al. (2021) first corrects for temperature differences in each flightline and uses the corrected flightlines to correct each sequential flightline. For each correction the same data was used, consisting of the orthophotos generated for the orthomosaic where the ultra-high DPC quality, mild DPC depth filtering, and the disabled blending mode settings were used. The raw thermal images were not used, as they do not contain a projection. They all appear in the same geolocation if plotted, thus they could not be used to calculate differences in overlapping areas.

The tie-point based drift correction method assumes that temperature values at the same tie-point is different across images (Figure 3). The T temperature is measured at a moment in t time. The T at t_0 is the first temperature measured of a tie-point. This temperature was subtracted from each T at later instances of t, to calculate how much T changes over time. This calculation occurred within the same (t_1, t_2, t_3) and adjacent (t_m, t_{m+1}) flightlines. The temperature difference was then averaged per timestamp. A trendline was plotted through the averaged differences in T over t. The slope and intercept values of this trendline were used to correct pixel values at intervals of t (Mesas-Carrascosa et al., 2018). For this process the tie-points acquired from the co-alignment of multispectral and thermal data were used, due to issues with the thermal only DPC's.

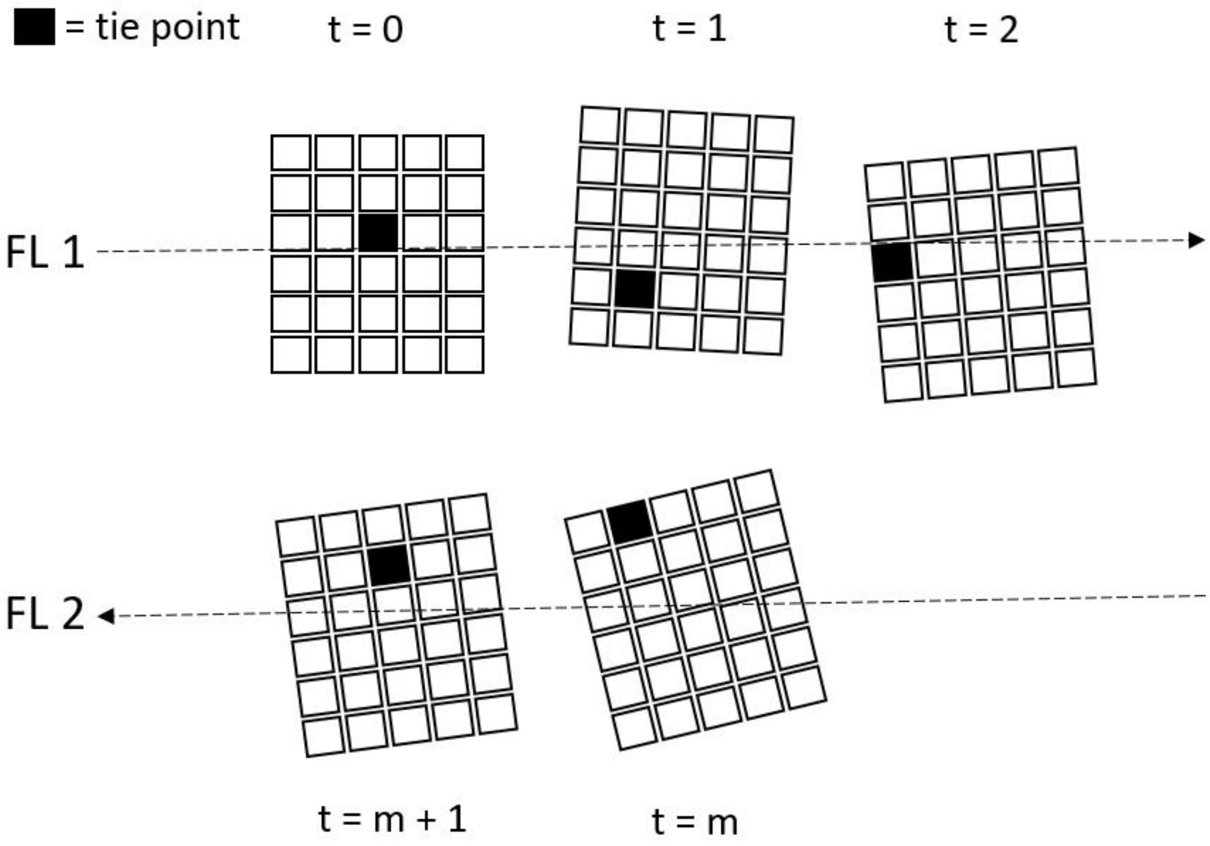

$$T_{t_0} \neq T_{t_1} \neq T_{t_2} \neq T_{t_3} \neq T_{t_m} \neq T_{t_{m+1}}$$

Figure 3 Adaptation of the overview of the drift correction method as proposed by Mesas-Carrascosa et al. (2018). *The black pixels represent the same location that is present in several images, at different time intervals (T is temperature, t is time, t = m stands for an unknown time value in the adjacent flightline)*

The drift correction method by Z. Wang et al. (2023) utilizes the overlap of subsequent image pairs to correct thermal drift. Temperature differences within overlapping areas should theoretically be non-existent. Assuming the theoretical mean difference of zero, a mean difference higher or lower than zero was assumed to be drift. The difference in overlapping pixels was calculated for image pairs. This difference was subtracted from the second image in each pair. Each corrected image was used to correct the next image, thus introducing an accumulative correction with reference to the first image. The formula for this correction is:

$$T_{i+1}^{corrected} = \begin{cases} T_{i+1} - \left(\sum_{j=2}^{i+1} C_{T,j}\right) - C_{T,1}, i \geq 1 \\ T_{i+1} - C_{T,1}, i = 0 \end{cases} \tag{1}$$

Where $T_{i+1}^{corrected}$ is the temperature after removing the calculated thermal drift of the *i + 1th* image, T_{i+1} is the temperature of the *i + 1th* image, $C_{T,j}$ is the temporal temperature drift of the jth image based on the theoretical mean difference of 0, and $C_{T,1}$ denotes the temperature drift at the first image. While the author utilized overlapping tie-points for this correction, overlapping pixels were used in this project. This approach was preferred over the tie-point approach, given the high computational load of the tie-point based drift correction. Consequently, the resultant temperature differences may differ from a tie-point based approach.

The last correction method applied was the swath-based approach to correct for temperature variations by Malbéteau et al. (2021). This mosaicking method was proposed as an alternative to the blending modes in Agisoft Metashape for thermal imagery, with consideration for temperature changes throughout the flight. Temperature variations in each individual flightline were corrected by averaging overlapping pixel values of adjacent images. As most images were taken within 3 seconds from each other, the temperature change between subsequent images was expected to be minimal. All images within a flightline were merged into a single swath. The mean difference between the first two adjacent flightlines was calculated, and used to correct images of the second flightline. The second (corrected) flightline was used to correct the images of the third flightline, and so on. This approach ensures that the correction applied to the last flightline is still affected by the influence of the first one.

The impact of each drift correction method was assessed by calculating the root mean squared error (RMSE), mean absolute error (MAE), and R^2 compared to ground reference measurements. The resultant metrics were compared to the metrics of the orthomosaic of which the used orthophotos originated from. Additionally, the original orthomosaic that was generated in Metashape was subtracted from each of the corrected orthomosaics. The outcomes consisted of influence maps, that depict on what location of the research area the corrections had the most impact.

2.2.3 Influence assessment

Following the investigations into the thermal drift, a thorough assessment of the impact of the SfM parameter selection on resultant orthomosaic temperatures was performed. Due to uncertainties revealed during the accuracy assessment and the thermal drift correction attempts, this part of the analysis focused on relative temperature changes. For this purpose the local one-at-a-time sensitivity analysis was performed (equation (2)). This type of sensitivity analysis requires a baseline of settings to test parameter influences with. In the equation $\Delta_i^+ y$ depicts the change caused by a parameter setting, $x_i + \Delta x_i^+, x_{\sim i}^0$ depicts that the setting for parameter x_i is changed whilst keeping the other parameters, $x_{\sim i}^0$, the same. The baseline case is depicted as x^0 (Borgonovo & Plischke, 2016). The calculations were performed on the orthomosaics that were masked to fit the 36 2 x 2 meter grass plots.

$$\Delta_i^+ y = g\left(x_i + \Delta x_i^+, x_{\sim i}^0\right) - g(x^0) \tag{2}$$

To compare the outcomes of the sensitivity analyses, the resultant influence values were plotted in violin plots and boxplots. The distribution of the influence values was assessed by comparing mean values, interquartile ranges, standard deviations, the extent of boxplot whisker bounds, and the percentage of values within the interquartile range and boxplot whiskers.

2.2.4 Parameter influence on temperatures

Most of the parameters contain a setting that performs no calculations, which makes these settings a suitable baseline setting. For the DPC quality parameter this setting is the ultra-high quality. The ultra-high quality setting uses the native image resolution for the creation of the DPC. Each step down in quality down-samples the resolution, thus changing the input data (Agisoft, 2023). For the DPC depth filtering parameter, the setting that does not perform calculations is the disabled setting. The impact of colour calibration was omitted by simply not performing colour calibration. No baseline setting was set for the blending mode. While it can be set to disabled, it still alters the input imagery (Figure 7). Consequently, three separate baselines were created for each of the other processing parameters, considering the three blending mode settings.

By disabling all settings, the resulting influence metric represents purely the influence of one setting under each of the blending modes. To assess the impact of the DPC quality parameter the baseline was subtracted from orthomosaics generated with the high, medium, low and lowest quality settings with all other parameter settings set to disabled. The same calculation was performed for the DPC depth filtering and colour calibration settings using their respective parameters.

The influence of the blending modes was determined by comparing the temperature distributions in orthomosaics generated with each of the blending modes. The other parameter settings were set to the ultra-high DPC quality setting, the disabled DPC depth filtering setting, and no colour calibration was applied.

2.2.5 Multi-parameter influence

Following the assessment of individual parameters, the combined influence of parameters was assessed. The multi-parameter influences were calculated between the DPC quality and depth filtering settings, the colour calibration and DPC quality settings, and the colour calibration and DPC depth filtering settings. For this analysis only parameter settings with a substantial effect on orthomosaic temperatures were considered.

The combined influence of the DPC quality and depth filtering settings was determined through calculating the quality influence at each of the four depth filtering settings. The baseline for this calculation consisted of the ultra-high quality setting and no colour calibration. The baseline orthomosaics were subtracted from orthomosaics generated at the high, medium low and lowest quality settings. These calculations were performed for each of the DPC depth filtering settings (disabled, mild, moderate, and aggressive). The baseline values changed to match the DPC depth filtering setting that was applied. The outcome consisted of the combined influence of the DPC quality and depth filtering settings on orthomosaic temperatures. The resultant values were plotted in violin plots.

The combined influence of the DPC quality settings with colour calibration, and the DPC depth filtering settings with colour calibration, were calculated in a similar fashion. For both calculations the baseline consisted of the ultra-high quality setting and the disabled depth filtering setting. The influence of the quality settings and depth filtering settings was separately calculated through a one-at-a-time sensitivity analysis with the aforementioned baseline. These calculations were performed with and without colour calibration. The baseline changed depending on whether colour calibration was performed (No, DEM). The outcome of the calculations consisted of the combined influence of the DPC quality settings (high, medium, low, and lowest) with and without the colour calibration settings, and the depth filtering settings (mild, moderate, and aggressive) with and without colour calibration. The resultant values were plotted in violin plots.

3 Results

3.1 Quality assessment

Out of the 360 projected orthomosaics, only 180 were generated with the parameters discussed in Table 1. Despite successful image alignment, Metashape was unable to generate full DPCs based on thermal imagery that was not co-aligned with multispectral imagery. Large holes formed at the location of the grass field (Figure 4). A total of 9 orthomosaics were created from a tie-point based DEM. Consequently, these orthomosaics were not influenced by the DPC quality and depth filtering settings. This impeded any direct comparison between co-aligned and thermal-only based orthomosaics. For this reason, no sensitivity analysis was performed with regards to the impact of co-alignment on orthomosaic temperatures. The 9 thermal-only based orthomosaics were omitted from further analysis.

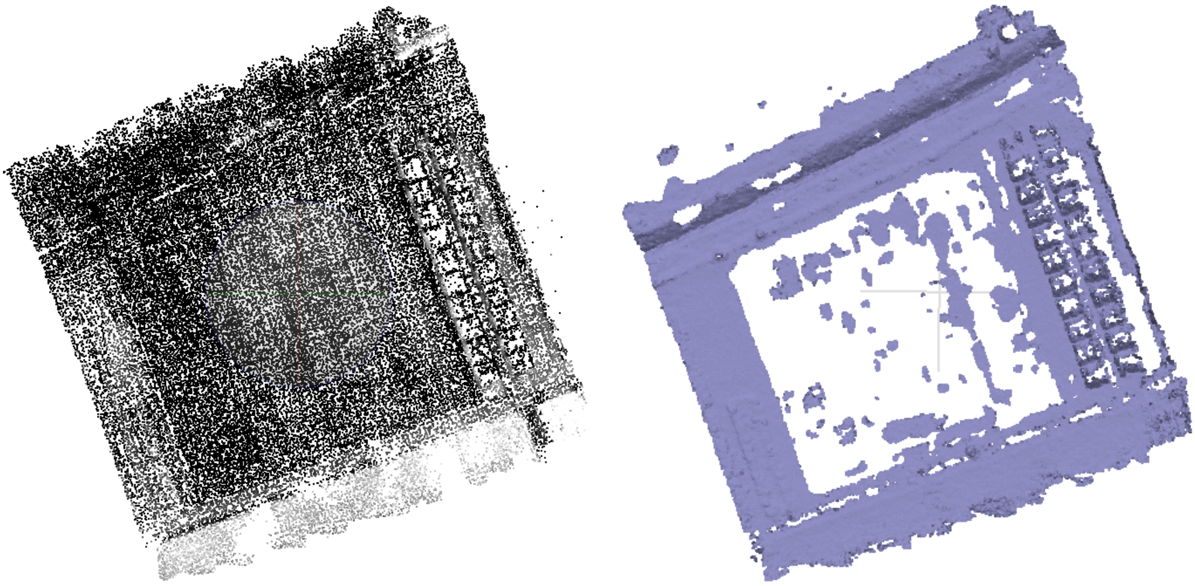

Figure 4 Thermal only sparse point cloud (left), thermal only dense point cloud based on the sparse point cloud (right).

The comparison of the remaining 180 orthomosaics to ground reference values resulted in RMSEs between 2.4 °C to 3.3 °C, MAEs of 2.1 °C to 2.9 °C, and a R^2 between 1.9×10^{-2} to 6.9×10^{-2} after empirical line correction. The highest RMSE and MAE values were produced by orthomosaics that were not colour calibrated (appendix F). Of these orthomosaics, those generated with the disabled blending mode produced the highest error, followed by the mosaic and average blending modes. Colour calibrated orthomosaics produced the smallest errors, with limited difference in errors between the blending modes. The high errors and low R^2 can potentially be attributed to the large variation in ground reference values and the eastward temperature increase visible in orthomosaics.

The maximum difference in the ground reference measurements is 3.6 °C, and no clear increasing or decreasing pattern is visible in the temperatures (appendix G). Most grass temperatures in the orthomosaics had a higher temperature than the ground reference measurements. The difference between the orthomosaic temperatures and ground reference measurements increased towards the eastern side of the grass field (appendix H). This may indicate the influence of thermal drift on the orthomosaics, especially given the decrease in focal plane array (FPA) temperature during the flight (Figure 5). The FPA temperature decreased rapidly at the beginning of the flight before stabilizing. The FPA temperature reduced by 5.5 °C in the first 200 seconds, and by a total of 7 °C throughout the flight.

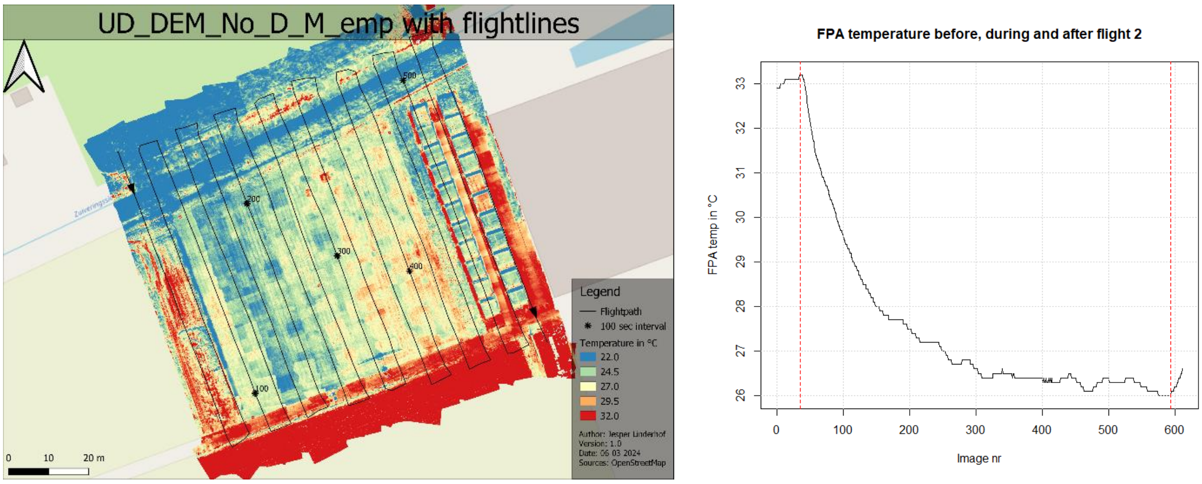

Figure 5 Orthomosaic processed with the ultra-high DPC quality setting, disabled DPC depth filtering, no colour calibration and disabled blending mode (left). FPA temperature throughout the flight (right), where the first vertical dashed line depicts the start of the flight, and the second dashed line depicts the end of the flight.

3.2 Drift assessment

To assess whether the decrease in FPA temperature had an effect on the temperature in the orthomosaics, three correction methods were applied. These corrections were applied to the orthophotos of an orthomosaic created with the ultra-high DPC quality setting, the mild DPC depth filtering setting, no colour calibration and the disabled blending mode (henceforth referred to as the original orthomosaic). The impact of each method was assessed through a visual assessment and by comparing the accuracy of the corrected orthomosaics with the original orthomosaic. The original orthomosaic had a RMSE, MAE, and R^2 of 3.29 °C, 2.93 °C and 2.6×10^{-2} compared to ground reference measurements.

The tie-point based correction method had the least influence on orthomosaic temperatures. The sub-result of this method consists of the calculated thermal drift in °C/s as a function of the flight time in seconds (appendix I). The calculated drift was small and decreased temperatures, with an average calculated drift of -9×10^{-3} °C. Applying this linear drift correction to the orthophotos resulted in an orthomosaic with sporadic temperature increases of a few thousandths of a degree Celsius (Figure 6). Additionally, the accuracy metrics worsened compared to the original orthomosaic, given its RMSE, MAE, and R^2 of 3.29 °, 2.94 °C, and 2.6×10^{-2}.

The swath-based correction was able to remove most of the presumed anomalies. Many warmer spots in the eastern part of the orthomosaic were alleviated, and the temperatures became overall more uniform (Figure 6). The correction patterns are similar between the colour calibrations and the swath-based correction. However, it had a greater influence on orthomosaic temperatures than the colour calibrations in Metashape. The temperature in the corrected orthomosaic is on average 1.38 °C lower than in the original orthomosaic. It is visually more comparable to the DEM and tie-point based colour calibrated versions of the original orthomosaic, although its temperatures are still 0.51 °C and 0.45 °C lower respectively. The swath-based correction had the most positive influence on the accuracy metrics given its RMSE, MAE, and R^2 of 2.05 °C, 1.73 °C, and 0.16.

The accumulative correction resulted in the least viable orthomosaic. The bias between images accumulated rapidly over the flight, which led to unrealistic temperature corrections (Figure 6). The flightline patterns are clearly visible, and with each flightline the temperature increased in the flight direction. The accumulated sum for the drift correction amounted to 21.8 °C. This orthomosaic was not empirically corrected, as this stretched the minimum and maximum values to 10 °C to 80 °C. The resultant RMSE, MAE, and R^2 were 17.7 °C, 17.2 °C, and 3.6×10^{-2}.

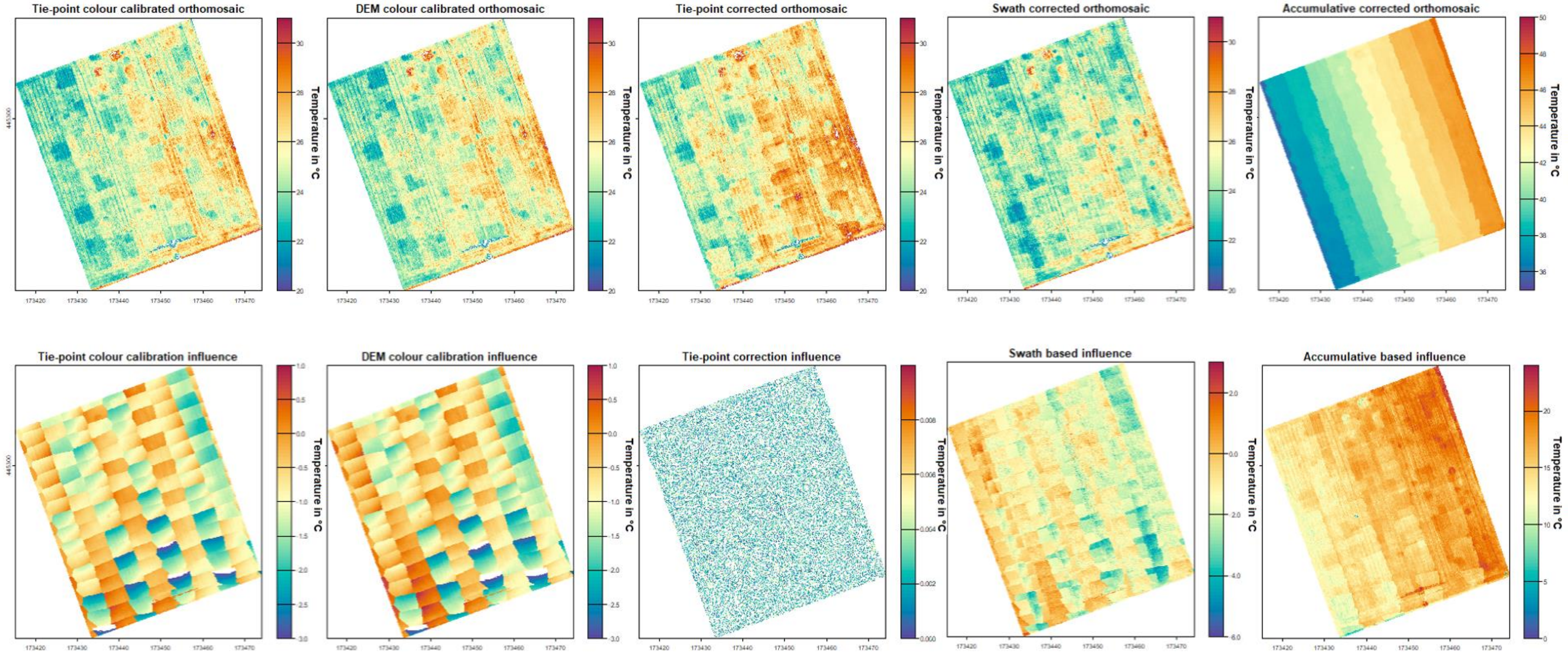

Figure 6 Resultant orthomosaics after the applying the colour calibration settings in Agisoft Metashape, and orthomosaics after the three corrections were applied (top row). The influence on orthomosaic temperatures was calculated by subtracting the original orthomosaic from each corrected orthomosaic (bottom row).

3.3 Parameter influence on temperatures

Violin plots were made for the 180 orthomosaics that were generated using all parameter settings. Wherever possible, boxplots were added in the violin plots to provide more understanding of the value distributions. The impact values themselves are not normally distributed, due to long tails at the lower and higher ends of the distributions. Wherever the impact of settings was similar, the values of all 36 plots were aggregated into one violin plot. This part of the report discusses the impact of the blending modes, DPC quality, DPC depth filtering, and colour calibration on orthomosaic temperatures.

3.3.1 Blending mode

The choice of blending mode had a large influence on orthomosaic temperatures. The blending patters became visible when a non-colour calibrated orthomosaic was subtracted from a colour calibrated orthomosaic (Figure 7). The pattern of the average blending mode does not show any locations where colour calibration reduced temperatures by more than -1.5 °C, and shows clear seamlines between overlapping images. In contrast, the mosaic blending mode retained more of the temperature reductions. Furthermore, it shows an outward circular pattern at nadir locations of images, compared to the rectangular shapes visible with the average and disabled blending modes. The disabled blending mode does not mix pixel values, yet only retains the middle portion of the images to create the orthomosaic. As it does not mix pixel values, the impact of the colour calibration was preserved most at this blending mode.

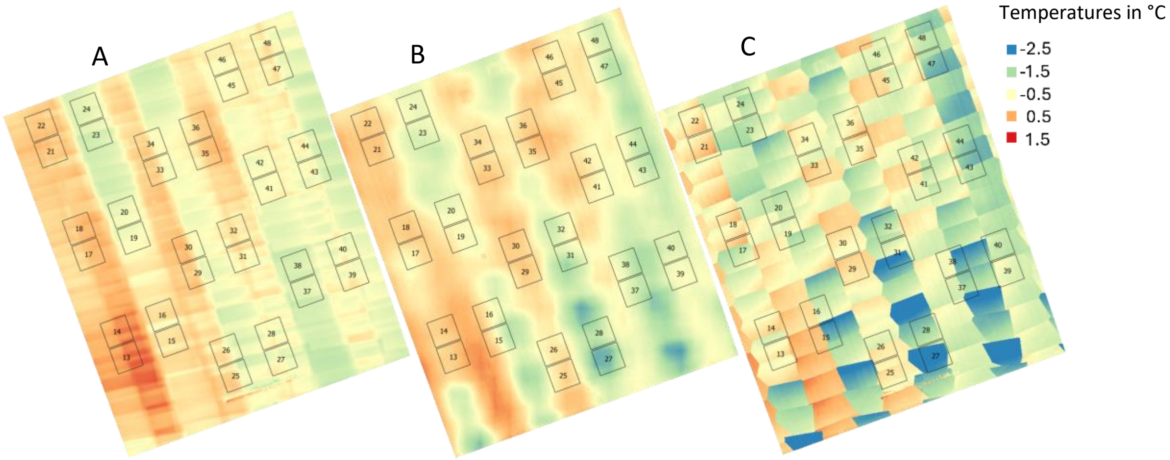

Figure 7 Influence of DEM based colour calibration (ultra-high DPC quality, mild DPC depth filtering setting, DEM based colour calibration). The non-colour calibrated version of the same orthomosaic was subtracted from the colour calibrated version to calculate these maps. A: colour calibration impact with the average blending mode. B: colour calibration impact with the mosaic blending mode. C: colour calibration impact with the disabled blending mode.

The disabled blending mode produced the highest temperatures, and the average and mosaic blending modes produced the lowest temperatures. Blending modes that produced the highest and lowest orthomosaic temperatures differed 0.61 °C on average across the grass plots, with a maximum difference of 1.94 °C. Depending on the temperature differences between adjacent images, the influence of the blending modes on orthomosaic temperatures differed. This observation is underpinned by the temperature distributions of orthomosaics made with the three blending modes across the 36 grass plots (Figure 8). The shape of distributions differed between grass plots, caused by the differing ways in which the blending modes handle pixel blending. In many grass plots, like 19, 20, and 21, the blending modes show similar distributions. In these cases, the blending modes produced similar temperatures, and were similarly colour calibrated (Figure 7). However, the blending modes performed differently in some plots. The most extreme example is grass plot 27, where at the disabled blending mode the colour calibration algorithm subtracted roughly -2.5 °C from the measured temperature. The application of the mosaic blending mode alleviated some of the temperature reduction, whereas the average blending mode caused a temperature increase in grass plot 27.

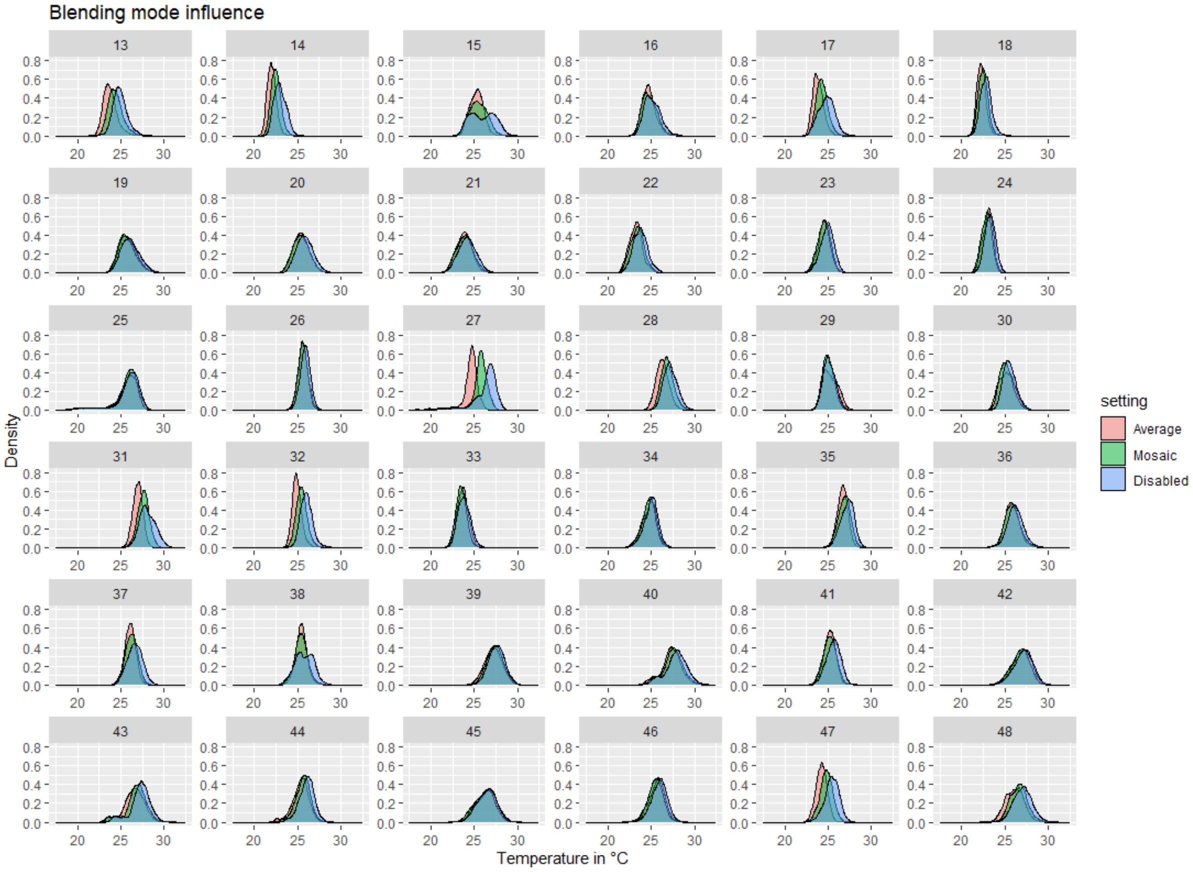

Figure 8 Density plot of temperature distributions in the 36 large grass plots at different blending mode settings. Orthomosaics with the ultra-high DPC quality setting, disabled DPC depth filtering setting and no colour calibration were used.

3.3.2 Dense point cloud quality

The influence of the DPC quality settings varied between blending modes, as is visible in the distributions of the influence values (Figure 9, Table 2). The influence of the quality settings was greatest when combined with the mosaic blending mode, and limited with the average and disabled blending modes. The influence of the quality settings was similar across all 36 grass plots, with the exception of plots 42 and 45 if the quality settings were combined with either the average or disabled blending mode (appendix J).

The influence of the quality settings was similar with the average and disabled blending modes. The average influence on orthomosaic temperatures was near zero degrees Celsius with both modes, and the distribution of influence values was similar across quality settings. However, the distribution of influence values was slightly larger with the disabled blending mode. The interquartile ranges (IQRs) and the range between the lower and upper boxplot whisker bounds were greater with the disabled blending mode compared to the average blending mode. Furthermore, the disabled blending mode produced a higher number of outliers. A total of 89% of all influence values remained within the whisker bounds if the disabled blending mode was used. This percentage was 94% with the average blending mode.

The influence of the DPC quality settings increased when the mosaic blending mode was utilized. It caused most quality settings to increase orthomosaic temperature values on average, with the exception of the medium quality setting (Figure 9, Table 2). Both the IQRs and the lower and upper boxplot whisker bounds were greater with the mosaic blending mode than with the average or disabled blending modes. A total of 95% to 96% of all influence values remained between the whisker bounds.

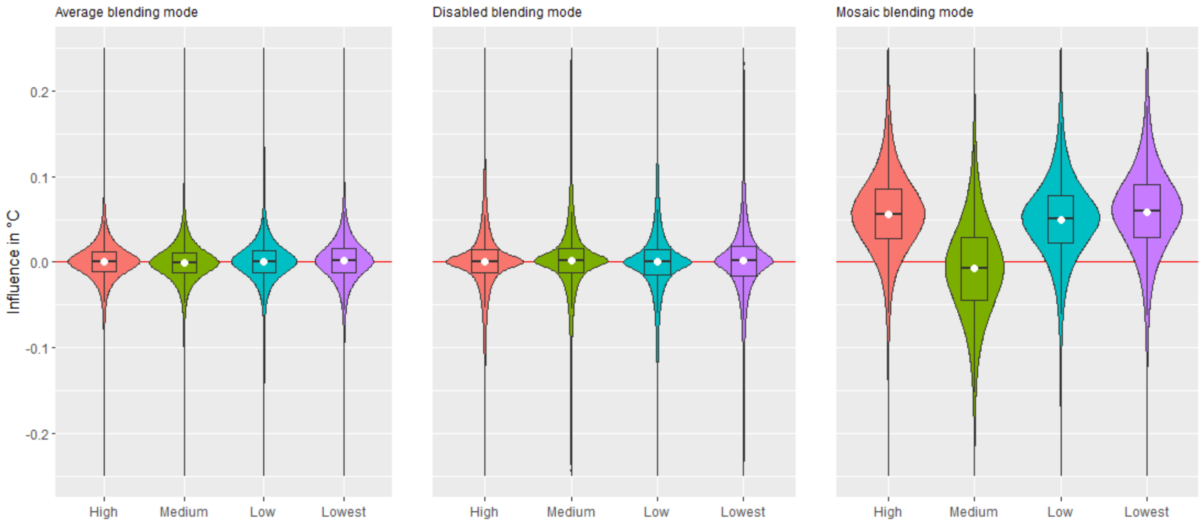

Figure 9 Violin plots of the quality influence on orthomosaic temperature values of all 36 plots combined. The whiskers of the boxplots depict the 1.5 x IQR range. The white dots show the average values. This plot does not show the range of the outliers.

Table 2 Distribution metrics of the temperature influence of the dense point cloud quality settings with the three blending modes. The mean, interquartile range (IQR), and the upper and lower boxplot whisker bounds (1.5 x IQR) are shown. All IQRs represent 50% of all influence values.

DPC quality setting, metric	**Average blending mode**	**Disabled blending mode**	**Mosaic blending mode**
High quality, mean in °C	2.7 x 10^{-4}	6.9 x 10^{-4}	5.6 x 10^{-2}
Medium quality, mean in °C	-9 x 10^{-4}	2 x 10^{-3}	-7.9 x 10^{-3}
Low quality, mean in °C	5.2 x 10^{-4}	6.8 x 10^{-5}	5 x 10^{-2}
Lowest quality, mean in °C	1.5 x 10^{-3}	1.3 x 10^{-3}	6 x 10^{-2}
High quality, IQR in °C	-1.1 x 10^{-2} – 1.2 x 10^{-2}	-1.3 x 10^{-2} – 1.5 x 10^{-2}	2.7 x 10^{-2} – 8.5 x 10^{-2}
Medium quality, IQR in °C	-1.3 x 10^{-2} – 1.1 x 10^{-2}	-1.2 x 10^{-2} – 1.6 x 10^{-2}	-4.4 x 10^{-2} – 2.8 x 10^{-2}
Low quality, IQR in °C	-1.2 x 10^{-2} – 1.4 x 10^{-2}	-1.5 x 10^{-2} – 1.5 x 10^{-2}	2.2 x 10^{-2} – 7.9 x 10^{-2}
Lowest quality, IQR in °C	-1.3 x 10^{-2} – 1.6 x 10^{-2}	-1.6 x 10^{-2} – 1.9 x 10^{-2}	2.9 x 10^{-2} – 9.1 x 10^{-2}
High quality, bounds in °C	-4.7 x 10^{-2} – 4.8 x 10^{-2}	-5.4 x 10^{-2} – 5.6 x 10^{-2}	-6 x 10^{-2} – 0.17
Medium quality, bounds in °C	-4.9 x 10^{-2} – 4.7 x 10^{-2}	-5.5 x 10^{-2} – 5.9 x 10^{-2}	-0.15 – 0.14
Low quality, bounds in °C	-5 x 10^{-2} – 5.2 x 10^{-2}	-6.1 x 10^{-2} – 6.1 x 10^{-2}	-6.2 x 10^{-2} – 0.16
Lowest quality, bounds in °C	-5.6 x 10^{-2} – 5.9 x 10^{-2}	-6.8 x 10^{-2} – 7.1 x 10^{-2}	-6.3 x 10^{-2} – 0.18

3.3.3 Dense point cloud depth filtering

The influence of the DPC depth filtering settings on orthomosaic temperatures was limited. The majority of influence values of the depth filtering setting were near zero degrees Celsius (Figure 10, Table 3). The influence of the depth filtering settings was greatest when combined with the mosaic blending mode. The influence of the depth filtering settings was similar across all 36 grass plots. Most variation occurred with the mosaic blending mode enabled (appendix K).

The influence of the DPC depth filtering settings was limited when the average and disabled blending modes were used. Most influence values were distributed near zero degrees Celsius with these blending modes (Figure 10, Table 3). Furthermore, the influence of the aggressive and moderate settings on orthomosaic temperatures was comparable with these blending modes. The mild setting produced the least influence. The temperature influence was slightly greater with the disabled blending mode, given the greater IQRs and greater lower and upper boxplot whisker bounds compared to the average blending mode. The disabled blending mode produced the greatest number of outliers, as 86% of all influence values were represented by the lower and upper whisker bounds at the aggressive and moderate settings, and 91% at the mild setting. With the average blending mode, percentages reached 94% with the aggressive and moderate settings, and 97% with the mild setting.

The influence of the DPC depth filtering settings was greatest with the mosaic blending mode. The temperature influence values became more varied, and a clear difference between the distributions at the aggressive and moderate settings occurred (Figure 10, Table 3). The mean influence values, IQRs and ranges between the lower and upper whisker bounds of the depth filtering settings were highest with the mosaic blending mode. A total of 97% of temperature influence values remained within the boxplot whisker bounds at the moderate and mild settings. At the aggressive setting the percentage increased to 98%.

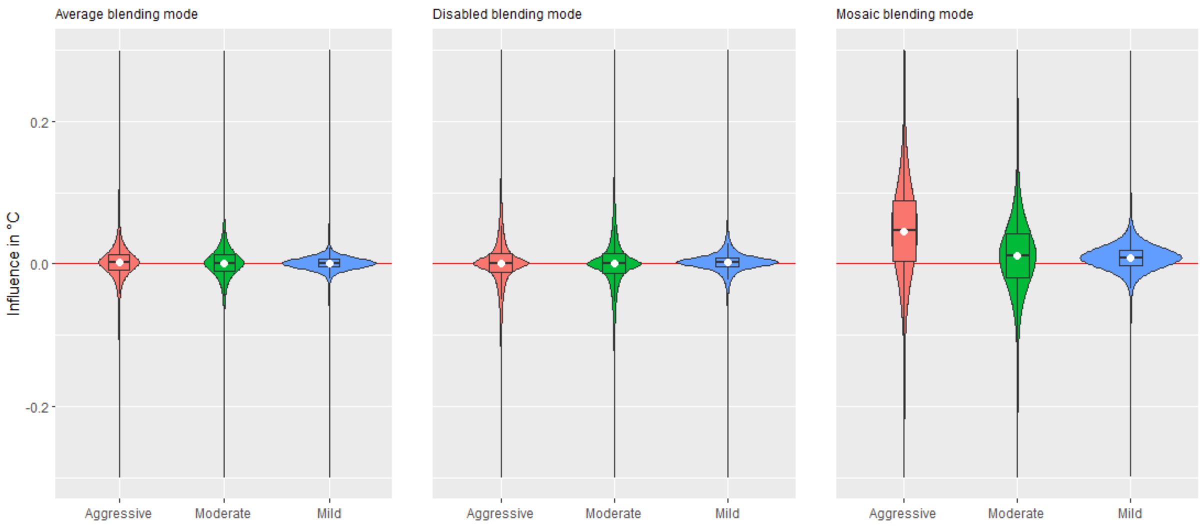

Figure 10 Violin plots of the depth filtering influence on orthomosaic temperature values of all 36 plots combined. The whiskers of the boxplots depict the 1.5 x IQR range. The white dots show the average values. This plot does not show the range of the outliers.

Table 3 Distribution metrics of the temperature influence of the dense point cloud depth filtering settings with the three blending modes. The mean, interquartile range (IQR), and the upper and lower boxplot whisker bounds (1.5 x IQR) are shown. All IQRs represent 50% of all influence values.

DPC depth filtering setting, metric	**Average blending mode**	**Disabled blending mode**	**Mosaic blending mode**
Aggressive, mean in °C	2 x 10^{-3}	9.8 x 10^{-3}	4.7 x 10^{-2}
Moderate, mean in °C	8.5 x 10^{-4}	2.9 x 10^{-3}	1.1 x 10^{-2}
Mild, mean in °C	6.4 x 10^{-4}	2.4 x 10^{-2}	8.8 x 10^{-3}
Aggressive, IQR in °C	-9.2 x 10^{-3} – 1.3 x 10^{-2}	-1.2 x 10^{-2} – 1.4 x 10^{-2}	3.5 x 10^{-3} – 8.9 x 10^{-2}
Moderate, IQR in °C	-1.1 x 10^{-2} – 1.3 x 10^{-2}	-1.3 x 10^{-2} – 1.4 x 10^{-2}	-2 x 10^{-2} – 4.2 x 10^{-2}
Mild, IQR in °C	-4.7 x 10^{-3} – 6.3 x 10^{-3}	-3.8 x 10^{-3} – 8.8 x 10^{-3}	-2.2 x 10^{-3} – 2 x 10^{-2}
Aggressive, bounds in °C	-4.3 x 10^{-2} – 4.8 x 10^{-2}	-5.1 x 10^{-2} – 5.3 x 10^{-2}	-0.12 – 0.22
Moderate, bounds in °C	-4.5 x 10^{-2} – 4.7 x 10^{-2}	-5.3 x 10^{-2} – 5.4 x 10^{-2}	-0.11 – 0.13
Mild, bounds in °C	-2.1 x 10^{-2} – 2.3 x 10^{-2}	-2.3 x 10^{-2} – 2.8 x 10^{-2}	-3.5 x 10^{-2} – 5.3 x 10^{-2}

3.3.4 Colour calibration

The influence of colour calibration on orthomosaic temperatures fluctuated greatly between grass plots, yet mostly lowered orthomosaic temperatures (Figure 11, appendix L). The DEM based colour calibration had a higher variation in influence values than the tie-point based colour calibration. While the mean values, IQRs, and ranges between the lower and upper boxplot whiskers were similar between the colour calibration settings, the standard deviations differed (Table 4). To illustrate, the mean values of the colour calibration impacts were plotted in aggregated boxplots (Figure 11). The jittered dots represent the mean influence values of the 36 grass plots. The blending modes had a large influence on the distribution of the colour calibration influence on orthomosaic temperatures.

The influence of the colour calibration settings on orthomosaic temperatures differed between blending modes (Figure 11). The colour calibrations had the least influence when combined with the average blending mode. This is reflected in the mean value and the standard deviation. Colour calibration had the most influence on orthomosaic temperatures with the disabled blending mode given the mean value, yet also had the most spread in both the IQR and the range between the lower and upper bounds of the boxplot whiskers. The influence of colour calibration combined with the mosaic blending mode was between the average and disabled blending modes.

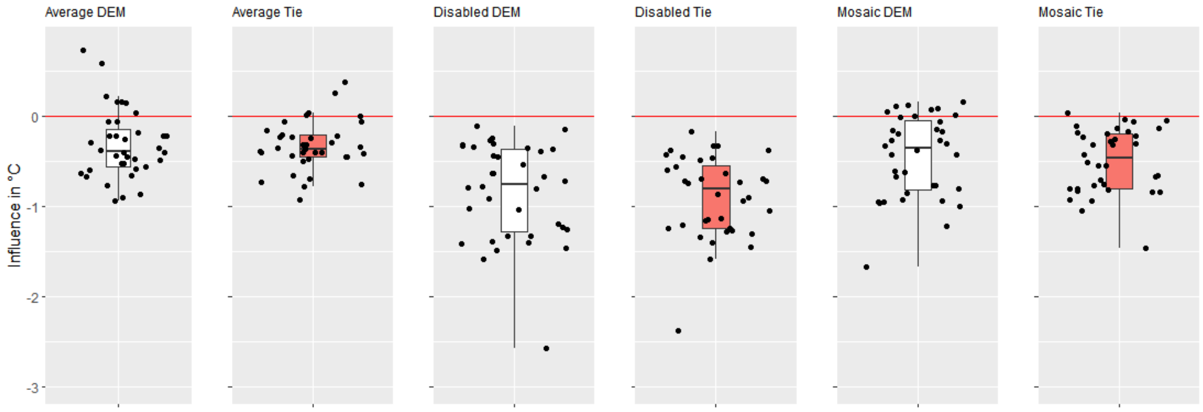

Figure 11 Aggregated boxplots of mean colour calibration influences on orthomosaic temperatures. The black dots represent all mean influence values of colour calibration at each of the 36 grass plots. From left to right, the colour calibration influence at the average, disabled, and mosaic blending modes are represented. The DEM based colour calibration is represented in white, the tie-point based colour calibration in red.

Table 4 Distribution metrics of the colour calibration settings with each of the blending modes, averaged from all 36 grass plots. The mean of all means depicted in the boxplots above, the standard deviation between the mean values, the average range between the first and third quartile, and the range between the lower and upper boxplot whisker bounds are shown.

Colour calibration setting, metric	**Average blending mode**	**Disabled blending mode**	**Mosaic blending mode**
DEM, mean in °C	-0.31	-0.85	-0.46
Tie-point, mean in °C	-0.33	-0.91	-0.51
DEM, stdev of means in °C	0.39	0.55	0.46
Tie-point, stdev of means in °C	0.28	0.46	0.36
DEM, average IQR in °C	0.28	0.59	0.28
Tie-point, average IQR in °C	0.28	0.57	0.28
DEM, range of bounds in °C	1.11	2.36	1.14
Moderate, range of bounds in °C	1.12	2.30	1.13

3.4 Multi-parameter influence

3.4.1 DPC quality & DPC quality

The combined influence of DPC quality and DPC depth filtering settings was only assessed with the mosaic blending mode enabled. The assessment was not performed with the disabled and average blending modes, given the low influence of the quality and depth filtering settings when combined with either of these blending modes (Figure 9, Figure 10).

The setting combinations showed similar patterns across quality settings, with the exception of the medium quality (Figure 12 b). In contrast to the other quality settings, combinations with the medium quality setting generally lowered orthomosaic temperatures. With the other quality settings, combinations with the disabled and mild depth filtering settings had the highest temperature influence. This is reflected by both the mean values, the IQRs and the boxplot whisker bounds (Table 5). Combining quality settings with the moderate and aggressive depth filtering settings produced the least influence (Figure 12 a, c, d). The extent of the influence differed between setting combinations. To illustrate, the combinations of the disabled, mild, and moderate settings with the low quality setting produced similar average temperatures (Figure 12 c, Table 5). In contrast, the combination of the mild and moderate settings with the lowest quality setting had a smaller influence than with the disabled setting (Figure 12 d).

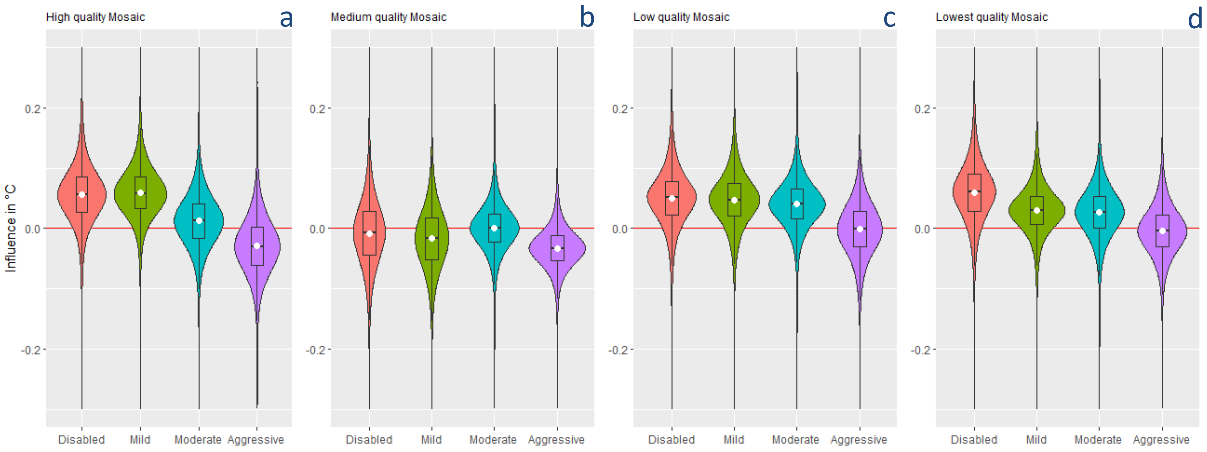

Figure 12 Violin plots of the combined influence of DPC quality and depth filtering settings on orthomosaic temperatures, aggregated from all 36 grass plots. Each plot represents a different quality setting (a through d) combined with all depth filtering settings on the x-axis. The whiskers of the boxplots depict the 1.5 x IQR range. The white dots show the average values. This plot does not show the range of the outliers.

Table 5 Distribution metrics of the combined influence of DPC quality and depth filtering settings with the mosaic blending mode, based on the aggregated values of all 36 grass plots. The mean, *interquartile range (IQR) and lower and upper boxplot whisker bounds are given for each combination between the DPC quality and depth filtering settings. All IQRs represent 50% of all influence values.*

DPC depth filtering setting, metric	**High quality**	**Medium quality**	**Low quality**	**Lowest quality**
Aggressive, mean in °C	-2.9 x 10^{-2}	-3.3 x 10^{-2}	-1.4 x 10^{-3}	-3.8 x 10^{-3}
Moderate, mean in °C	1.2 x 10^{-2}	8.2 x 10^{-4}	4.1 x 10^{-2}	2.7 x 10^{-2}
Mild, mean in °C	5.9 x 10^{-2}	-1.7 x 10^{-2}	4.7 x 10^{-2}	3.1 x 10^{-2}
Disabled, mean in °C	5.6 x 10^{-2}	-7.9 x 10^{-3}	5.1 x 10^{-2}	6 x 10^{-2}
Aggressive, IQR in °C	-6 x 10^{-2} – 1.5 x 10^{-3}	-5.4 x 10^{-2} – -1.2 x 10^{-2}	-3.1 x 10^{-2} – 2.9 x 10^{-2}	-3.1 x 10^{-2} – 1.2 x 10^{-2}
Moderate, IQR in °C	-1.6 x 10^{-2} – 4.1 x 10^{-2}	-2.3 x 10^{-2} – 2.4 x 10^{-2}	1.6 x 10^{-2} – 6.5 x 10^{-2}	5.9 x 10^{-4} – 5.4 x 10^{-2}
Mild, IQR in °C	3.2 x 10^{-2} – 8.6 x 10^{-2}	-5.1 x 10^{-2} – 1.7 x 10^{-2}	2 x 10^{-2} – 7.4 x 10^{-2}	7.2 x 10^{-3} – 5.4 x 10^{-2}
Disabled, IQR in °C	2.7 x 10^{-2} – 8.5 x 10^{-2}	-4.4 x 10^{-2} – 2.8 x 10^{-2}	2.2 x 10^{-2} – 7.9 x 10^{-2}	2.9 x 10^{-2} – 9.1 x 10^{-2}
Aggressive, bounds in °C	-0.15 – 9.4 x 10^{-2}	-0.12 – 5 x 10^{-2}	-0.12 – 0.12	-0.11 – 0.10
Moderate, bounds in °C	-0.10 – 0.13	-9.4 x 10^{-2} – 9.6 x 10^{-2}	-5.6 x 10^{-2} – 0.14	-7.9 x 10^{-2} – 0.13
Mild, bounds in °C	-4.7 x 10^{-2} – 0.17	-0.15 – 0.12	-6 x 10^{-2} – 0.15	-6.3 x 10^{-2} – 0.12
Disabled, bounds in °C	-6 x 10^{-2} – 0.17	-0.15 – 0.14	-6.2 x 10^{-2} – 0.16	-6.3 x 10^{-2} – 0.18

3.4.2 Colour calibration & DPC quality

The combined influence of DPC quality settings with colour calibration was only assessed with the DEM based colour calibration. The tie-point based colour calibration was not used, due to the limited impact this setting had on the temperature influence of the quality settings (appendix N).

Combining the DPC quality settings with the DEM based colour calibration resulted in an increased influence on orthomosaic temperatures compared to DPC quality settings without colour calibration (Figure 13). The influence was increased most at the high and low quality settings. The average influence values were increased the least when the disabled or average blending mode were used, although the IQRs and the range between lower and upper boxplot whisker bounds increased (Table 6). The average combined influence of quality settings with colour calibration increased most with the mosaic blending mode enabled, with the exception of the medium quality setting (Figure 13 c, f). However, the IQR and the range between the lower and upper whisker bounds decreased compared to the quality settings without colour calibration. Adding colour calibration increased the percentage of influence values that remained within the whisker bounds. Without colour calibration, a minimum of 94%, 86%, and 96% (average, disabled, and mosaic blending modes) of influence values remained within the whisker bounds across all the quality settings. Adding colour calibration increased the minimum percentages to 97%, 92%, and 94%.

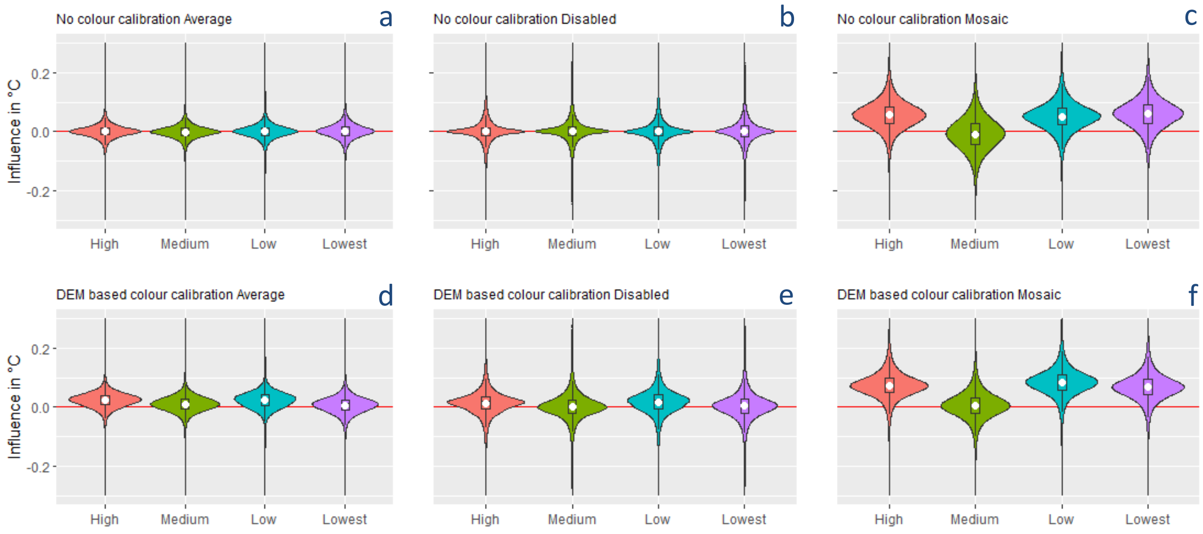

Figure 13 Violin plots of the combined influence of the DEM based colour calibration with DPC quality settings on orthomosaic temperature values of all 36 plots combined. Plots a through c represent the influence of quality settings without colour calibration with the average, disabled, and mosaic blending

modes respectively. Plots d through f represent the influence of quality settings combined with the DEM based colour calibration with the average, disabled, and mosaic blending modes respectively. The whiskers of the boxplots depict the 1.5 x IQR range. The white dots show the average values. This plot does not show the range of the outliers.

Table 6 Distribution metrics of the combined influence of DPC quality settings and DEM based colour calibration, based on the aggregated values of all 36 grass plots. The mean and lower and upper boxplot whisker bounds are given for each combination between the DPC quality and colour calibration settings.

DPC quality setting, colour calibration, metric	**Average blending mode**	**Disabled blending mode**	**Mosaic blending mode**
High quality, No, mean in °C	2.7 x 10^{-4}	6.9 x 10^{-4}	5.6 x 10^{-2}
Medium quality, No, mean in °C	-9 x 10^{-4}	2 x 10^{-3}	-7.9 x 10^{-3}
Low quality, No, mean in °C	5.2 x 10^{-4}	6.8 x 10^{-5}	5.1 x 10^{-2}
Lowest quality, No, mean in °C	1.5 x 10^{-3}	1.3 x 10^{-3}	6 x 10^{-2}
High quality, DEM, mean in °C	2.3 x 10^{-2}	1.4 x 10^{-2}	7.4 x 10^{-2}
Medium quality, DEM, mean in °C	1 x 10^{-2}	1.9 x 10^{-3}	6.3 x 10^{-3}
Low quality, DEM, mean in °C	2.3 x 10^{-2}	1.8 x 10^{-2}	8.4 x 10^{-2}
Lowest quality, DEM, mean in °C	6.3 x 10^{-3}	3.5 x 10^{-3}	6.8 x 10^{-2}
High quality, No, bounds in °C	-4.7 x 10^{-2} – 4.8 x 10^{-2}	-5.4 x 10^{-2} – 5.6 x 10^{-2}	-6 x 10^{-2} – 0.17
Medium quality, No, bounds in °C	-4.9 x 10^{-2} – 4.7 x 10^{-2}	-5.5 x 10^{-2} – 5.9 x 10^{-2}	-0.15 – 0.14
Low quality, No, bounds in °C	-5 x 10^{-2} – 5.2 x 10^{-2}	-6.1 x 10^{-2} – 6.1 x 10^{-2}	-6.2 x 10^{-2} – 0.16
Lowest quality, No, bounds in °C	5.6 x 10^{-2} – 5.9 x 10^{-2}	-6.8 x 10^{-2} – 7.1 x 10^{-2}	-6.3 x 10^{-2} – 0.18
High quality, DEM, bounds in °C	-4 x 10^{-2} – 8.8 x 10^{-2}	-6.8 x 10^{-2} – 9.5 x 10^{-2}	-2.3 x 10^{-2} – 0.17
Medium quality, DEM, bounds in °C	-5.6 x 10^{-2} – 7.7 x 10^{-2}	-8.4 x 10^{-2} – 8.8 x 10^{-2}	-0.10 – 0.11
Low quality, DEM, bounds in °C	-5.1 x 10^{-2} – 9.7 x 10^{-2}	-7.6 x 10^{-2} – 0.11	-1.8 x 10^{-2} – 0.19
Lowest quality, DEM, bounds in °C	-6.3 x 10^{-2} – 7.7 x 10^{-2}	-8.7 x 10^{-2} – 9.4 x 10^{-2}	-3.6 x 10^{-2} – 0.17

3.4.3 Colour calibration & DPC depth filtering

Combining the DPC depth filtering settings with the tie-point based colour calibration had a limited impact on temperature influences compared to the depth filtering settings without colour calibration (appendix O). Thus, the tie-point based colour calibration was not used in this assessment, and only the influence of the DEM based colour calibration was considered.

The combined influence of DPC depth filtering settings with the DEM based colour calibration on orthomosaic temperatures was larger than the influence of the depth filtering settings without colour calibration (Figure 14). Combining depth filtering settings with colour calibration increased the mean temperature influence with the average and mosaic blending modes (Table 7). With the disabled blending mode, the mean influence decreased at the aggressive and mild settings, whilst the mean value at the moderate setting remained similar to its non-colour calibrated counterpart (Figure 14 b, d). Adding colour calibration to the depth filtering settings increased the range between the lower and upper boxplot whiskers with the average and disabled blending modes. The variation decreased at the aggressive and moderate settings with the mosaic blending mode. Without colour calibration the whisker bounds represented at least 92%, 84%, and 95% of the influence values across all depth filtering settings with the average, disabled, and mosaic blending modes respectively. The percentages increased to 95%, 91%, and 94% when the depth filtering settings were combined with colour calibration.

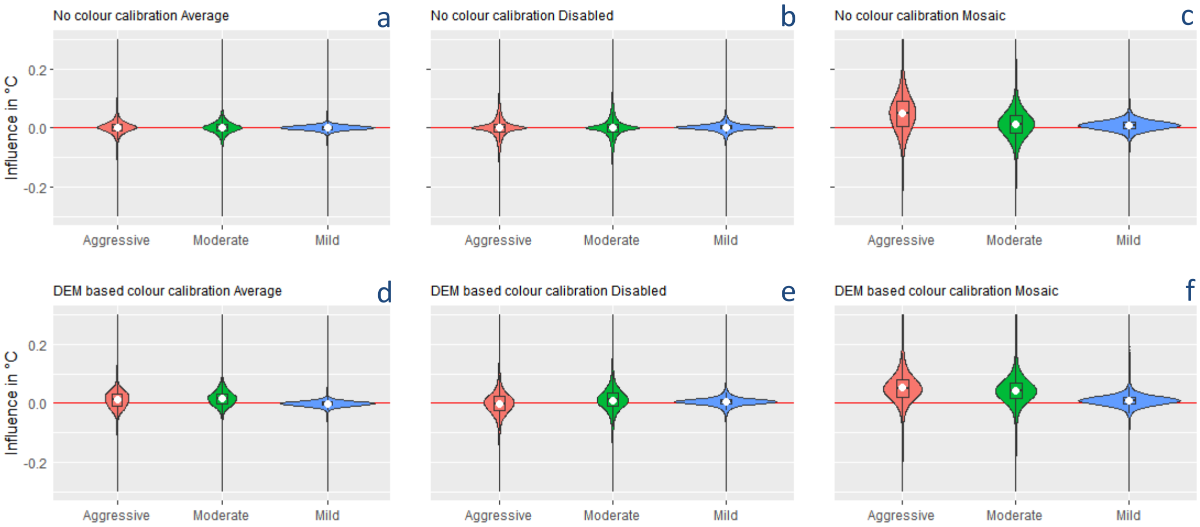

Figure 14 Violin plots of the combined influence of the DEM based colour calibration with DPC depth filtering settings on orthomosaic temperature values of all 36 plots combined. Plots a through c represent the influence of depth filtering settings without colour calibration with the average, disabled, and mosaic blending modes respectively. Plots d through f represent the influence of depth filtering settings combined with the DEM based colour calibration with the average, disabled, and mosaic blending modes respectively. The whiskers of the boxplots depict the 1.5 x IQR range. The white dots show the average values. This plot does not show the range of the outliers.

Table 7 Distribution metrics of the combined influence of DPC depth filtering and DEM based colour calibration with the mosaic blending mode, based on the aggregated values of all 36 grass plots. The mean and lower and upper boxplot whisker bounds are given for each combination between the colour calibration and DPC depth filtering settings.

DPC depth filtering setting, colour calibration, metric	**Average blending mode**	**Disabled blending mode**	**Mosaic blending mode**
Aggressive, No, mean in °C	-8.9 x 10^{-3}	2.1 x 10^{-2}	5.2 x 10^{-2}
Moderate, No, mean in °C	-1 x 10^{-2}	2.1 x 10^{-2}	1.7 x 10^{-2}
Mild, No, mean in °C	-1 x 10^{-2}	2.3 x 10^{-2}	1.4 x 10^{-2}
Aggressive, DEM, mean in °C	2.1 x 10^{-2}	8.9 x 10^{-3}	6 x 10^{-2}
Moderate, DEM, mean in °C	2.5 x 10^{-2}	2.1 x 10^{-2}	5 x 10^{-2}
Mild, DEM, mean in °C	8.1 x 10^{-3}	1.5 x 10^{-2}	1.9 x 10^{-2}
Aggressive, No, bounds in °C	-4.6 x 10^{-2} – 4.9 x 10^{-2}	-5.3 x 10^{-2} – 5.8 x 10^{-2}	-0.13 – 0.22
Moderate, No, bounds in °C	-4.8 x 10^{-2} – 4.8 x 10^{-2}	-5.5 x 10^{-2} – 5.8 x 10^{-2}	-0.12 – 0.14
Mild, No, bounds in °C	-2.2 x 10^{-2} – 2.3 x 10^{-2}	-2.3 x 10^{-2} – 2.9 x 10^{-2}	-3.6 x 10^{-2} – 5.5 x 10^{-2}
Aggressive, DEM, bounds in °C	-7.2 x 10^{-2} – 9.8 x 10^{-2}	-9.9 x 10^{-2} – 0.10	-7.2 x 10^{-2} – 0.17
Moderate, DEM, bounds in °C	-5.7 x 10^{-2} – 9.1 x 10^{-2}	-8.4 x 10^{-2} – 0.11	-7.2 x 10^{-2} – 0.16
Mild, DEM, bounds in °C	-2.6 x 10^{-2} – 2.4 x 10^{-2}	-2.5 x 10^{-2} – 3.7 x 10^{-2}	-3.7 x 10^{-2} – 5.6 x 10^{-2}

4 Discussion

The focus of this research was to assess the influence of five SfM processing parameters on orthomosaic temperatures. The data used for this assessment showed signs of thermal drift, which were alleviated most by a swath-based correction. The temperatures in the generated orthomosaics were most affected by the blending mode and colour calibration, especially by the mosaic blending mode and DEM based colour calibration. In this section, the results are compared to existing literature to explore their possible implications.

4.1 Orthomosaic quality

The thermal imagery had too little detail to perform a successful alignment without co-alignment. Metashape indicated that the alignment of all thermal images succeeded and the sparse point cloud covered the entire research area (Figure 4). However, the generated DPCs contained large holes.

Altering DPC settings did not remedy this problem, and changes to the alignment quality, tie-point limit, key-point limit and image selection settings did not remedy the alignment issues either. The orthomosaic temperatures based on thermal imagery that was aligned on its own would have been compared to orthomosaic temperatures of co-aligned thermal imagery. Due to the portrayed alignment issues, this comparison was not performed.

Similar problems were described by Dillen et al. (2016) and Hoffmann et al. (2016), who concluded that alignment issues occurred due to the relatively low resolution of thermal imagery combined with the limited contrast in said imagery. The alignment of thermal imagery could be improved by increasing the identifiable features. Maes et al. (2017) discussed how the alignment of thermal imagery can be slightly improved by correcting the thermal images based on fluctuations in air temperature. This correction likely evened out temperatures between overlapping images, and thus reduced differences between identifiable features. Turner et al. (2014) suggested a contrast stretch on digital numbers to increase the number of features SfM algorithms can detect. Ribeiro-Gomes et al. (2017) and Conte et al. (2018) similarly applied the Wallis filter to thermal images to increase contrast between features. Bitelli et al. (2015) successfully aligned thermal images without any contrast enhancements. They used thermal imagery from the urban environment, which contained enough detail for the SfM algorithm to find common objects between overlapping images. However, detail is often lacking in thermal imagery of agricultural fields and forests. It is in these types of applications that co-alignment with multispectral or RBG imagery is often considered (Kapil et al., 2023; Maes et al., 2017; Stutsel et al., 2021).

Before generating the co-aligned orthomosaics with different parameter combinations, a mask based vignetting correction was applied to the thermal imagery. This mask based approach removed most of the vignetting effect from the imagery. This approach limited the overlap between orthophotos as a consequence. In literature, other vignetting corrections are suggested that alter pixel values instead of removing them. For example, Aragon et al. (2020) suggest a radiometric calibration function based on the ambient temperature that reduces vignetting. Alternatively, W. Yuan & Hua, (2022) suggest creating a vignetting correction image to subtract from all in-flight images. These options retain all pixel values, yet require extensive testing of the thermal camera that is used. For this reason, only the central portion of the images were used, as suggested by Kelly et al. (2019), despite the inevitable impact on the orthomosaic generation.

4.2 Drift correction

Temperature anomalies were identified in the successfully aligned and orthomosaicked imagery. Temperatures fluctuated in the first few flightlines, and temperatures increased towards the eastern part of the research area. The discrepancy between orthomosaic and ground reference temperatures was smallest in the west of the orthomosaics, and largest in the east. A likely cause for these anomalies is the decrease in FPA temperature during the flight, which impacts the temperature measurements of the thermal camera (Figure 5). The FPA temperature is influenced by heat dissipated of internal electronic components of the camera, and by meteorological factors (Maes et al., 2017; Smigaj et al., 2017). Thermal cameras perform a non-uniformity correction (NUC) to alleviate temperature fluctuations measured by the microbolometers in the FPA. The NUC is based on the temperature of the camera shutter, under the assumption that its temperature is representative of the internal camera temperature. However, the temperature of camera parts may change at different rates, and the FPA temperature may change more rapidly than the NUC can correct for (Kelly et al., 2019; Wan et al., 2021; Z. Wang et al., 2023).

Three methods were applied to the thermal imagery in an attempt to correct for the observed temperature anomalies. The tie-point based correction had a limited impact on temperatures, and did not correct for the observed anomalies. Despite the visible temperature increase towards the east in the orthomosaics, the temperature at the location of tie-points mostly declined in later thermal images compared to the first image. The general temperature decline found in the calculated drift may correspond to the temperature decrease of the FPA. The correction was only performed with a linear equation, whereas Mesas-Carrascosa et al. (2018) performed the corrections using exponential, quadratic, bicubic, and quartic functions as well. Experimenting with these equations could have improved the performance of the correction. However, the impact would have been limited given the average drift of -9 x 10^{-3} °C/s. Despite the promising results achieved by Mesas-Carrascosa et al. (2018), this approach has not been widely used in literature. Döpper et al. (2020) used its general concept to determine the measurement noise of their camera, yet no additional literature was found to compare the drift correction performance to.

It is possible that the tie-point based correction was carried out erroneously. As Szostak et al. (2023) point out, the author of this correction did not provide an elaborate explanation of the calculations performed. Additionally, this author discussed the need for a drone attachment that precisely records the image acquisition time. The timestamp in image metadata is often captured with the precision of ±1 s, which can influence the calculated drift. The potential error would be greatest between adjacent images. For example, overlapping images could be acquired with a time difference of two seconds, with a temperature difference of 5 x 10^{-2} °C. Dividing the difference by two seconds results in a calculated drift of 2.5 x 10^{-2} °C, whereas the drift drops to 1.6 x 10^{-2} °C if the time difference was measured to be three seconds. The drone used in this study was not equipped with an attachment that precisely records image acquisition times on the 7th of Semptember 2023, which makes it a realistic source of error for this study.

The use of the accumulative drift correction rapidly increased the temperature in orthophotos in the flight direction. In the last flightlines that cover the grass field, temperatures were raised towards 50 °C (Figure 6). The strong temperature increase in the corrected orthomosaic indicates that of the adjacent images in each flightline, a higher temperature was measured in the first image than in the second image. The likely reason for the extreme result is that this correction is not suited for a large quantity of images. Z. Wang et al. (2023) discuss that with a large quantity of UAV data the uncertainty in the accumulative drift is inevitable. Irani Rahaghi et al. (2019) reported unsatisfactory results with a similar drift correction approach, where temperatures in overlapping image pairs were averaged. These authors used images with an overlap of 95%. Comparable to the findings of this report, the error accumulated and produced unsatisfactory results.

Irani Rahaghi et al. (2019) opted for a probability distribution based approach instead, where cross correlations were calculated between image pairs. The lag between the distributions was used to correct the second image based on the first. The corrected image was used to correct the third, and so forth. The authors showed that if the drift correction was not applied to the imagery, temperature drift caused temperature anomalies in the resultant orthomosaic. However, this probability distribution based approach was applied to images with a high overlap percentage. It is unknown how effective this drift correction is when there is less overlap between consecutive images in a dataset. Further research is required to determine the efficacy of the probability distribution based approach with lower image overlap percentages.

The swath-based approach reduced the temperature anomalies the most, leading to lower RMSE and MAE values, and an improved R^2. These results are similar to those of Malbéteau et al. (2021), where the swath-based approach improved the RMSE and MAE as well. The R^2 did not improve, as it was 0.99 with each of the blending modes. In contrast, the R^2 improved in this study compared to the blending modes of Metashape. Only one other study was found that used this alternative blending mode. Stutsel et al. (2021) applied this approach in their study regarding the detection of plant stress using thermal and optical imagery, however, the effectiveness of the swath-based approach was not discussed. Elfarkh et al. (2023) briefly discussed the swath-based approach, and mentioned that it corrects for wind effects that occur at the camera, and not the wind effects that influence the temperature on the ground. This limitation can lead to temperature inaccuracies being retained in thermal orthomosaics. Given the promising results achieved with the swath-based approach in this study, further developing the swath-based approach to consider ground based temperature fluctuations could lead to a thermal orthomosaicking approach with a higher accuracy.

4.3 Parameter influence

Apart from potential inaccuracies in captured thermal imagery, the SfM process used to generate orthomosaics forms another source of error. Several authors discuss how SfM is geared towards RGB and multispectral data and is unsuitable for thermal data (Conte et al., 2018; Elfarkh et al., 2023; Malbéteau et al., 2021). The most discussed parameter with regards to its impact on thermal imagery is the blending mode, given its direct impact on orthomosaic temperatures. This thesis expands on the prior research as the influence of the DPC quality, DPC depth filtering, colour calibration and blending modes on orthomosaic temperatures were assessed. The colour calibration and blending mode influenced orthomosaic temperatures most. The influence of the DPC quality and depth filtering setting was limited. However, combining either parameter with the mosaic blending mode strongly increased the influence on orthomosaic temperatures. Pairing the DPC parameters with colour calibration also caused a slight increase in influence with the DEM setting selected.

The blending mode had a large influence on orthomosaic temperatures (on average by 0.61 °C, with a maximum of 1.92 °C). In contrast to the results of Acorsi et al. (2020) and Malbéteau et al. (2021), the disabled setting produced the highest error in this study, although the R^2 was low with any of the blending modes. The performance of the average and mosaic blending modes was dissimilar across all studies. In the study by Acorsi et al. (2020) the R^2 and RMSE were 0.96 and 3.08 °C for the disabled blending mode, and 0.96 and 3.14 °C for the disabled and average blending modes. The disabled blending mode had an R^2 and RMSE of 0.99 and 1.63 °C in the study by Malbéteau et al. (2021). The mosaic blending mode performed similarly with a R^2 and RMSE of 0.99 and 1.63 °C, whereas the average blending mode produced a R^2 and RMSE of 0.99 and 1.66 °C. The performance difference of blending modes between studies is likely bound to the objects that were measured. The average blending mode combines temperatures taken from several geometry angles, whereas the disabled blending mode only retains temperatures at nadir (Perich et al., 2020). Consequently, the structures of the measured objects influence what temperatures are calculated in the average and mosaic blending modes.

Colour calibration had a large, but varied, impact on resultant temperatures depending on the used approach. The DEM based colour calibration resulted in larger variations in the temperature influence across the grass plots compared to the tie-point based colour calibration. The difference can be attributed to the difference in detail between the DEM and tie-points. Tie-points are sparsely distributed across the research area, whereas the used DEM has a high resolution and covers the entire research area. Consequently, there is a larger variation in height values in the DEM compared to the tie-points that the algorithm can utilize to estimate overlapping areas in imagery (Agisoft, 2023). No literature was found where colour calibration was applied to thermal imagery (Conte et al., 2018; Kelly et al., 2019; McCarthy et al., 2021, 2022; Ribeiro-Gomes et al., 2017). Applying colour calibration to thermal data could be beneficial. It reduced the RMSE and MAE in this study, as it partially alleviated the thermal anomalies in the resultant orthomosaics (appendix F). Tocci et al. (2022) discuss how colour calibration is often overlooked during the generation of RGB or multispectral orthomosaics, although it could correct for atmospheric changes that occurred during the flight. In most literature the focus was on assessing what parameters influence the reprojection error with RGB or multispectral imagery (Benjamin & Dennis O'brien, 2017; Śledź & Ewertowski, 2022; Tinkham & Swayze, 2021).

The influence of DPC quality settings on orthomosaic temperatures was limited. The DPC solely influences orthomosaic temperatures indirectly at the orthomosaicking step in the SfM workflow. The influence on orthomosaic temperatures was similar across the DPC quality settings with the average and disabled blending modes, likely due to the low height differences present in the research area (Figure 9, appendix M). Tinkham & Swayze (2021) demonstrated that the influence of the quality settings are more pronounced in a dataset with more height differences. With imagery of trees and understory, the height details of the understory were mostly lost if the low and lowest quality settings were used. Utilizing the medium to ultra-high settings retained most of these heights. Śledź & Ewertowski (2022) demonstrated that higher quality settings produced the least error compared to ground control points. Thus, it is possible that temperature differences between quality setting were caused by reprojection errors.

Orthomosaic temperatures were least impacted by the DPC depth filtering settings. The aggressive and moderate settings mostly performed similarly with the average and disabled blending modes, whereas the mild setting had the least impact on temperatures (Figure 10). Depth filtering had a small impact on the DPC, likely due to the lack of heights (Benjamin & Dennis O'brien, 2017). The influence of the depth filtering settings corresponds to the results of Tinkham & Swayze (2021), that showed that with distinct height differences the aggressive setting omits more DPC points than the moderate setting, whereas the mild setting affects the DPC the least. Thermal datasets acquired from areas with greater height differences would be affected more by the depth filtering settings, as the disparity between the influence of different settings would increase. Consequently, the selection of the depth filtering setting would likely have a greater impact on resultant orthomosaic temperatures.

4.4 Multi-parameter influence

The mosaic blending mode had a large impact on the influence of the DPC quality and depth filtering settings compared to the average and disabled blending modes (Figure 9, Figure 10). In contrast, the influence of the quality and depth filtering settings was near zero degrees Celsius with the average and disabled blending modes. The overall influence of the DPC quality and depth filtering settings was small, as these parameters only influence orthomosaic temperatures through the DEM in the orthorectification process (Agisoft, 2023; Perich et al., 2020). However, given the higher influence with the mosaic blending mode, it is likely that the DEM is used during the blending process as well. Despite the temperature increase caused by the DPC parameters with the mosaic blending mode, the produced orthomosaic temperatures were often lower than with the disabled blending mode and higher than with the average blending mode. These differences are likely caused by the blending algorithm of the mosaic blending mode. Overlapping pixel values are blended most along seamlines between images, whereas pixel values close to nadir are blended the least (Agisoft, 2023; Aragon et al., 2020; Malbéteau et al., 2021).

Combined with the mosaic blending mode, the medium DPC quality setting produced dissimilar results compared to the other quality settings. It constantly had a lower influence than the other quality settings. Given the indirect influence of the quality settings through the DEM, the orthomosaic was generated with the medium quality setting again, but paired with the DEM that was generated with the high quality setting. The resultant orthomosaic had a similar distribution of temperature values compared to the high, low, and lowest quality settings. Thus, the DEM generated with the medium quality setting was the cause of the lower influence. A potential reason for the difference in distribution caused by this DEM is the mosaic blending mode, given the aforementioned likelihood of the DEM being used in the blending process. This suspicion is strengthened by the fact that there was no disparity between the influence of the quality settings when combined with the average and disabled blending modes (appendix N). The reason why the resultant orthomosaic temperature distribution was different with the medium quality setting is unknown, as its DEM was similar to the DEMs of the high and low quality settings (appendix M).

The combined influence of the DPC quality and depth filtering settings on orthomosaic temperatures showed similar patterns across quality settings (Figure 12). Combinations with no or mild depth filtering had most influence on orthomosaic temperatures, whereas more aggressive depth filtering generally decreased the influence. This decrease is likely caused by the removal of height detail by the depth filtering settings. Young et al. (2022) and Tinkham & Swayze (2021) both applied several combinations of DPC quality and depth filtering settings on datasets with greater heights. In these studies, aggressive depth filtering settings removed details at the higher quality settings, whereas most height differences were removed at the lower quality settings. It is thus likely that the moderate and aggressive depth filtering settings removed what little height detail there was in the DPC of the grass field, which caused the decrease in temperature influence on the thermal orthomosaic. In contrast to the studies by Young et al. (2022) and Tinkham & Swayze (2021), the influence of the depth filtering settings was similar across the quality settings. This was likely caused by the lack of height differences in the grass field, as the quality settings all had a similar influence on orthomosaic temperatures when combined with the disabled depth filtering setting (Figure 9).

Combining DPC quality and depth filtering settings with the DEM based colour calibration increased the influence on orthomosaic temperatures across all blending modes (Figure 13, Figure 14). The difference was likely caused by the fact that the DPC quality and depth filtering settings were used in the DEM based colour calibration. In turn, the DEM based colour calibration was affected by the DPC parameters. In contrast, tie-points were generated before and independent of the DPC, meaning that the tie-point based colour calibration was not affected by DPC parameters. In contrast to the colour calibration tool in Metashape, colour calibration methods in literature do not use tie-points or the DEM (Abdalla et al., 2019; Huang et al., 2022; Tocci et al., 2022). The temperature influence these methods would have on orthomosaics would not be directly influenced by the DPC quality or depth filtering settings. However, the use of orthorectified imagery would introduce a limited influence of the DPC parameters, given the involvement of the DEM in the orthorectification process.

4.5 Limitations

The comparison of parameter influences was limited by the closed source nature of Agisoft Metashape. The Metashape manual provides a general explanation of most parameters, yet refrains from discussing the inner workings of the algorithms (Agisoft, 2023; Pell et al., 2022). This restricted the interpretability of the calculated parameter influences. Interpretations were based on the impact of parameters discussed in literature (often applied to RGB or multispectral data), combined with assumptions on how the perceived parameter impact influenced orthomosaic temperatures. An additional factor to consider is that Agisoft Metashape is one of several software packages that are used in orthomosaic creation, albeit one of the more popular packages (Ribeiro-Gomes et al., 2017). While all of them follow a similar SfM workflow, the findings of this thesis are not directly applicable to the other software packages.

The influence of SfM processing parameters on resultant orthomosaics is a scarcely discussed topic in literature, especially with regards to thermal imagery. However, research on the influence of processing parameters on RGB and multispectral imagery is scarce as well (Benjamin & Dennis O'brien, 2017; Śledź & Ewertowski, 2022). In select cases the influence of processing parameters was assessed in a part of the SfM workflow, such as the creation of DPCs (Tinkham & Swayze, 2021; Young et al., 2022). The literature scarcity limited the possibilities to compare the results of this study to findings in other studies.

In the process of generating orthomosaics based on co-aligned thermal imagery, the thermal imagery was involved in the generation of the DPC. At the ultra-high DPC quality setting, the involvement of the thermal imagery caused sporadic height differences of roughly 20 cm in the generated DEM (appendix M). At the lower quality setting these heights were not part of the DEMs. However, orthomosaics generated with the ultra-high quality setting were used as baselines for the calculation of parameter influences. Thus, the potential impact of the erroneous height differences were part of the calculations of single and multi-parameter temperature influences. It is advisable to disable the thermal imagery before the DPC generation in future studies.

The orthomosaics were radiometrically corrected with the empirical line correction. For this correction the temperatures of the reference panels situated to the south of the grass field were used. These panels were placed in close proximity to each other. Consequently, they were only captured in a few images during the flight. This is a limiting factor, as the extent of the corrected orthomosaics cover the entire grass field. The use of more reference panels spread across the research area would be beneficial as it could give an indication of how stable thermal measurements are during the flight. As the correction is linear in nature, the relative distribution of temperatures was not changed in the orthomosaics. The scale of the temperatures was changed. Thus, this correction did not influence the relative influence of processing parameters.

To calculate the influence of parameters through subtracting orthomosaics from each other, the orthomosaics had to be resampled. The orthomosaics that were processed in Metashape were exported in the resolution that was calculated by the program. As it is not possible to subtract pixels that are in different locations, lower resolution orthomosaics were resampled to match higher resolution orthomosaics. The default bilinear interpolation method of the R resample function was used. The possible impact of the resampling is small, given the high resolution of all orthomosaics, with pixel sizes ranging from 1.61 cm to 1.64 cm. An assessment of the impact of resampling on orthomosaic temperatures was outside of the scope of this project.

The influence of parameters was assessed for at the individual parameter level and for pairs of parameters. The parameter pairs always consisted of three parameters, as it is impossible to remove the impact of the blending mode parameter. Yet, this study did not explore the impact of all parameter settings simultaneously. Further research is required to gain insight into inter-parameter impact on orthomosaic temperatures.

5 Conclusion

The aim of this study was to determine what structure from motion (SfM) processing parameters are influential in thermal orthomosaicking, and to determine what influence parameters have on resultant orthomosaic temperatures. Parameters that directly perform calculations with the pixel values of thermal imagery (colour calibration and blending mode) were most influential. Other parameters, although used in the orthorectification process, had little influence on orthomosaic temperatures.

Thermal imagery failed to align without co-alignment to multispectral imagery. Thus, the temperature influence of this parameter could not be assessed. However, given the successful alignment of thermal imagery with co-alignment proved both the efficacy and importance of co-alignment, in the creation of thermal orthomosaics.

The blending mode and colour calibration had the most impact on the temperature influence of other parameters. However, the influence these parameters had varied between their respective settings.

The extent to which parameters influence resultant temperatures is likely influenced by the physical traits of the research area (height, structure, and diversity of land cover), and by measurement inaccuracies caused by fluctuations in the focal plane array temperature in the thermal camera. Datasets with little temperature variations across the images are likely to be the least influenced by parameter choices.

The outcomes of this study showed that it is important to be cautious in the parameter selection whilst creating thermal orthomosaics. The best performing set of parameters need to be selected on a case-by-case basis. For applications where a high accuracy is required, it is advised not to use thermal orthomosaics without validation with ground reference measurements.

6 Recommendations

Allowing the thermal camera to stabilize to the in-flight conditions before covering the research area could increase the accuracy of thermal imagery. The steep decrease in the FPA temperature was a likely cause for the temperature anomalies that were encountered (Figure 5). Adding additional flightlines before the drone passes the research area to the flight plan, would allow the camera to stabilize to the in-flight conditions. The FPA temperature stabilized towards the end of the 9 minute flight. Kelly et al. (2019) recommend to add 15 minutes of such stabilization time. The length of the stabilization time will depend on the operational capacity of the used drone and its batteries. An additional option would be to extend the flight with an additional overflight in the opposite direction. This additional data could pose as a reference for the initial overflight, in case anomalies are encountered in the resultant orthomosaics.

The dataset used in this study contained little height difference. Consequently, it is unknown how the processing parameters in Agisoft Metashape influence temperatures in datasets that capture more height variations. Tinkham & Swayze (2021) tested the influence of the DPC quality and depth filtering settings on imagery from trees and understory, and noted that the lower quality and aggressive depth filtering settings reduced the height detail perceived by the SfM algorithm. Consequently, there is a chance that in thermal datasets with more height variation, the DPC parameters have more influence on orthomosaic temperatures. Additionally, height differences and the structure of measured objects may influence the effect of the blending modes on orthomosaic temperatures. The disabled blending mode uses temperatures measured at nadir, whereas the average blending mode combines overlapping pixel values acquired at several angles. The influence of the blending modes on orthomosaic temperatures will thus likely differ based on the height and structure of the observed objects, yet the extent of this influence is unknown (Perich et al., 2020). Further research is required to assess the influence of heights on orthomosaic temperatures.

In future research the relevance of SfM parameters with regards to the output thermal orthomosaic could be assessed based on the PAWN global sensitivity analysis (GSA). Many GSA methods rank the relevance of parameters based on the resultant variance. An often used example of a variance based approach is the Sobol GSA (Zhang et al., 2024). However, the distribution of orthomosaic temperature values can be skewed or multimodal, as imagery could be captured from multiple land surface types with contrasting surface temperatures. In such cases, the use of variance based GSAs may produce discrepant results. In contrast, the PAWN GSA is density-based, utilizing a cumulative distribution function based approach. This allows this GSA to be used on skewed and multimodal distributed temperature outputs. An additional benefit of PAWN is that it allows one to focus on specific ranges of the output distributions, such as the tails. This could allow for a more in-depth analysis of what parameter combinations are influential in the generation of outliers (Pianosi & Wagener, 2015). However, the application of the PAWN GSA only indicates the relevance of SfM parameters to the resultant orthomosaic temperatures. It does not provide insight into which parts of the orthomosaics are most affected by certain parameters.

A greater understanding of the impact of input data on the influence SfM processing parameters have on orthomosaic temperatures could be achieved by investigating the spatial autocorrelation of resultant thermal orthomosaics with Moran's I. Kumari et al. (2019) applied Moran's I to Landsat 7 and Landsat 8 imagery to assess the dynamics between land cover changes to the land surface temperature as a result of the construction of thermal power plants. With this assessment the Moran's I calculated the spatial autocorrelation, and aided in identifying patterns in land surface temperatures caused by different land surface types. Similarly, the patterns in orthomosaics based on differing SfM parameter combinations could be identified. The physical traits of the captured images remain the same, yet the patterns that occur in the orthomosaics may differ based on the chosen parameters. By comparing the differences in temperature patterns between these orthomosaics, the cause of higher or lower temperature influences of parameters could be identified. For example, DPC depth filtering settings could impact temperature values more if there are great height differences within the research area. Comparing temperature patterns identified for at the disabled depth filtering setting to those of the aggressive setting could indicate in which parts of the research area depth filtering affects orthomosaic temperatures most. Consequently, the difference in patterns could be compared to physical traits of the research area to gain understanding of which of these traits the parameter is sensitive to.

Apart from Agisoft Metashape, several SfM based software packages are available. Both proprietary and open source. To fully understand the influence of SfM parameters in proprietary software packes on orthomosaic temperatures, extensive research would be required. Furthermore, the inner workings of the algorithms in proprietary software may change with an update, which could render prior findings incorrect. Open source SfM software packages could be used instead. Due to their open source nature the impact of the used algorithms to resultant temperatures can be researched directly. However, these software packages are found to be less user friendly and more prone to be affected by errors. Still, developing a SfM workflow based on such open source packages could provide more control and insight on resultant orthomosaic temperatures (Daniels et al., 2023; Eltner & Sofia, 2020).

An alternative option could be to develop a blending mode specifically geared towards thermal data. Malbéteau et al. (2021) suggested a swath-based approach, which corrects for temperature differences between flightlines. However, Elfarkh et al. (2023) argue that this approach corrects for temperature differences caused at the camera, not for temperature fluctuations that occur on the ground. Temperature fluctuations across images and ground surface temperatures are captured in the tie-point based approach by Mesas-Carrascosa et al. (2018). This approach captures temperature fluctuations that occur over time. A possible avenue for future research would be to investigate whether the concept of the tie-point based correction could be integrated into the swath-based approach. This way, temperature fluctuations that occur at the ground would be included in the blending mode as well.

7 References

Abdalla, A., Cen, H., Abdel-Rahman, E., Wan, L., & He, Y. (2019). Color calibration of proximal sensing RGB images of oilseed rape canopy via deep learning combined with k-means algorithm. *Remote Sensing*, *11*(24). https://doi.org/10.3390/RS11243001

Acorsi, M. G., Gimenez, L. M., & Martello, M. (2020). Assessing the Performance of a Low-Cost Thermal Camera in Proximal and Aerial Conditions. *Remote Sensing 2020, Vol. 12, Page 3591*, *12*(21), 3591. https://doi.org/10.3390/RS12213591

Agisoft. (2023). *Agisoft Metashape: User Manuals*. https://www.agisoft.com/downloads/user-manuals/

Aragon, B., Johansen, K., Parkes, S., Malbeteau, Y., Al-mashharawi, S., Al-amoudi, T., Andrade, C. F., Turner, D., Lucieer, A., & McCabe, M. F. (2020). A Calibration Procedure for Field and UAV-Based Uncooled Thermal Infrared Instruments. *Sensors (Basel, Switzerland)*, *20*(11), 1–24. https://doi.org/10.3390/S20113316

Belfiore, N., Vinti, R., Lovat, L., Chitarra, W., Tomasi, D., de Bei, R., Meggio, F., & Gaiotti, F. (2019). Infrared Thermography to Estimate Vine Water Status: Optimizing Canopy Measurements and Thermal Indices for the Varieties Merlot and Moscato in Northern Italy. *Agronomy 2019, Vol. 9, Page 821*, *9*(12), 821. https://doi.org/10.3390/AGRONOMY9120821

Benjamin, M. A., & Dennis O’brien, M. (2017). UNMANNED AERIAL SYSTEMS ASSESSMENT OF STRUCTURE FROM MOTION (SFM) PROCESSING PARAMETERS ON PROCESSING TIME, SPATIAL ACCURACY, AND GEOMETRIC QUALITY OF UNMANNED AERIAL SYSTEM DERIVED MAPPING PRODUCTS. *Journal of Unmanned Aerial Systems*, *3*(1). www.uasjournal.org

Bitelli, G., Conte, P., Csoknyai, T., Franci, F., Girelli, V. A., & Mandanici, E. (2015). Aerial thermography for energetic modelling of cities. *Remote Sensing*, *7*(2), 2152–2170. https://doi.org/10.3390/RS70202152

Borgonovo, E., & Plischke, E. (2016). Sensitivity analysis: A review of recent advances. *European Journal of Operational Research*, *248*(3), 869–887. https://doi.org/10.1016/J.EJOR.2015.06.032

Conte, P., Girelli, V. A., & Mandanici, E. (2018). Structure from Motion for aerial thermal imagery at city scale: Pre-processing, camera calibration, accuracy assessment. *ISPRS Journal of Photogrammetry and Remote Sensing*, *146*, 320–333. https://doi.org/10.1016/j.isprsjprs.2018.10.002

Daniels, L., Eeckhout, E., Wieme, J., Dejaegher, Y., Audenaert, K., & Maes, W. H. (2023). Identifying the Optimal Radiometric Calibration Method for UAV-Based Multispectral Imaging. *Remote Sensing*, *15*(11). https://doi.org/10.3390/RS15112909

Dillen, M., Vanhellemont, M., Verdonckt, P., Maes, W. H., Steppe, K., & Verheyen, K. (2016). Productivity, stand dynamics and the selection effect in a mixed willow clone short rotation coppice plantation. *Biomass and Bioenergy*, *87*, 46–54. https://doi.org/10.1016/J.BIOMBIOE.2016.02.013

Döpper, V., Gränzig, T., Kleinschmit, B., & Förster, M. (2020). Challenges in UAS-Based TIR Imagery Processing: Image Alignment and Uncertainty Quantification. *Remote Sensing 2020, Vol. 12, Page 1552*, *12*(10), 1552. https://doi.org/10.3390/RS12101552

Eide, A., Koparan, C., Zhang, Y., Ostlie, M., Howatt, K., & Sun, X. (2021). UAV-Assisted Thermal Infrared and Multispectral Imaging of Weed Canopies for Glyphosate Resistance Detection. *Remote Sensing 2021, Vol. 13, Page 4606*, *13*(22), 4606. https://doi.org/10.3390/RS13224606

Elfarkh, J., Johansen, K., Angulo, V., Camargo, O. L., & McCabe, M. F. (2023). Quantifying Within-Flight Variation in Land Surface Temperature from a UAV-Based Thermal Infrared Camera. *Drones 2023, Vol. 7, Page 617*, *7*(10), 617. https://doi.org/10.3390/DRONES7100617

Eltner, A., & Sofia, G. (2020). Structure from motion photogrammetric technique. *Developments in Earth Surface Processes*, *23*, 1–24. https://doi.org/10.1016/B978-0-444-64177-9.00001-1

Galieni, A., D'Ascenzo, N., Stagnari, F., Pagnani, G., Xie, Q., & Pisante, M. (2021). Past and Future of Plant Stress Detection: An Overview From Remote Sensing to Positron Emission Tomography. *Frontiers in Plant Science*, *11*, 609155. https://doi.org/10.3389/FPLS.2020.609155/BIBTEX

Garcia, M. V. Y., & Oliveira, H. C. (2020). THE INFLUENCE OF GROUND CONTROL POINTS CONFIGURATION AND CAMERA CALIBRATION FOR DTM AND ORTHOMOSAIC GENERATION USING IMAGERY OBTAINED FROM A LOW-COST UAV. *ISPRS Annals of the Photogrammetry, Remote Sensing and Spatial Information Sciences*, *V-1–2020*(1), 239–244. https://doi.org/10.5194/ISPRS-ANNALS-V-1-2020-239-2020

García-Tejero, I., Durán-Zuazo, V. H., Arriaga, J., Hernández, A., Vélez, L. M., & Muriel-Fernández, J. L. (2012). Approach to assess infrared thermal imaging of almond trees under water-stress conditions. *Fruits*, *67*(6), 463–474. https://doi.org/10.1051/FRUITS/2012040

Gutiérrez-Gordillo, S., García-Tejero, I. F., Durán Zuazo, V. H., Escalera, A. G., Gil, F. F., Amores-Agüera, J. J., Rodríguez, B. C., & Hernández-Santana, V. (2020). Assessing the Water-Stress Baselines by Thermal Imaging for Irrigation Management in Almond Plantations under Water Scarcity Conditions. *Water 2020, Vol. 12, Page 1298*, *12*(5), 1298. https://doi.org/10.3390/W12051298

Hasan, A., Widodo, Mutaqin, K. H., Taufik, M., & Hidayat, S. H. (2023). The Potential of a Low-Cost Thermal Camera for Early Detection of Temperature Changes in Virus-Infected Chili Plants. *Journal of ICT Research and Applications*, *17*(1), 17–28. https://doi.org/10.5614/ITBJ.ICT.RES.APPL.2023.17.1.2

Hoffmann, H., Nieto, H., Jensen, R., Guzinski, R., Zarco-Tejada, P., & Friborg, T. (2016). Estimating evaporation with thermal UAV data and two-source energy balance models. *Hydrol. Earth Syst. Sci*, *20*, 697–713. https://doi.org/10.5194/hess-20-697-2016

Huang, H., Tang, Y., Tan, Z., Zhuang, J., Hou, C., Chen, W., & Ren, J. (2022). Object-Based Attention Mechanism for Color Calibration of UAV Remote Sensing Images in Precision Agriculture. *IEEE Transactions on Geoscience and Remote Sensing*, *60*. https://doi.org/10.1109/TGRS.2022.3224580

Irani Rahaghi, A., Lemmin, U., Sage, D., & Barry, D. A. (2019). Achieving high-resolution thermal imagery in low-contrast lake surface waters by aerial remote sensing and image registration. *Remote Sensing of Environment*, *221*, 773–783. https://doi.org/10.1016/J.RSE.2018.12.018

Jain, K. (2021). How Photogrammetric Software Works: A Perspective Based on UAV's Exterior Orientation Parameters. *Journal of the Indian Society of Remote Sensing*, *49*(3), 641–649. https://doi.org/10.1007/S12524-020-01256-8/METRICS

Kapil, R., Castilla, G., Marvasti-Zadeh, S. M., Goodsman, D., Erbilgin, N., & Ray, N. (2023). Orthomosaicking Thermal Drone Images of Forests via Simultaneously Acquired RGB Images. *Remote Sensing 2023, Vol. 15, Page 2653*, *15*(10), 2653. https://doi.org/10.3390/RS15102653

Kelly, J., Kljun, N., Olsson, P. O., Mihai, L., Liljeblad, B., Weslien, P., Klemedtsson, L., & Eklundh, L. (2019). Challenges and Best Practices for Deriving Temperature Data from an Uncalibrated UAV Thermal Infrared Camera. *Remote Sensing 2019, Vol. 11, Page 567*, *11*(5), 567. https://doi.org/10.3390/RS11050567

Khanal, S., Fulton, J., & Shearer, S. (2017). An overview of current and potential applications of thermal remote sensing in precision agriculture. *Computers and Electronics in Agriculture*, *139*, 22–32. https://doi.org/10.1016/J.COMPAG.2017.05.001

KNMI - Dagwaarden neerslagstations. (n.d.). Retrieved March 6, 2024, from https://www.knmi.nl/nederland-nu/klimatologie/monv/reeksen

Kumari, M., Sarma, K., & Sharma, R. (2019). Using Moran's I and GIS to study the spatial pattern of land surface temperature in relation to land use/cover around a thermal power plant in Singrauli district, Madhya Pradesh, India. *Remote Sensing Applications: Society and Environment*, *15*, 100239. https://doi.org/10.1016/J.RSASE.2019.100239

Ludovisi, R., Tauro, F., Salvati, R., Khoury, S., Mugnozza, G. S., & Harfouche, A. (2017). Uav-based thermal imaging for high-throughput field phenotyping of black poplar response to drought. *Frontiers in Plant Science*, *8*, 252873. https://doi.org/10.3389/FPLS.2017.01681/BIBTEX

Maes, W. H., Huete, A. R., & Steppe, K. (2017). Optimizing the Processing of UAV-Based Thermal Imagery. *Remote Sensing 2017, Vol. 9, Page 476*, *9*(5), 476. https://doi.org/10.3390/RS9050476

Maes, W. H., & Steppe, K. (2019). Perspectives for Remote Sensing with Unmanned Aerial Vehicles in Precision Agriculture. *Trends in Plant Science*, *24*(2), 152–164. https://doi.org/10.1016/j.tplants.2018.11.007

Malbéteau, Y., Johansen, K., Aragon, B., Al-Mashhawari, S. K., & McCabe, M. F. (2021). Overcoming the Challenges of Thermal Infrared Orthomosaics Using a Swath-Based Approach to Correct for Dynamic Temperature and Wind Effects. *Remote Sensing 2021, Vol. 13, Page 3255*, *13*(16), 3255. https://doi.org/10.3390/RS13163255

McCarthy, E. D., Martin, J. M., Boer, M. M., & Welbergen, J. A. (2021). Drone-based thermal remote sensing provides an effective new tool for monitoring the abundance of roosting fruit bats. *Remote Sensing in Ecology and Conservation*, *7*(3), 461–474. https://doi.org/10.1002/RSE2.202

McCarthy, E. D., Martin, J. M., Boer, M. M., & Welbergen, J. A. (2022). Ground-based counting methods underestimate true numbers of a threatened colonial mammal: an evaluation using drone-based thermal surveys as a reference. *Wildlife Research*, *50*(6), 484–493. https://doi.org/10.1071/WR21120

Mesas-Carrascosa, F. J., Pérez-Porras, F., de Larriva, J. E. M., Frau, C. M., Agüera-Vega, F., Carvajal-Ramírez, F., Martínez-Carricondo, P., & García-Ferrer, A. (2018). Drift Correction of Lightweight Microbolometer Thermal Sensors On-Board Unmanned Aerial Vehicles. *Remote Sensing 2018, Vol. 10, Page 615*, *10*(4), 615. https://doi.org/10.3390/RS10040615

Mulero, G., Jiang, D., Bonfil, D. J., & Helman, D. (2023). Use of thermal imaging and the photochemical reflectance index (PRI) to detect wheat response to elevated CO2 and drought. *Plant, Cell & Environment*, *46*(1), 76–92. https://doi.org/10.1111/PCE.14472

Ozturk, M., Turkyilmaz Unal, B., García-Caparrós, P., Khursheed, A., Gul, A., & Hasanuzzaman, M. (2021). Osmoregulation and its actions during the drought stress in plants. *Physiologia Plantarum*, *172*(2), 1321–1335. https://doi.org/10.1111/PPL.13297

Pell, T., Li, J. Y. Q., & Joyce, K. E. (2022). Demystifying the Differences between Structure-from-Motion Software Packages for Pre-Processing Drone Data. *Drones*, *6*(1). https://doi.org/10.3390/DRONES6010024

Perich, G., Hund, A., Anderegg, J., Roth, L., Boer, M. P., Walter, A., Liebisch, F., & Aasen, H. (2020). Assessment of Multi-Image Unmanned Aerial Vehicle Based High-Throughput Field Phenotyping of Canopy Temperature. *Frontiers in Plant Science*, *11*, 482307. https://doi.org/10.3389/FPLS.2020.00150/BIBTEX

Pianosi, F., & Wagener, T. (2015). A simple and efficient method for global sensitivity analysis based on cumulative distribution functions. *Environmental Modelling & Software*, *67*, 1–11. https://doi.org/10.1016/J.ENVSOFT.2015.01.004

Pineda, M., Barón, M., & Pérez-Bueno, M. L. (2020). Thermal Imaging for Plant Stress Detection and Phenotyping. *Remote Sensing 2021, Vol. 13, Page 68*, *13*(1), 68. https://doi.org/10.3390/RS13010068

Qin, W., Wang, J., Ma, L., Wang, F., Hu, N., Yang, X., Xiao, Y., Zhang, Y., Sun, Z., Wang, Z., & Yu, K. (2022). UAV-Based Multi-Temporal Thermal Imaging to Evaluate Wheat Drought Resistance in Different Deficit Irrigation Regimes. *Remote Sensing*, *14*(21), 5608. https://doi.org/10.3390/RS14215608/S1

Rama, H.-O., Roberts, D., Tignor, M., Poloczanska, E. S., Mintenbeck, K., Alegría, A., Craig, M., Langsdorf S., Löschke, S., Möller, V., Okem, A., Rama, B., & Ayanlade, S. (2022). *Climate Change 2022: Impacts, Adaptation and Vulnerability Working Group II Contribution to the Sixth Assessment Report of the Intergovernmental Panel on Climate Change*. https://doi.org/10.1017/9781009325844.

Ribeiro-Gomes, K., Hernández-López, D., Ortega, J. F., Ballesteros, R., Poblete, T., & Moreno, M. A. (2017). Uncooled Thermal Camera Calibration and Optimization of the Photogrammetry Process for UAV Applications in Agriculture. *Sensors 2017, Vol. 17, Page 2173*, *17*(10), 2173. https://doi.org/10.3390/S17102173

Sepulcre-Cantó, G., Zarco-Tejada, P. J., Jiménez-Muñoz, J. C., Sobrino, J. A., Miguel, E. De, & Villalobos, F. J. (2006). Detection of water stress in an olive orchard with thermal remote sensing imagery. *Agricultural and Forest Meteorology*, *136*(1–2), 31–44. https://doi.org/10.1016/J.AGRFORMET.2006.01.008

Śledź, S., & Ewertowski, M. W. (2022). Evaluation of the Influence of Processing Parameters in Structure-from-Motion Software on the Quality of Digital Elevation Models and Orthomosaics in the Context of Studies on Earth Surface Dynamics. *Remote Sensing*, *14*(6), 1312. https://doi.org/10.3390/RS14061312/S1

Smigaj, M., Gaulton, R., Suarez, J. C., & Barr, S. L. (2017). Use of Miniature Thermal Cameras for Detection of Physiological Stress in Conifers. *Remote Sensing 2017, Vol. 9, Page 957*, *9*(9), 957. https://doi.org/10.3390/RS9090957

Stutsel, B., Johansen, K., Malbéteau, Y. M., & McCabe, M. F. (2021). Detecting Plant Stress Using Thermal and Optical Imagery From an Unoccupied Aerial Vehicle. *Frontiers in Plant Science*, *12*, 734944. https://doi.org/10.3389/FPLS.2021.734944/BIBTEX

Szostak, R., Zimnoch, M., Wachniew, P., & Jasek-Kamińska, A. (2023). Self-Calibration of UAV Thermal Imagery Using Gradient Descent Algorithm. *Drones*, *7*(11). https://doi.org/10.3390/DRONES7110683

Tinkham, W. T., & Swayze, N. C. (2021). Influence of Agisoft Metashape Parameters on UAS Structure from Motion Individual Tree Detection from Canopy Height Models. *Forests 2021, Vol. 12, Page 250*, *12*(2), 250. https://doi.org/10.3390/F12020250

Tocci, F., Figorilli, S., Vasta, S., Violino, S., Pallottino, F., Ortenzi, L., & Costa, C. (2022). Advantages in Using Colour Calibration for Orthophoto Reconstruction. *Sensors*, *22*(17). https://doi.org/10.3390/S22176490

Turner, D., Lucieer, A., Malenovský, Z., King, D. H., & Robinson, S. A. (2014). Spatial Co-Registration of Ultra-High Resolution Visible, Multispectral and Thermal Images Acquired with a Micro-UAV over Antarctic Moss Beds. *Remote Sensing 2014, Vol. 6, Pages 4003-4024*, *6*(5), 4003–4024. https://doi.org/10.3390/RS6054003

Virtue, J., Turner, D., Williams, G., Zeliadt, S., McCabe, M., & Lucieer, A. (2021). Thermal Sensor Calibration for Unmanned Aerial Systems Using an External Heated Shutter. *Drones 2021, Vol. 5, Page 119*, *5*(4), 119. https://doi.org/10.3390/DRONES5040119

Wan, Q., Brede, B., Smigaj, M., & Kooistra, L. (2021). Factors influencing temperature measurements from miniaturized thermal infrared (Tir) cameras: A laboratory-based approach. *Sensors*, *21*(24), 8466. https://doi.org/10.3390/S21248466/S1

Wang, L., Poque, S., & Valkonen, J. P. T. (2019). Phenotyping viral infection in sweetpotato using a high-throughput chlorophyll fluorescence and thermal imaging platform. *Plant Methods*, *15*(1), 1–14. https://doi.org/10.1186/S13007-019-0501-1/FIGURES/5

Wang, Z., Zhou, J., Ma, J., Wang, Y., Liu, S., Ding, L., Tang, W., Pakezhamu, N., & Meng, L. (2023). Removing temperature drift and temporal variation in thermal infrared images of a UAV uncooled thermal infrared imager. *ISPRS Journal of Photogrammetry and Remote Sensing*, *203*, 392–411. https://doi.org/10.1016/j.isprsjprs.2023.08.011

Yang, X., Lu, M., Wang, Y., Wang, Y., Liu, Z., & Chen, S. (2021). Response Mechanism of Plants to Drought Stress. *Horticulturae 2021, Vol. 7, Page 50*, *7*(3), 50. https://doi.org/10.3390/HORTICULTURAE7030050

Young, D. J. N., Koontz, M. J., Weeks, | Jonahmaria, Alberto, C., & Silva, A. (2022). Optimizing aerial imagery collection and processing parameters for drone-based individual tree mapping in structurally complex conifer forests. *Methods Ecol Evol*, *13*, 1447–1463. https://doi.org/10.1111/2041-210X.13860

Yuan, G., Wang, Y., Zhao, F., Wang, T., Zhang, L., Hao, M., Yan, S., Dang, L., & Peng, B. (2021). Accuracy assessment and scale effect investigation of UAV thermography for underground coal fire surface temperature monitoring. *International Journal of Applied Earth Observation and Geoinformation*, *102*, 102426. https://doi.org/10.1016/J.JAG.2021.102426

Yuan, W., & Hua, W. (2022). A Case Study of Vignetting Nonuniformity in UAV-Based Uncooled Thermal Cameras. *Drones 2022, Vol. 6, Page 394*, *6*(12), 394. https://doi.org/10.3390/DRONES6120394

Zhang, M., Liu, C., Hu, R., Han, H., & Wu, Q. (2024). Comparing global sensitivity analysis methods for the joint thermal design parameters of a space manipulator based on the Sobol' and PAWN. *Thermal Science and Engineering Progress*, *47*, 102338. https://doi.org/10.1016/J.TSEP.2023.102338

8 Appendix

A. Table of content for zip file

Table of Content of the zip file that accompanies the thesis report.

- Documentation of what is where in the zip-file (README file)
- Report (Word, PDF)
- Midterm & Final presentation (PPTX)
- Agisoft projects
  - Project where thermal imagery was co-aligned with multispectral imagery
  - Project where thermal imagery was not co-aligned with multispectral imagery
- Datasets used and created
  - Raw thermal and multispectral imagery
  - Orthomosaics cropped to the size of the 36 grass plots
  - Influence rasters of the colour calibration settings of the 36 grass plots
  - Excel files with the statistics mentioned in the (multi)parameter influence results
  - The mask that was applied during the orthomosaicking process
- Scripts
  - R scripts:
    - Empirical line correction
    - Accuracy assessment
    - Drift corrections
    - Code for cropping the orthomosaics to the size of the 36 grass plots
    - Code for calculating colour calibration influence rasters
    - Code for calculating the influence of the blending mode
    - Code for calculating the influence of DPC quality
    - Code for calculating the influence of DPC depth filtering
    - Code for calculating the influence of colour calibration
    - Code for calculating combined influence DPC quality and depth filtering
    - Code for calculating combined influence DPC quality and colour calibration
    - Code for calculating combined influence DPC depth filtering and colour calibration
- Figures shown in the report
- Excel files
  - All excel files that were generated in the R scripts mentioned above.
    - Statistics of aggregated plots, representing the influence of parameters on orthomosaic temperatures across all 36 grass plots
    - Statistics extracted during the tie-point based drift correction

- PDF files of used literature

B. Layout Nergena grass plot experiment

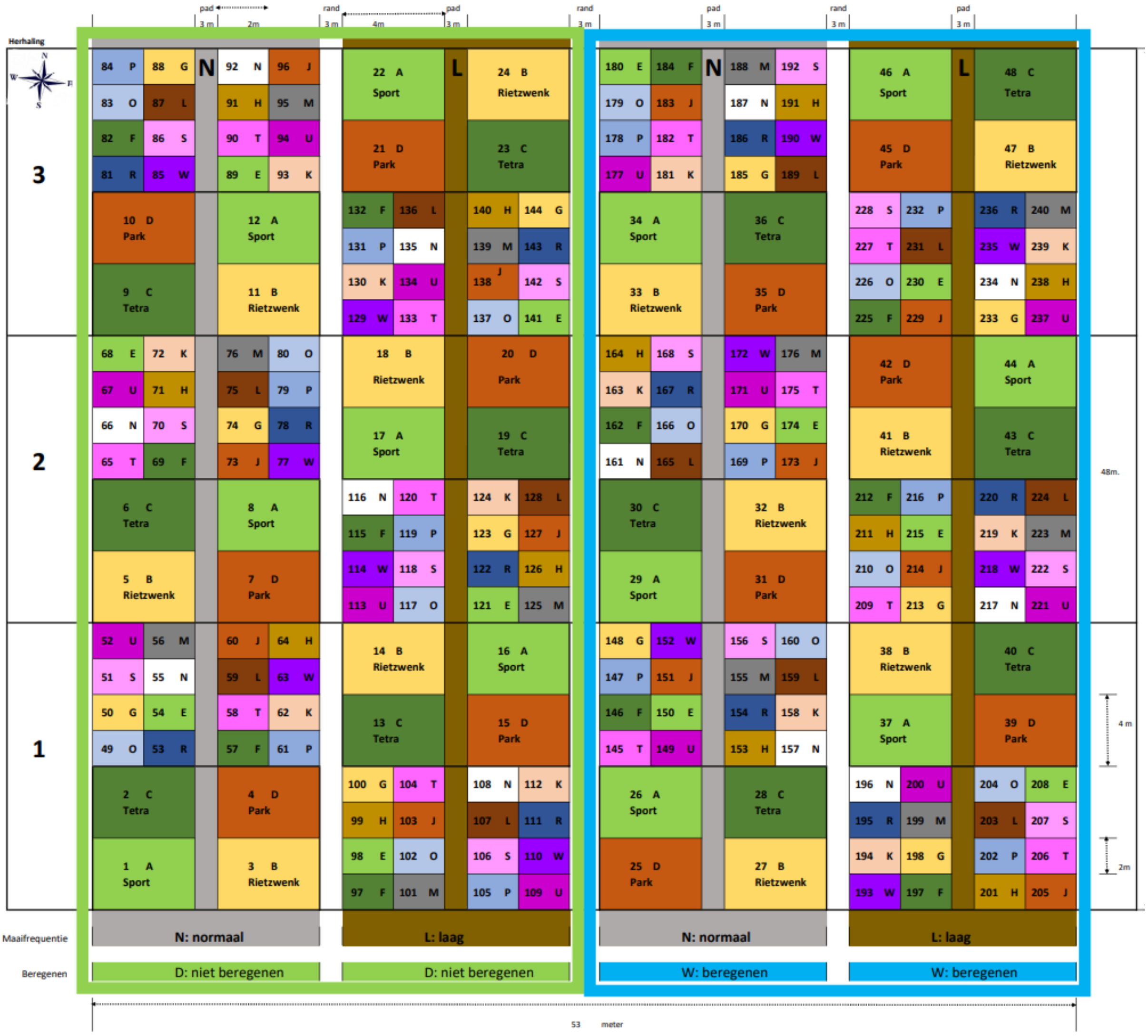

Figure 15 Overview of the layout of the Nergena grass field. Each colour represents a different grass species / mixture. The grass field is divided into four parts. At the bottom of each of the four grass strips either 'normaal', 'laag', 'niet beregenen', and 'beregenen' is written. The words 'normaal' and 'laag' refer to the mowing heights of 6 cm and 3 chm. 'Niet beregenen' and 'beregenen' refers to the irrigation scheme, where the strips linked with 'niet beregenen' are not irrigated, and the plots linked to 'beregenen' are irrigated.

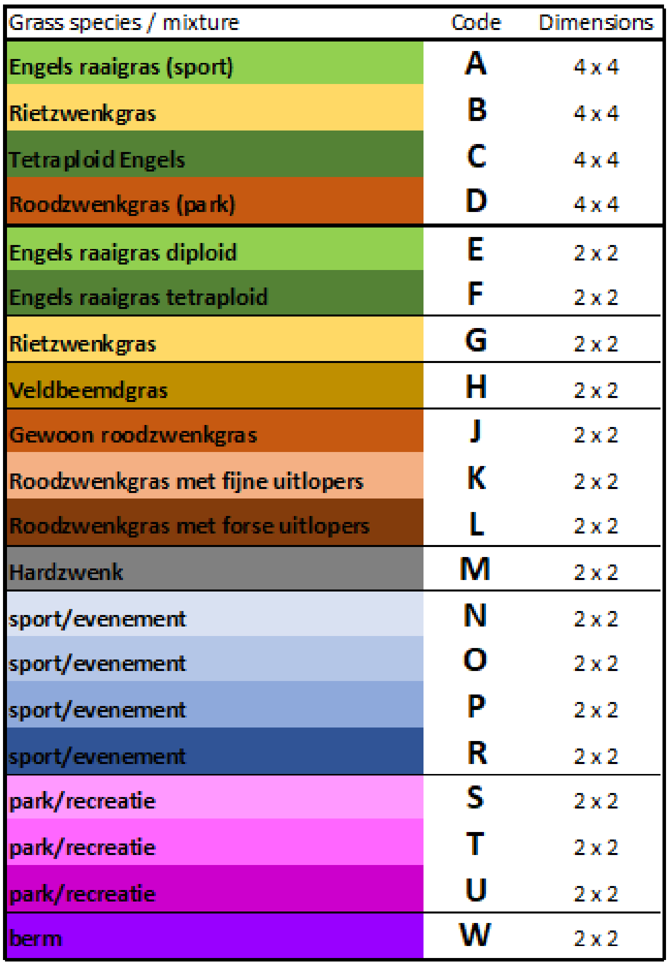

Grass species / mixture	Code	Dimensions
Engels raaigras (sport)	A	4 x 4
Rietzwenkgras	B	4 x 4
Tetraploid Engels	C	4 x 4
Roodzwenkgras (park)	D	4 x 4
Engels raaigras diploid	E	2 x 2
Engels raaigras tetraploid	F	2 x 2
Rietzwenkgras	G	2 x 2
Veldbeemdgras	H	2 x 2
Gewoon roodzwenkgras	J	2 x 2
Roodzwenkgras met fijne uitlopers	K	2 x 2
Roodzwenkgras met forse uitlopers	L	2 x 2
Hardzwenk	M	2 x 2
sport/evenement	N	2 x 2
sport/evenement	O	2 x 2
sport/evenement	P	2 x 2
sport/evenement	R	2 x 2
park/recreatie	S	2 x 2
park/recreatie	T	2 x 2
park/recreatie	U	2 x 2
berm	W	2 x 2

Figure 16 Legend of the grass species and dimensions in the layout of the Nergena grass field

C. Ground reference measurement locations

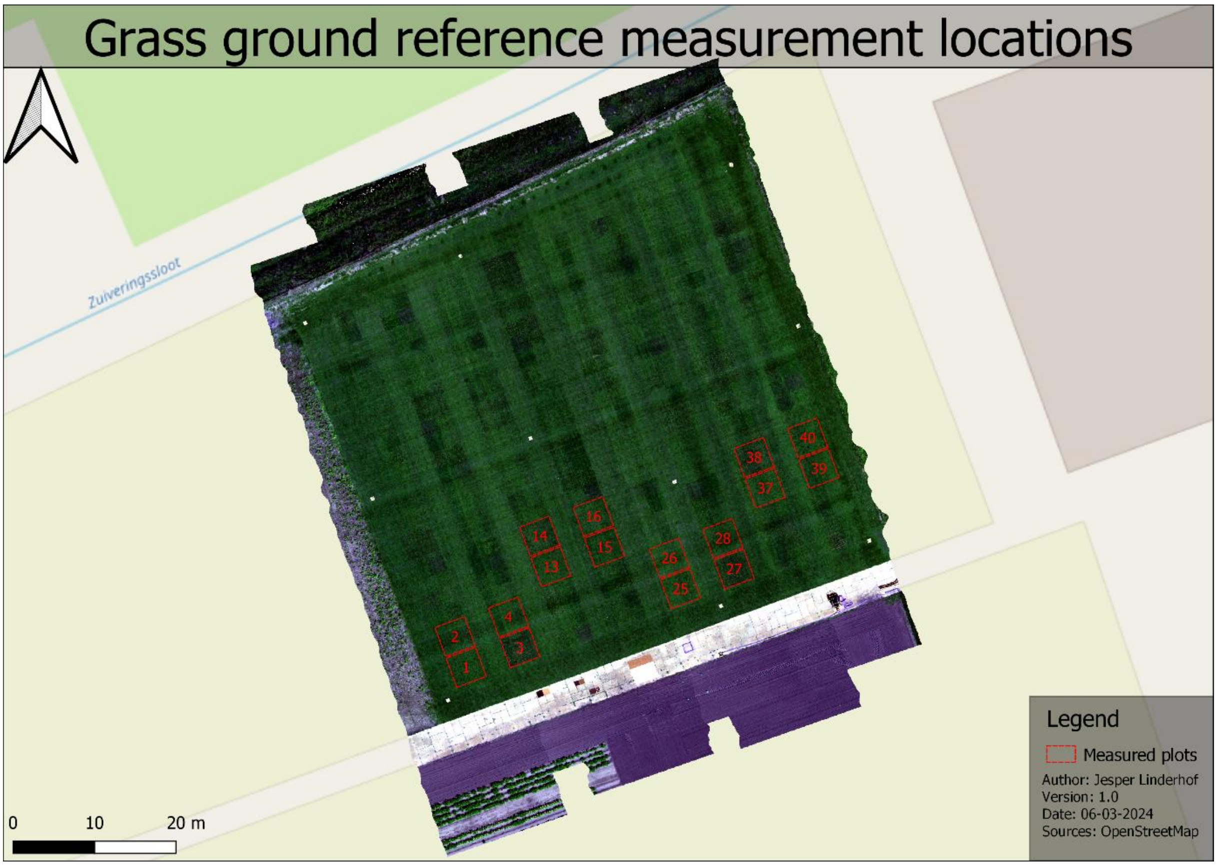

Figure 17 Overview of the grass plots that were measured with the Raytek handheld device. The measurements were performed in the middle of each of these grass plots, at a height of approximately 1 meter.

D. Vignetting correction

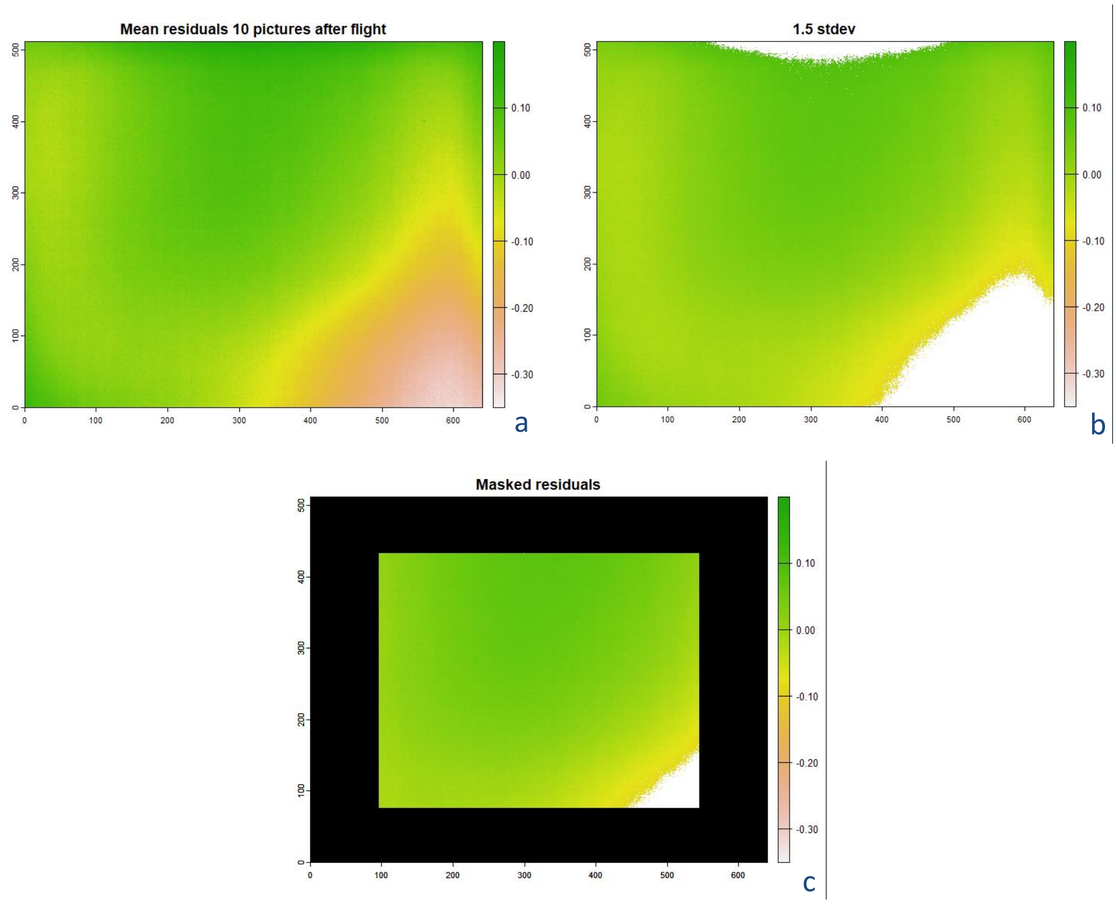

Figure 18 A: Mean residuals illustrating the vignetting effect. B: The vignetting effect after removing outliers (1.5 standard deviation). C: The mask applied to remove the vignetting effect.

E. Fixed parameter settings Agisoft Metashape

Table 8 Overview of the fixed parameter settings used during the orthomosaicking process in Agisoft Metashape. For each parameter the used setting, the potential influence on the thermal orthomosaic and the source used to assess the potential influence of the parameter settings are shown.

Parameters	Setting or value(s)	Influence	Influence source
Align photos			
Accuracy	Highest	Thermal data contains little detail, so even a small loss of detail will reduce the accuracy of the SfM process.	(Agisoft, 2023)
Preselection type	Generic + reference (Source)	Including generic and reference preselection types reduces the number of tie point mismatches.	(Döpper et al., 2020)
Key and tie point limit	20.000 and 1.000	The key and tie point limit has a small impact on the orthomosaic accuracy.	(Śledź & Ewertowski, 2022), (Maes et al., 2017), (Acorsi et al., 2020)
Ground control points	-	The addition of ground control points improves the alignment of the cameras.	(Jain, 2021), (Garcia & Oliveira, 2020)
Build dense point cloud			
Source data	Dense point cloud		(Agisoft, 2023)
Calculate point confidence	Enabled	This only calculates point confidence, it does not impact the SfM calculations.	(Agisoft, 2023)
Build digital elevation model			
Projection type	Geographic	This only determines the projection type, it does not impact the SfM calculations.	(Agisoft, 2023)
Source data	Depth maps	Other source data types can be selected which can lower the quality of the DEM. However,	(Agisoft, 2023)

		as the research area does not have any height differences, the impact would be small.	
Interpolation	Enabled mode	Thermal data is prone to failed alignments, which can cause gaps. For this reason, the enabled mode was selected.	(Kapil et al., 2023), (Maes et al., 2017)
Setup boundaries	Default	This parameter has no influence on the SfM calulcations.	(Agisoft, 2023)
Resolution	Default	This parameter has no influence on the SfM calulcations.	(Agisoft, 2023)
Total size (pix)	Default	This parameter has no influence on the SfM calulcations.	(Agisoft, 2023)
Build orthomosaic			
Projection type	Geographic	This only determines the projection type, it does not impact the SfM calculations.	(Agisoft, 2023)
Surface	DEM	Given the lack of height differences in the research area, the use of a DEM compared to a mesh would yield little difference.	(Agisoft, 2023)
Pixel size	Default	This parameter has no influence on the SfM calulcations.	(Agisoft, 2023)
Max. dimension (pix)	Default	This parameter has no influence on the SfM calulcations.	(Agisoft, 2023)
Enable hole filling	Enabled	This setting prevents the salt-and-pepper effect caused by complex surfaces. As the surface of the research area is flat, the influence of this parameter is estimated to be low.	(Agisoft, 2023)

F. RMSE and MAE orthomosaics compared to ground reference measurements

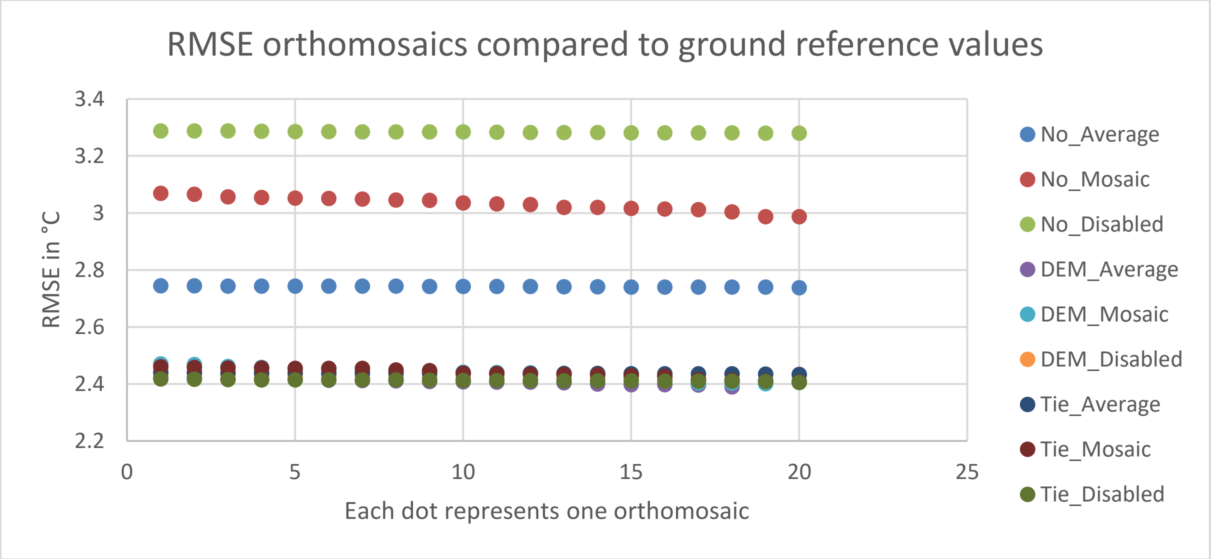

Figure 19 RMSE values between orthomosaic temperatures and ground reference measurements. The legend entries depict the colour calibration (No, DEM based or tie-point based colour calibration) and blending modes (Average, Mosaic, Disabled) that were applied. A total of 20 orthomosaics were created with each combination of colour calibration and blending mode. Each dot on the graph, and thus the increment on the x-axis, represents one orthomosaic.

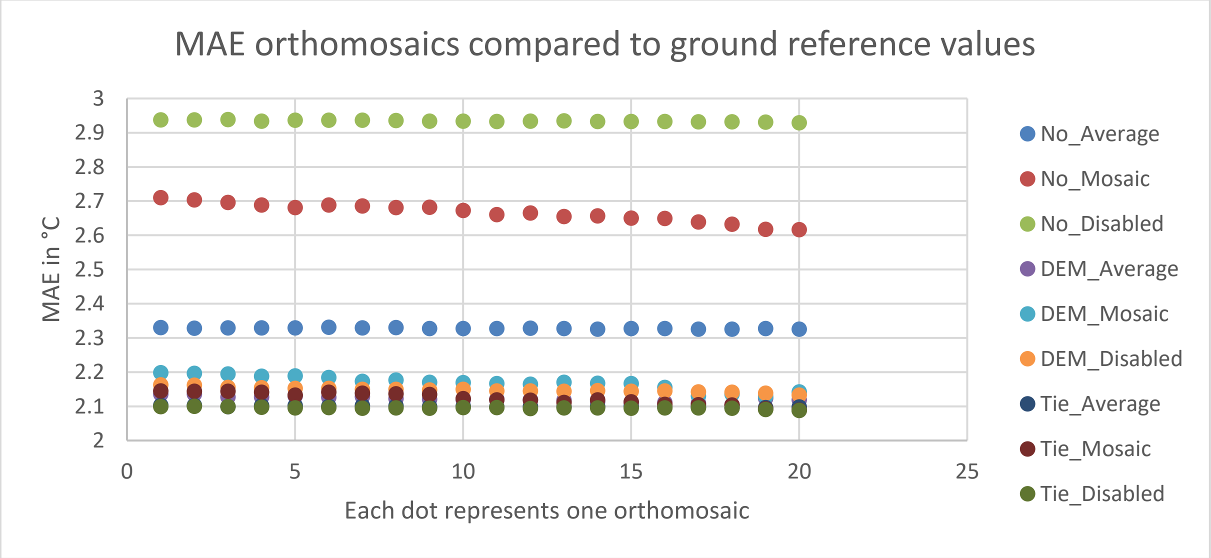

Figure 20 MAE values between orthomosaic temperatures and ground reference measurements. The legend entries depict the colour calibration (No, DEM based or tie-point based colour calibration) and blending modes (Average, Mosaic, Disabled) that were applied. A total of 20 orthomosaics were created with each combination of colour calibration and blending mode. Each dot on the graph, and increment on the x-axis, represents one orthomosaic.

G. Ground reference measurements

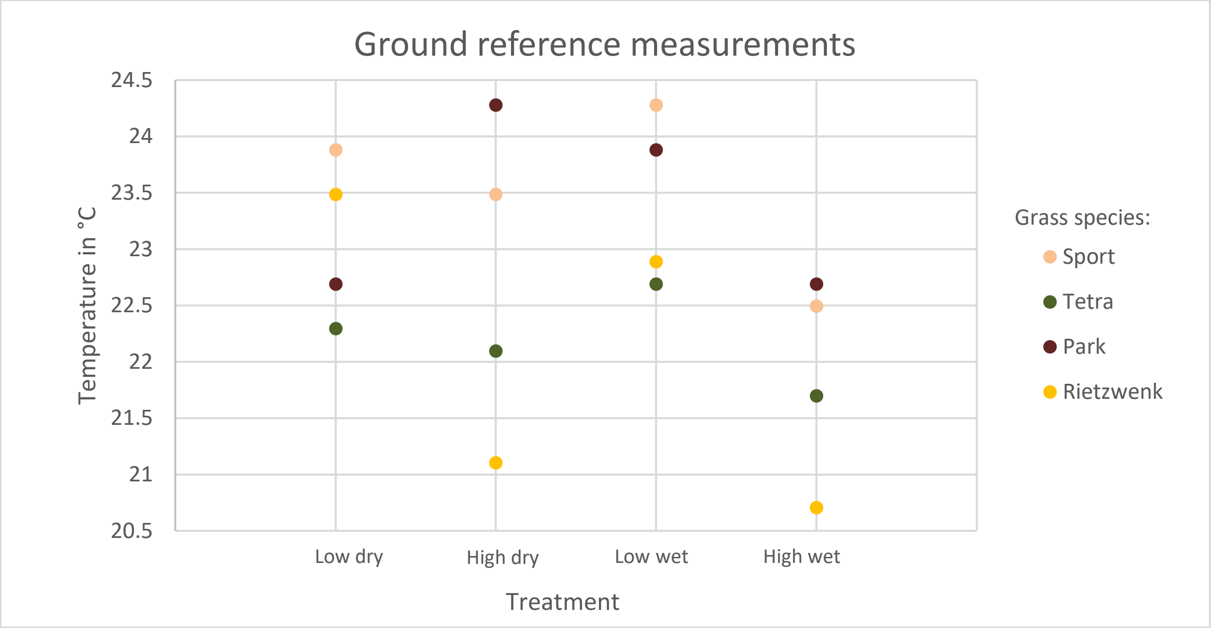

Figure 21 Ground reference measurements in °C per grass species, per treatment. The treatment is shown on the x-axis. The indicators 'Low' and 'High' represent the mowing heights of the grass field of 3 cm and 6 cm respectively. The indicators 'Dry' and 'Wet' refer to the non-irrigated and irrigated parts of the grass field.

H. Difference orthomosaic and ground reference temperatures

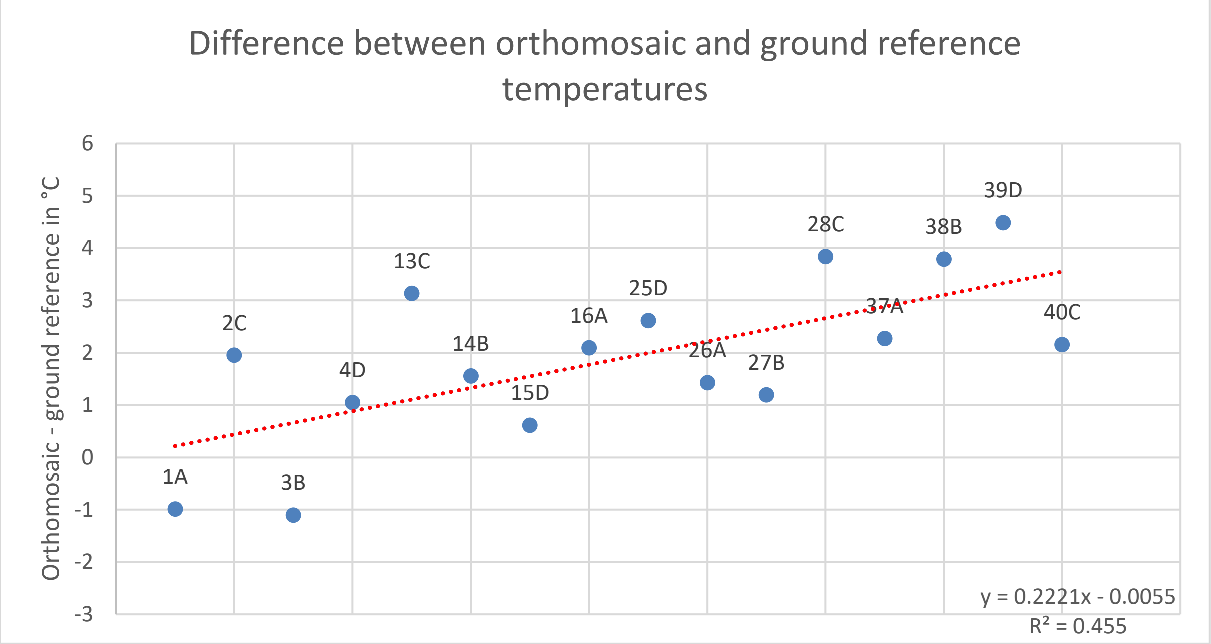

Figure 22 Difference between orthomosaic temperatures and ground reference measurements. The orthomosaic used in this graph was generated with the ultra-high DPC quality setting, the aggressive DPC depth filtering setting, DEM based colour calibration, and the disabled blending mode. Each dot represents a grass plot that was measured. The grass plot number is plotted next to each dot. Lower grass plot numbers represent grass plots to the western side of the grass field, higher grass plot numbers represent grass plots to the eastern side of the grass field.

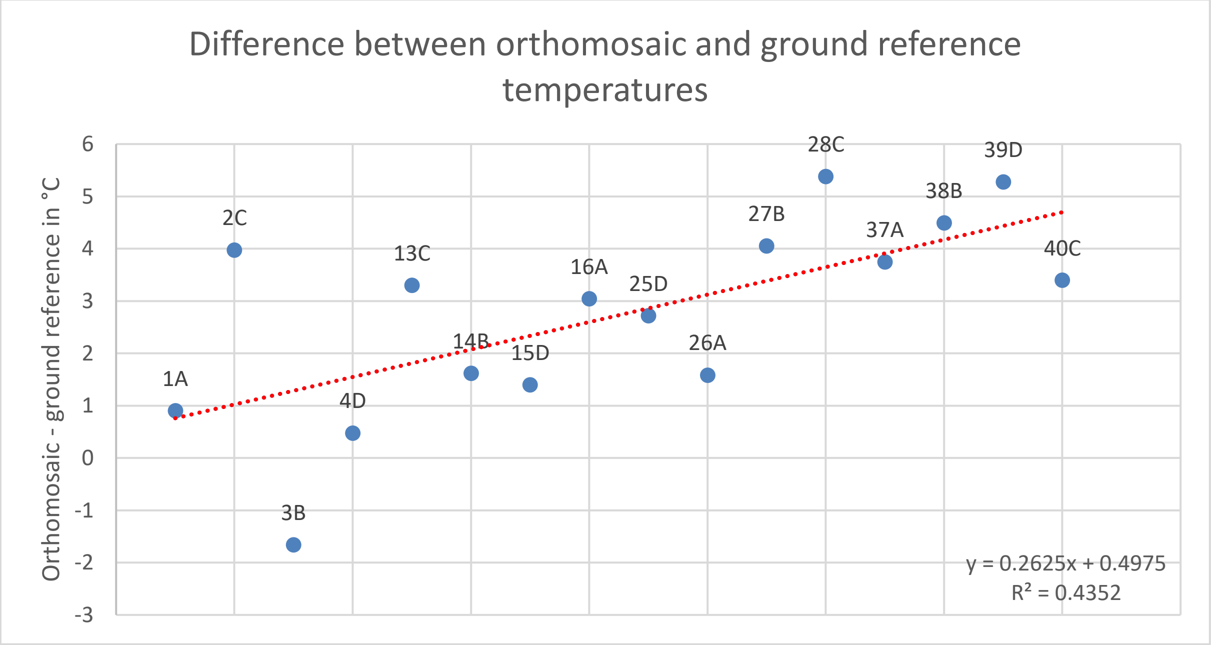

Figure 23 Difference between orthomosaic temperatures and ground reference measurements. The orthomosaic used in this graph was generated with the ultra-high DPC quality setting, the aggressive DPC depth filtering setting, no colour calibration, and the disabled blending mode. Each dot represents a grass plot that was measured. The grass plot number is plotted next to each dot. Lower grass plot numbers represent grass plots to the western side of the grass field, higher grass plot numbers represent grass plots to the eastern side of the grass field.

I. Point cloud tie-point based drift correction point cloud

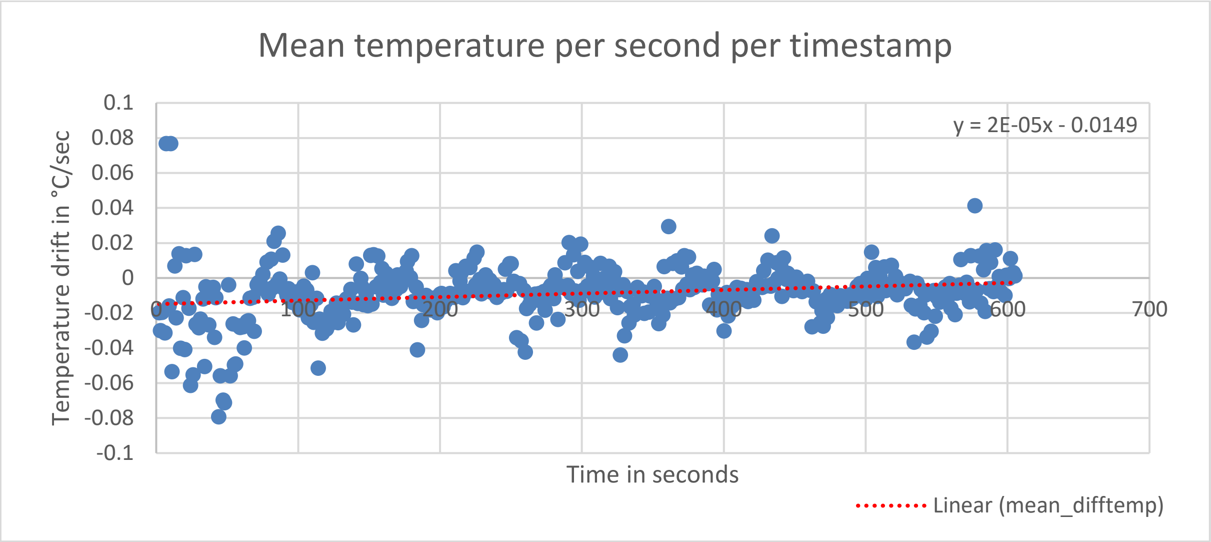

Graph 2 Sub-product of the tie-point based drift correction. Temperatures were extracted from orthophotos at the locations of each shared tie point. The temperature extracted from the first image (first time the temperature was measured at a tie-point) served as a baseline, and was subtracted from the temperatures at the same tie-point location extracted from later images. The resultant difference was divided by the time that passed between the first and the n-th image. Consequently, a large number of temperature differences (drift) were calculated for each timestamp. All these values were averaged for each timestamp. The resultant values are shown in this graph.

J. DPC quality influence per grass plot

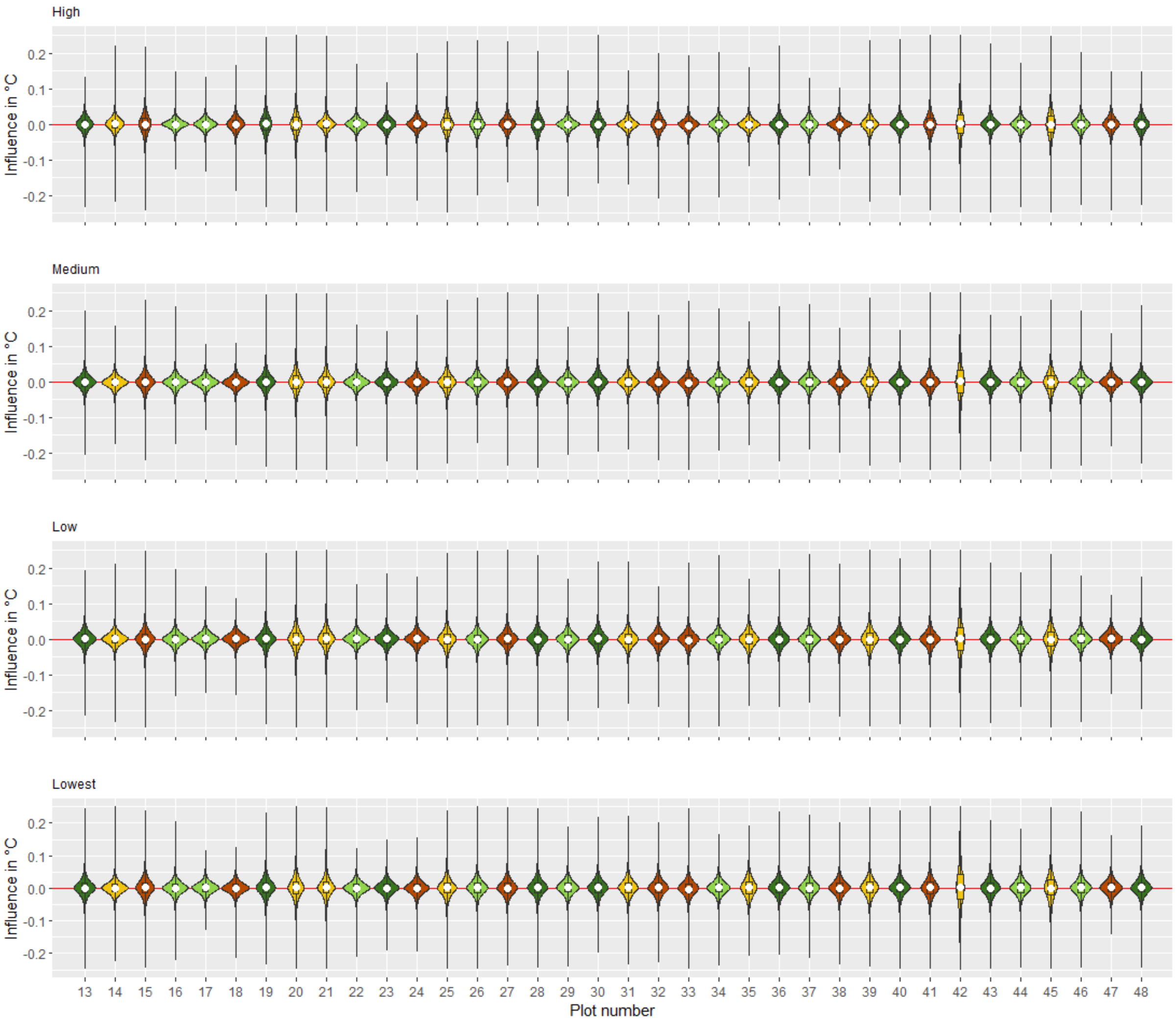

Figure 24 This graph shows the influence of the dense point cloud quality influence on orthomosaic temperatures with the average blending mode across all 36 grass plots. Each violin plot represents a single grass plot. Each graph with violin plots represents a different quality setting. The colours correspond to the respective grass species / mixture (see legend below).

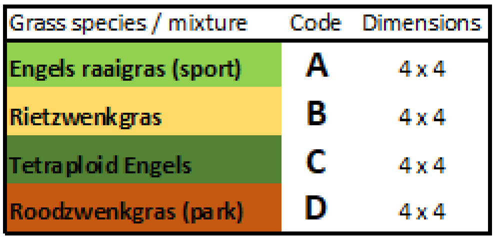

Grass species / mixture	Code	Dimensions
Engels raaigras (sport)	A	4 x 4
Rietzwenkgras	B	4 x 4
Tetraploid Engels	C	4 x 4
Roodzwenkgras (park)	D	4 x 4

Figure 25 Legend of what grass species match the colours in the violin plots.

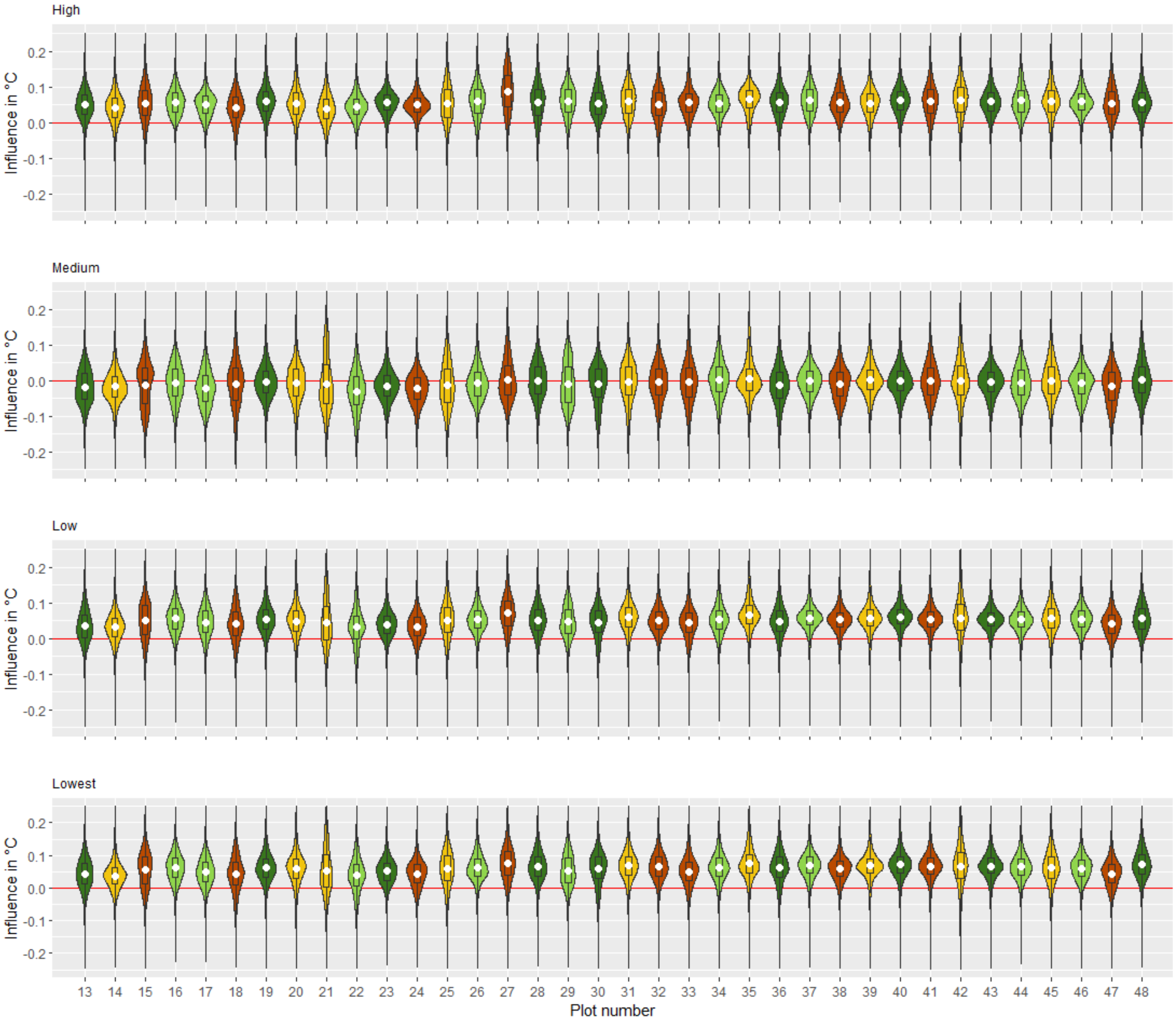

Figure 26 This graph shows the influence of the dense point cloud quality influence on orthomosaic temperatures with the mosaic blending mode across all 36 grass plots. Each violin plot represents a single grass plot. Each graph with violin plots represents a different quality setting. The colours correspond to the respective grass species / mixture (see legend below).

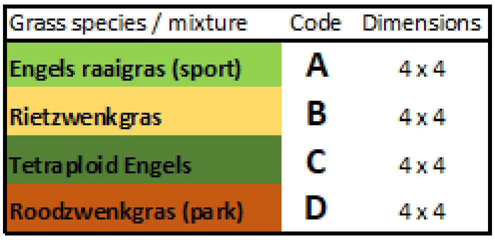

Grass species / mixture	Code	Dimensions
Engels raaigras (sport)	A	4 x 4
Rietzwenkgras	B	4 x 4
Tetraploid Engels	C	4 x 4
Roodzwenkgras (park)	D	4 x 4

Figure 27 Legend of what grass species match the colours in the violin plots.

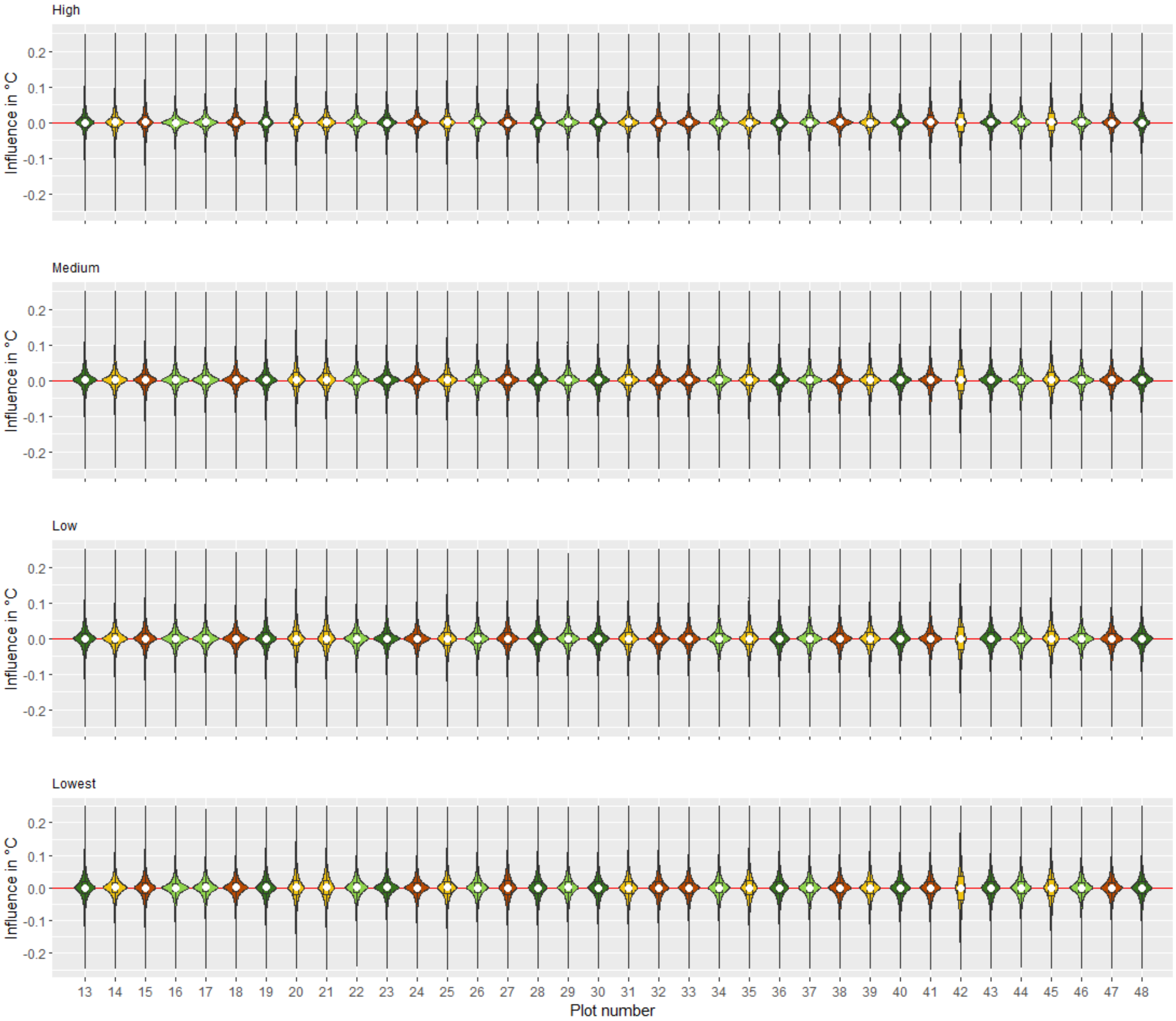

Figure 28 This graph shows the influence of the dense point cloud quality influence on orthomosaic temperatures with the disabled blending mode across all 36 grass plots. Each violin plot represents a single grass plot. Each graph with violin plots represents a different quality setting. The colours correspond to the respective grass species / mixture (see legend below).

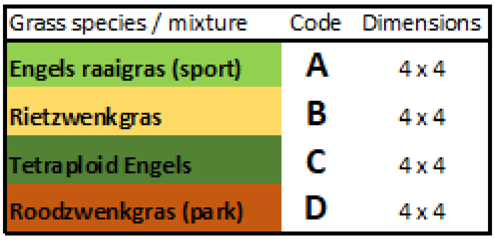

Grass species / mixture	Code	Dimensions
Engels raaigras (sport)	A	4 x 4
Rietzwenkgras	B	4 x 4
Tetraploid Engels	C	4 x 4
Roodzwenkgras (park)	D	4 x 4

Figure 29 Legend of what grass species match the colours in the violin plots.

K. DPC depth filtering influence per grass plot

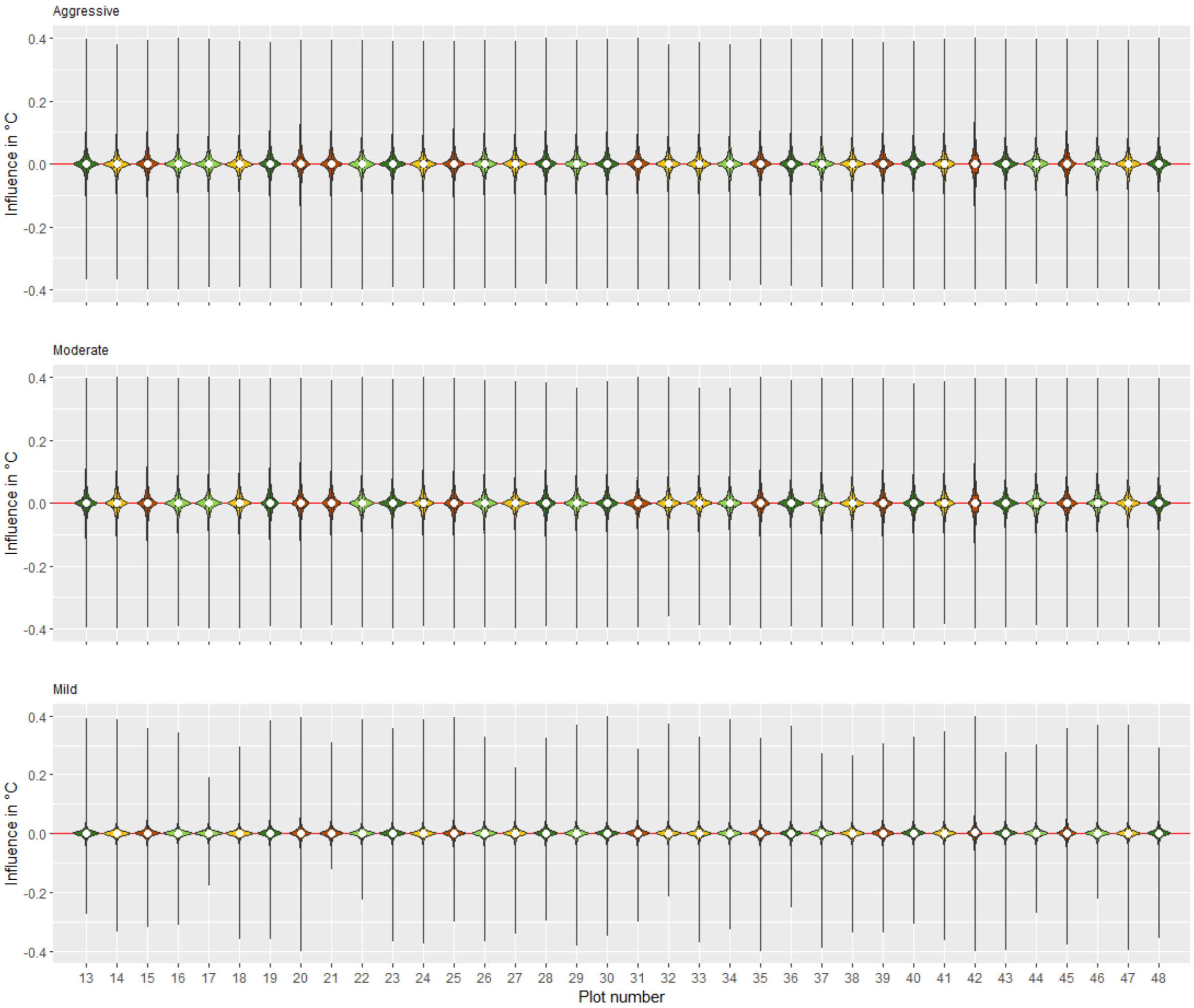

Figure 30 This graph shows the influence of the dense point cloud depth filtering settings on orthomosaic temperatures with the disabled blending mode across all 36 grass plots. Each violin plot represents a single grass plot. Each graph with violin plots represents a different depth filtering setting. The colours correspond to the respective grass species / mixture (see legend below).

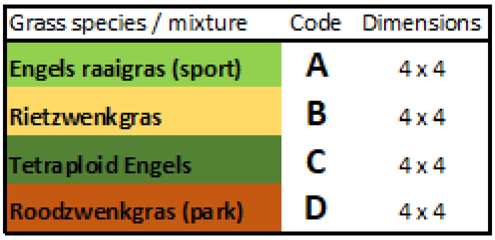

Grass species / mixture	Code	Dimensions
Engels raaigras (sport)	**A**	4 x 4
Rietzwenkgras	**B**	4 x 4
Tetraploid Engels	**C**	4 x 4
Roodzwenkgras (park)	**D**	4 x 4

Figure 31 Legend of what grass species match the colours in the violin plots.

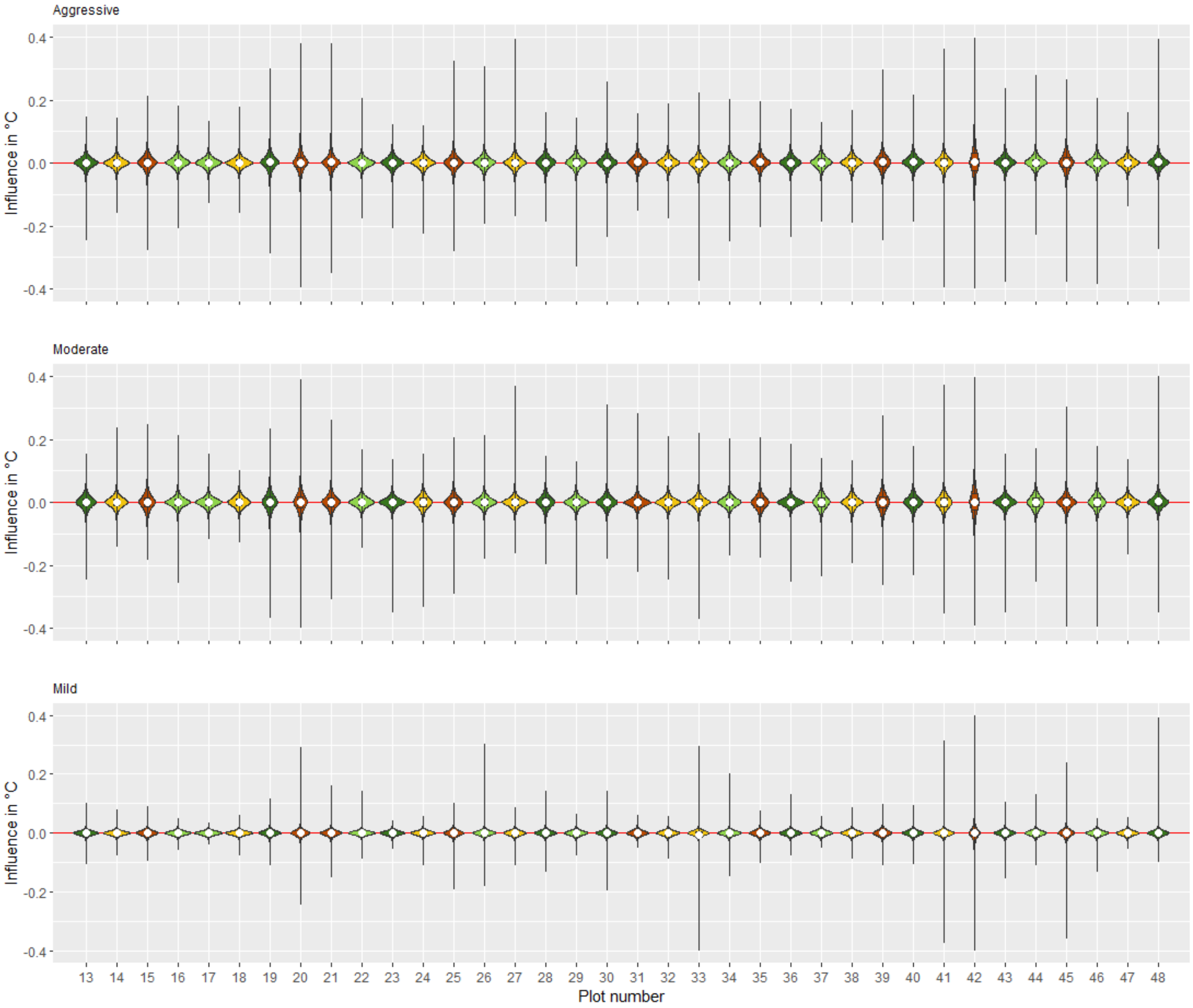

Figure 32 This graph shows the influence of the dense point cloud depth filtering settings on orthomosaic temperatures with the average blending mode across all 36 grass plots. Each violin plot represents a single grass plot. Each graph with violin plots represents a different depth filtering setting. The colours correspond to the respective grass species / mixture (see legend below).

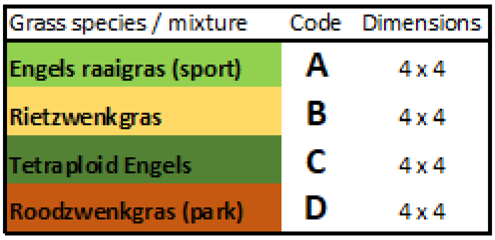

Grass species / mixture	Code	Dimensions
Engels raaigras (sport)	**A**	4 x 4
Rietzwenkgras	**B**	4 x 4
Tetraploid Engels	**C**	4 x 4
Roodzwenkgras (park)	**D**	4 x 4

Figure 33 Legend of what grass species match the colours in the violin plots.

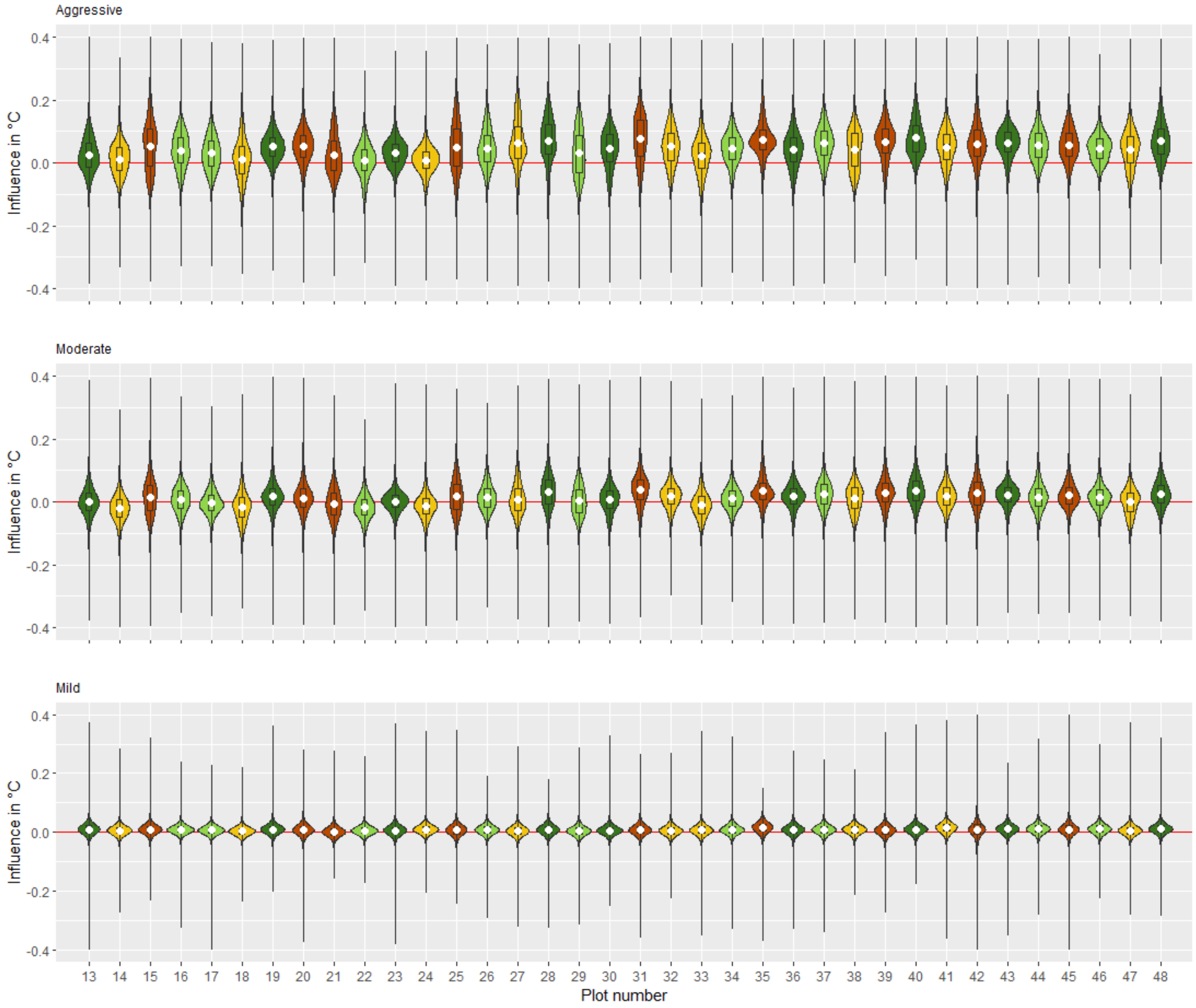

Figure 34 This graph shows the influence of the dense point cloud depth filtering settings on orthomosaic temperatures with the mosaic blending mode across all 36 grass plots. Each violin plot represents a single grass plot. Each graph with violin plots represents a different depth filtering setting. The colours correspond to the respective grass species / mixture (see legend below).

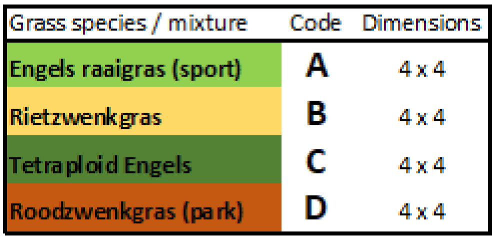

Grass species / mixture	Code	Dimensions
Engels raaigras (sport)	**A**	4 x 4
Rietzwenkgras	**B**	4 x 4
Tetraploid Engels	**C**	4 x 4
Roodzwenkgras (park)	**D**	4 x 4

Figure 35 Legend of what grass species match the colours in the violin plots.

L. Colour calibration influence per grass plot

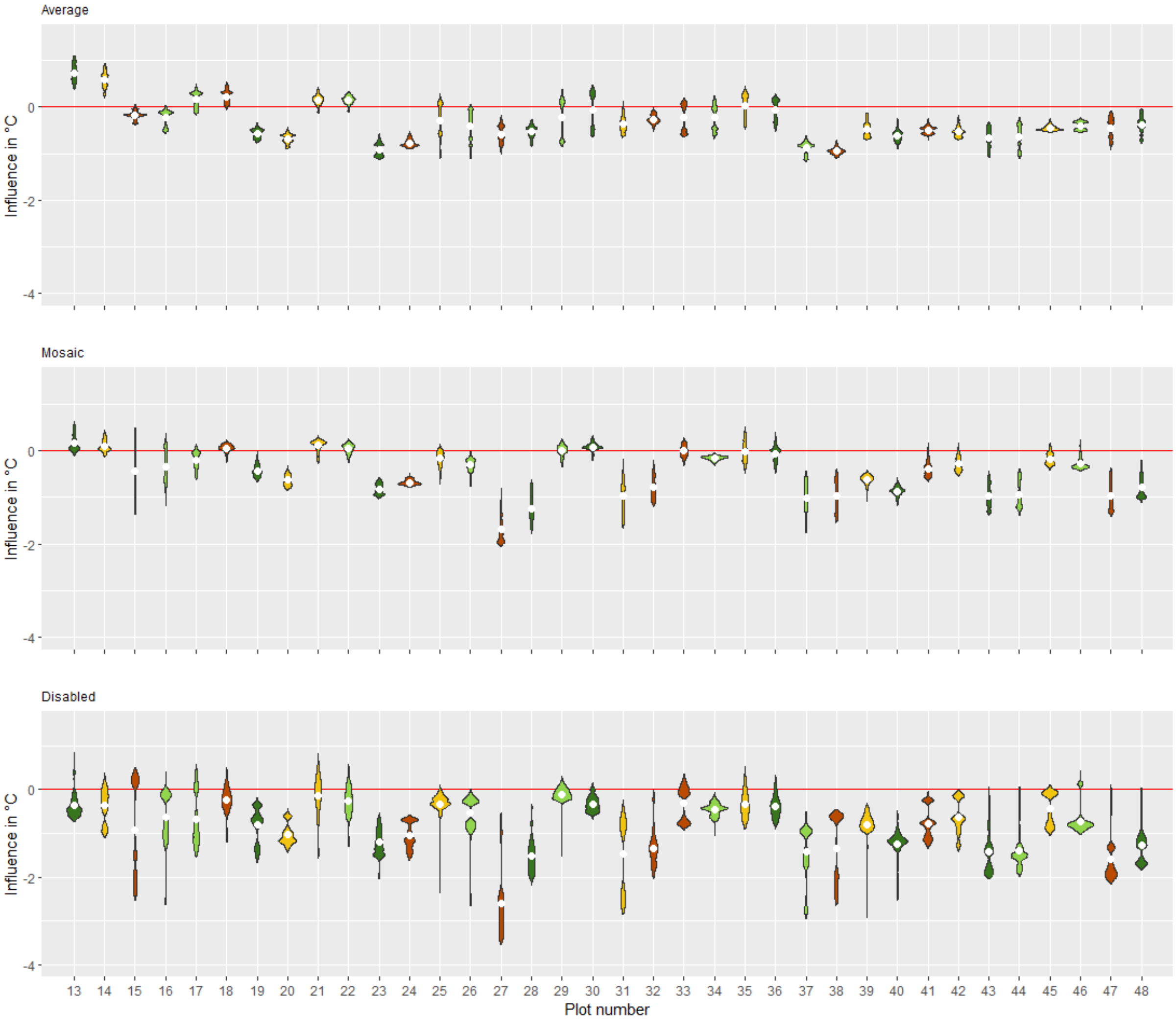

Figure 36 The influence of DEM based colour calibration on orthomosaic temperatures. Each violin plots represents one of the 36 grass plots. Each of the three graphs represents the influence of the DEM based colour calibration combined with one of the blending modes. The colours correspond to the respective grass species / mixture (see legend below).

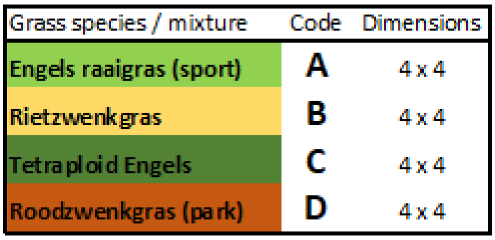

Grass species / mixture	Code	Dimensions
Engels raaigras (sport)	**A**	4 x 4
Rietzwenkgras	**B**	4 x 4
Tetraploid Engels	**C**	4 x 4
Roodzwenkgras (park)	**D**	4 x 4

Figure 37 Legend of what grass species match the colours in the violin plots.

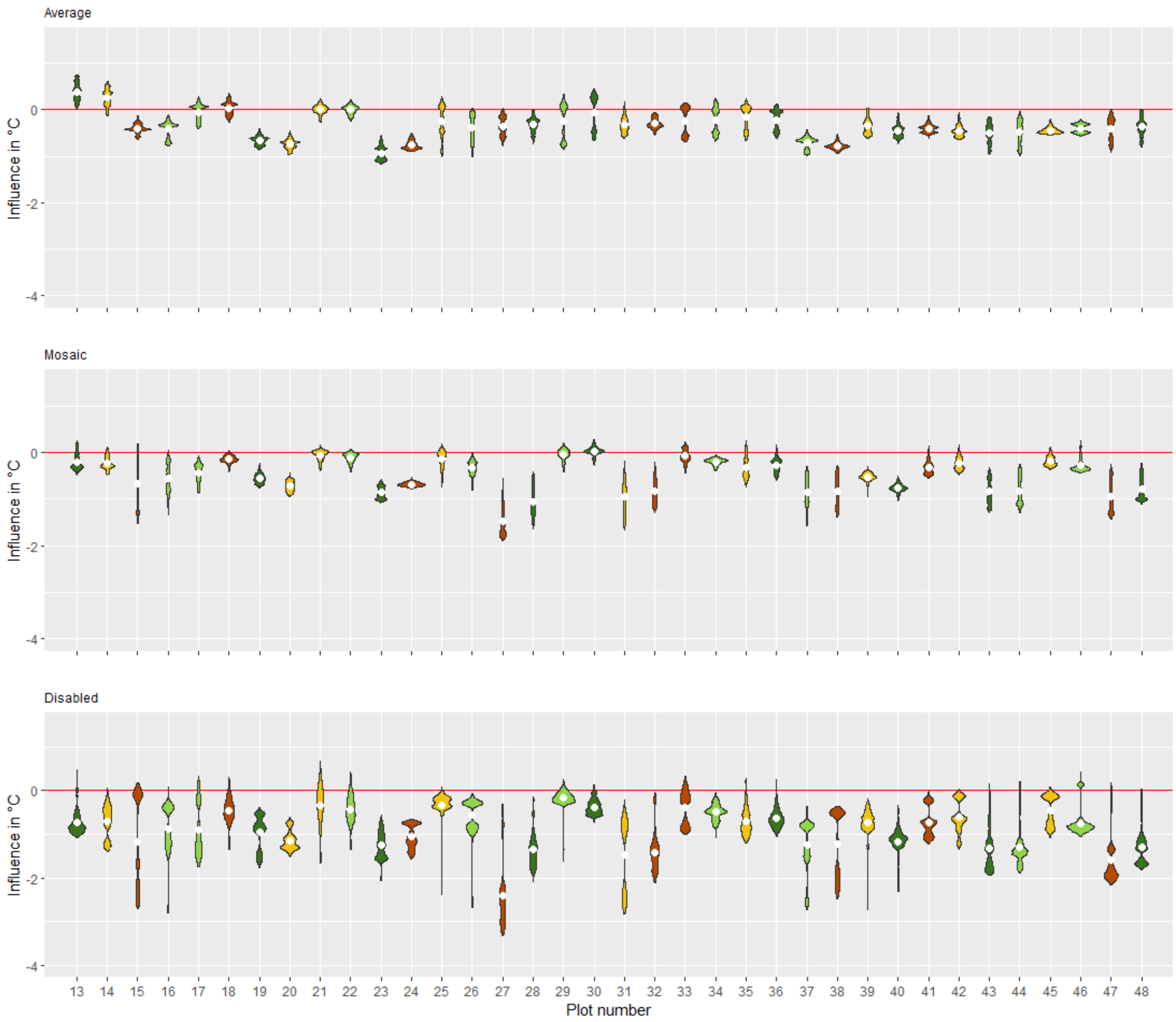

Figure 38 The influence of tie-point based colour calibration on orthomosaic temperatures. Each violin plots represents one of the 36 grass plots. Each of the three graphs represents the influence of the tie-point based colour calibration combined with one of the blending modes. The colours correspond to the respective grass species / mixture (see legend below).

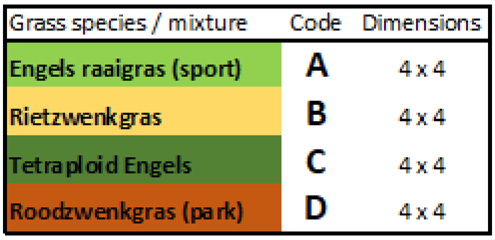

Grass species / mixture	Code	Dimensions
Engels raaigras (sport)	A	4 x 4
Rietzwenkgras	B	4 x 4
Tetraploid Engels	C	4 x 4
Roodzwenkgras (park)	D	4 x 4

Figure 39 Legend of what grass species match the colours in the violin plots.

M. DEMs generated at different quality settings

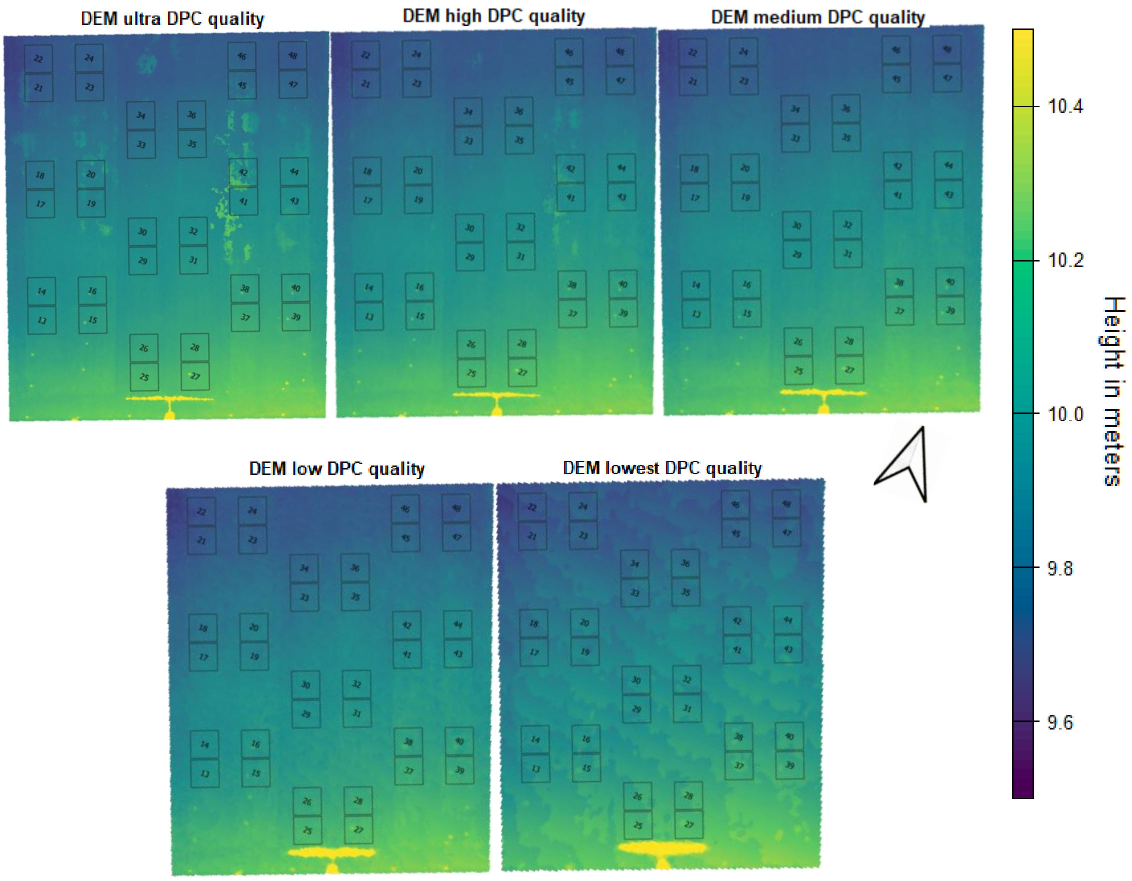

Figure 40 Height maps generated at all the DPC quality settings, combined with the disabled depth filtering setting. These DEMs were trimmed to fit the area the 36 grass plots reside in. Note how there are heights present around plots 41 and 42 at the ultra-high quality setting. These heights are still somewhat visible at the high quality setting, yet are not visible at the medium quality setting anymore. Excluding the thermal imagery removed these heights entirely (see figure below). Towards the low and lowest quality settings, a cloudy pattern becomes visible.

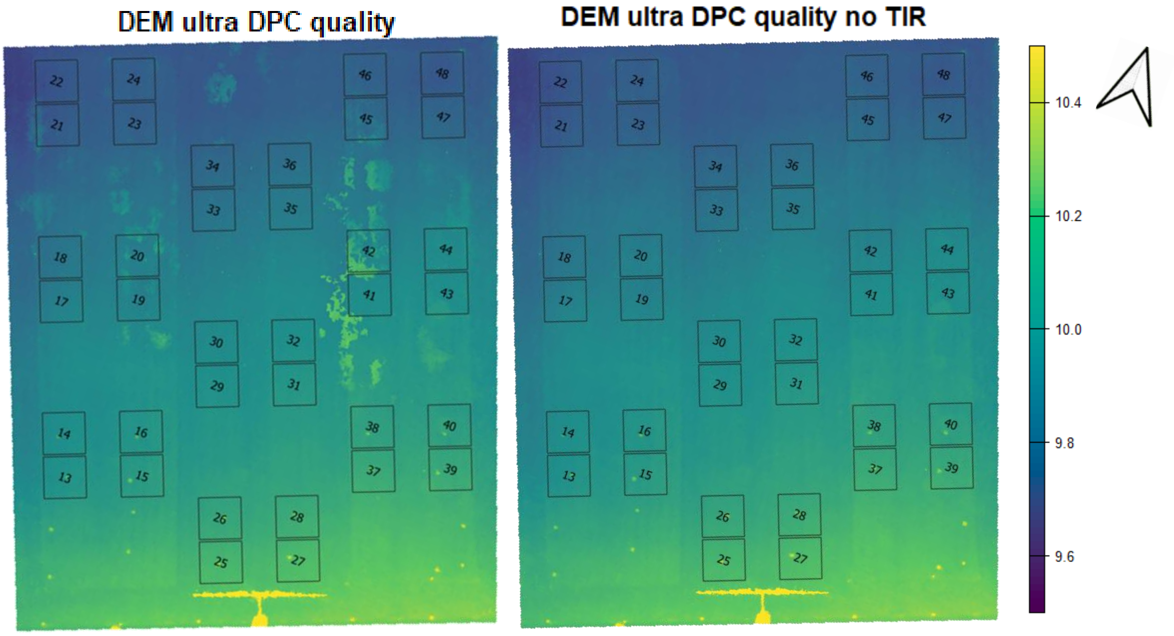

Figure 41 DEMs generated with the ultra-high DPC quality setting, combined with the disabled depth filtering setting. The DEM on the left was based on a DPC that was generated with thermal imagery included. The DEM on the right was generated based on multispectral

N. Combined influence of colour calibration with DPC quality settings

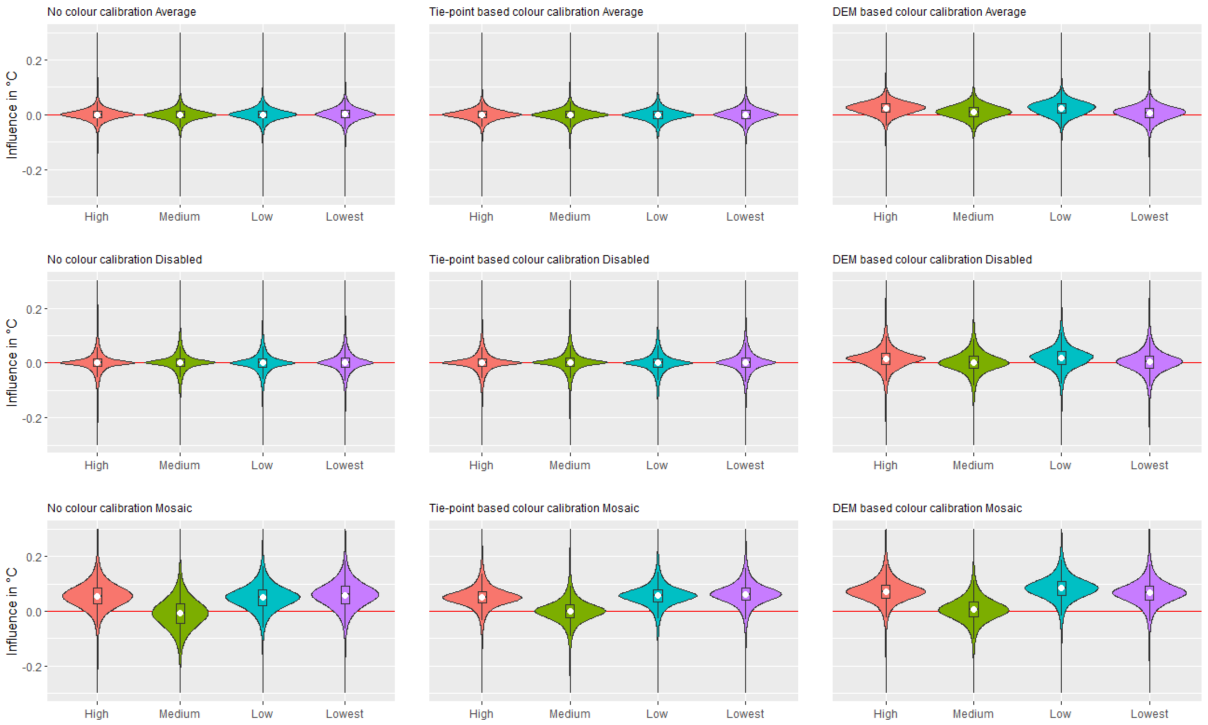

Figure 42 Combined temperature influence of the colour calibration settings and DPC quality settings on orthomosaic temperatures. The x-axis represents the quality settings. The influence of the quality settings without colour calibration is shown in the left column. The influence of quality settings combined with the tie-point based colour calibration is shown in the middle column. The influence of the quality settings combined with the DEM based colour calibration is shown in the column on the right. Each row represents the influence values at a different blending mode. Influence values in the top row were calculated with the average blending mode, in the middle row with the disabled blending mode, and the bottom row with the mosaic blending mode. Note how the influence of the tie-point based colour calibration is limited compared to the influence of the DEM based colour calibration.

O. Combined influence of colour calibration with DPC depth filtering settings

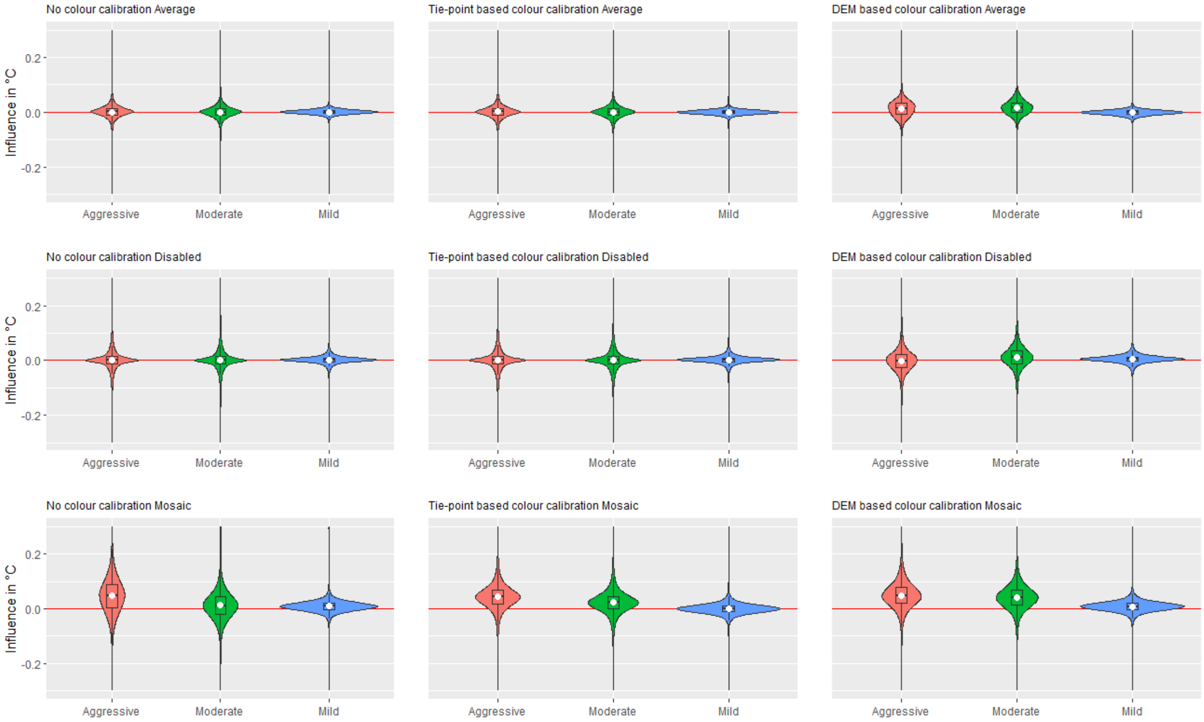

Figure 43 Combined temperature influence of the colour calibration settings and DPC depth filtering settings on orthomosaic temperatures. The depth filtering settings are shown on the x-axis. The influence of the depth filtering settings without colour calibration is shown in the left column. The influence of depth filtering settings combined with the tie-point based colour calibration is shown in the middle column. The influence of the depth filtering settings combined with the DEM based colour calibration is shown in the column on the right. Each row represents the influence values at a different blending mode. Influence values in the top row were calculated with the average blending mode, in the middle row with the disabled blending mode, and the bottom row with the mosaic blending mode. Note how the influence of the tie-point based colour calibration is limited compared to the influence of the DEM based colour calibration.